Volumetric Additive Manufacturing of Polymer Structures by Holographically Projected Light Fields

by

Maxim Shusteff

B.S.E. Princeton University (2001)
S.M. Massachusetts Institute of Technology (2003)

Submitted to the Department of Electrical Engineering and Computer Science
in Partial Fulfillment of the Requirements for the Degree of

Doctor of Philosophy in Electrical Engineering

at the

MASSACHUSETTS INSTITUTE OF TECHNOLOGY

September 2017

Author _____
Department of Electrical Engineering and Computer Science
August 31, 2017

Certified by _____
Nicholas Xuanlai Fang
d'Arbeloff Career Development Associate Professor of Mechanical Engineering
Thesis Supervisor

Accepted by _____
Leslie A. Kolodziejski
Professor of Electrical Engineering and Computer Science
Chair, Committee on Graduate Students

Volumetric Additive Manufacturing of Polymer Structures by Holographically Projected Light Fields

by

Maxim Shusteff

Submitted to the Department of Electrical Engineering and Computer Science
on August 31, 2017 in Partial Fulfillment of the Requirements for the Degree of
Doctor of Philosophy in Electrical Engineering

ABSTRACT

As additive manufacturing technologies proliferate and mature, overcoming some of their process limitations becomes increasingly important for the continued expansion of practical applications. Two such limitations that arise from layer-based fabrication are slow speed and geometric constraints (which include poor surface quality and challenges fabricating span, cantilever, and overhang elements). Moving beyond point-by-point and layer-by-layer approaches, the ability to generate a complex 3D volume as a unit operation has the potential to overcome these limitations.

Since holography has been extensively studied as a means for storage and retrieval of 3D geometrical information, this dissertation explores the use of holographically-shaped light fields for producing three-dimensional structures in a "volume at once" approach. Leveraging advances in spatial light modulator (SLM) technology, phase-controlled light fields are projected into photopolymer resin to cure a desired geometry. By overlapping multiple sub-regions of a single light field within the target volume, the successful fabrication of non-periodic complex 3D geometries is demonstrated by single exposures on timescales of seconds.

This dissertation presents a complete prototype platform that makes this approach possible, comprising a suitable hardware configuration along with the computational algorithms necessary to calculate and optimize the required optical fields. A study of the photopolymerization kinetics is also carried out, to determine the boundaries of usable process parameters such as resin absorbance and available light intensity. The results indicate that low-absorbing resins containing ~0.1% photoinitiator, illuminated at modest powers (~10-100 mW) may be used to produce full 3D structures from 1-10 second exposures, with volume build rates exceeding 100 cm^3/hr, without layering and with no need for a substrate or support material.

Thesis Supervisor: Nicholas Xuanlai Fang
Title: d'Arbeloff Career Development Associate Professor of Mechanical Engineering

Acknowledgments

The experience of completing this doctoral dissertation has been akin to the effort of climbing a tall mountain peak – reaching the top, you look around with satisfaction and a sense of accomplishment (and possibly also fatigue), and see all the others who made the climb with you. Just as the tallest peaks are virtually impossible to climb without a team, this PhD is not something that I did alone, and the accomplishment belongs as much to my family, friends, and colleagues as it does to me.

Most prominently, I owe an enormous debt of gratitude to my wife Tamar. Thank you for supporting and encouraging this slightly foolish endeavor of a PhD all the way through, in the myriad ways that you did (and the ways I didn't even notice), though I was already prone to bouts of working a little too hard even before I started. Мама и папа, вам я вечно благодарен за прочное основание знаний и любви к учёбе. Вы научили меня что такое старание до последних усилий, и зародили во мне безграничное любопытство, без которых никакой исследователь из меня не мог бы выйти - доктор или нет. И конечно за тот месяц, что вы провели у нас, позволив мне сделать последний рывок к финишу. To my brother Sasha, thank you for putting me up for every visit to Boston to meet with my committee, and for always keeping me humble. To my kids, thank you for being a constant reminder that life is more than work; I hope one day this thesis might serve as a measure of inspiration to climb your own mountain. Thank you to all the friends who cheered, needled, heckled, commiserated, and cheered again along the way, especially Jessica Blazer, and Dr. Dave Sopchak.

In the professional realm, thank you foremost to Chris Spadaccini, my friend and unfailingly supportive center lead, for the trust you place in those who work for you, and the example you set as a leader. To my thesis supervisor Prof. Nick Fang, our longtime collaborator, for being willing to take on a grad student with a very weird arrangement, and to my other committee members Profs. Karl Berggren and Jeff Lang for your guidance and mentorship throughout. To the staff of the MIT EECS Graduate Office, who enabled me to thread the administrative and bureaucratic needles needed to get to this point.

The reason I could carry out this research at all is because I'm highly fortunate to work with the additive manufacturing team at LLNL, a truly exceptional group of people. When talking about my job, I always tell people how lucky I am to be able to learn something literally every single day; my generous, creative, and knowledgeable colleagues are the reason why. Thanks especially to Allie Browar for the Kingdom of Cubes, and to James Oakdale and Todd Weisgraber for giving me a framework which allowed me to start filling in the yawning gaps in my understanding of photopolymerization. Thank you to my other colleagues, who are too many to name – your kindness and advice, technical and otherwise, and good humor most of all give me the real reasons that I like coming in to work every day. To those of my managers who supported and nurtured my slightly crazy idea to finish my doctorate, by smoothing my path through LLNL's often-turbulent and never-linear environment: Elizabeth, Diane, Rob and Anantha, thank you all.

The best part of this, as with any significant effort, is that it's not only the end of a major life chapter, but the beginning of another. I'm energized by the possibilities that the future holds in store in this technology space.

A portion of this dissertation was adapted from a conference paper: M. Shusteff *et al.* "Optimal Source Beam Shaping for Digital Holographic Lithography," in Proceedings of the 2016 Imaging and Applied Optics Congress: *Digital Holography and Three-Dimensional Imaging*, The Optical Society, Heidelberg, Germany, 2016: paper DW1D.2.

Funding from LLNL Laboratory-Directed Research & Development (LDRD) project numbers 14-SI-004 and 17-ERD-116, as well as from the LLNL Educational Assistance Program (EAP) is gratefully acknowledged.

This work was performed under the auspices of the U.S. Department of Energy by Lawrence Livermore National Laboratory under Contract DE-AC52-07NA27344. LLNL-TH-735018.

Table of Contents

Chapter 1
Introduction

1.1 Background and Motivation

The recent decade has seen a great intensification of interest in non-traditional manufacturing and "making" capabilities, a group of technologies collectively referred to as additive manufacturing (AM) [1]. This terminology refers to building three-dimensional (3D) structures "from the bottom up," by adding material, rather than "subtractive" by cutting, milling or machining parts down from a larger workpiece. Although the conceptual framework for AM was put into place decades ago [2,3], the materials [4], methods [5], and applications of AM have significantly expanded and matured in the recent few years, pushing into the nanometer scale [6], and the meter-scale [7], as well as reaching into the consumer market, where it has manifested itself as affordable desktop "3D printer" technology.

Research efforts into new AM processes and materials have accelerated, with a handful of major peer-reviewed journals on the topic launched just during the three-year period of research culminating in this dissertation, including Elsevier's *Additive Manufacturing* and Springer's *Progress in Additive Manufacturing*. A notable research area is the development of novel architected materials, with properties not found in nature, nor seen in bulk or monolithic materials, including mechanical [8,9], photonic [10,11], electromagnetic [12] and acoustic [13] properties. With few exceptions, producing these materials cannot be accomplished by conventional machining and manufacturing methods, nor standard planar silicon-based MEMS microfabrication.

A generalized AM process begins from a 3D CAD model of a part, typically sectioned into two-dimensional (2D) layers by closely-spaced parallel planes. Each layer is then built up or deposited at a specified thickness, with its computer-generated geometry defining the extent of

the deposition. The substrate on which the build is forming is repositioned, and the next layer is added in sequence, until the full set of slices comprising the part has been formed. Because digital CAD data drives the fabrication platform directly, without the need to develop tooling or fixturing, this paradigm is also called "direct digital manufacturing." Material deposition methods vary widely, giving rise to an alphabet soup of AM processes, ranging from material extrusion, to solidification of liquid resin, to binding/sintering of powder feedstock.

The point-by-point and layer-by-layer techniques that are characteristic of AM fabrication approaches are advantageous owing to their generality, which allows broad geometric versatility. But along with these advantages, the decomposition of 3D structures into low-dimensional subunits has also imposed their own new set of fabrication constraints. Two of the most significant are slow build rates, and layering artifacts. The slow build speeds derive from the serial deposition of the low-dimensional (point, line, plane) subunits in nearly every available AM technique, typically requiring hours to make a structure. Layer artifacts arise from the discretization of a digital CAD model into planes, which leaves stairstep features, degrading the surface characteristics of finished parts. In addition, some overhanging and spanning geometries are impossible to produce without support material.

To examine this more closely, AM processes can be grouped by the dimensionality of their unit operation. Point-based approaches that use a 0D voxel as their fundamental operation include methods such as laser-scanning stereolithography (SLA) and its derivatives [14], selective laser melting [15], and direct laser-writing (DLW) [16]. Extrusion-based filament methods such as direct-ink writing (DIW) [17], direct-metal writing [18], and fused-filament fabrication (more often known by the trademarked term fused deposition modeling FDM) [19] use a 1D fundamental unit. In a number of recent reports, including projection micro-stereolithography [20,21], continuous liquid interface printing (CLIP) [22], and diode additive manufacturing (DiAM) [23], complete 2D layers are formed in a single operation.

Advancing into the realm of forming complex 3D volumes as unit operations is one of the last remaining barriers to overcome for rapid 3D part fabrication spanning all three spatial

dimensions. This leap continues to present conceptual and technical barriers. To-date volumetric 3D structures patterned in a single operation have not been demonstrated outside the realm of interference lithography of polymers [24–27]. Here, a photoactive material is exposed to the intersection of multiple coherent beams, with the coherent interference of these beams forming the desired patterns, typically submicron lattices. The resulting geometries have useful properties such as electrode materials with controlled porosity [26], or photonic crystals [28], but one of the part dimensions must always be orders of magnitude smaller than the others. That is, only a relatively thin layer of material can be patterned, even when such lattices are modulated by larger-scale aperiodic features [25,29].

Some possibilities exist of overcoming the constraints of the layer-by-layer paradigm. Of course, DLW (0D voxel fundamental subunit) and DIW (1D filament fundamental subunit) allow some capability to build out-of-plane unsupported structures, writing unsupported "into space" or into the bulk of a photopolymer volume. However, there are still significant geometric limitations for both methods, and the discretization (stairstep/layers) and speed problems remain due to serial deposition of 0D or 1D elements.

A few investigators have reported more creative efforts to overcome typical layering constraints. A technique called stop-flow lithography developed in 2007 by Doyle and co-workers [30] generated micron-scale particles in a microfluidic channel, but these were constrained to prismatic geometries. Paulsen and Chung later extended this technique by using inertial fluid shaping to add complexity in the third dimension [31], but still with significant geometric limitations. Kim *et al*. used an approach they dubbed "low one-photon polymerization (LOPP)" [32] to polymerize simple structures in bulk resin. Gandhi and Bhole [33] modulated the depth of polymerization in a laser-scanned stereolithography process by adjusting the laser intensity and scan speed, resulting in non-planar structures. However, these remained discretized due to the laser's finite beam size, and feature sizes along the different directions were significantly different from one another. None of these approaches indicate a path toward geometric versatility/generality, nor overcoming the speed and surface finish limitations typical in AM.

Thus, one of the primary motivations for undertaking this research is developing an AM process that is capable of patterning 3D volumes with non-periodic (ideally arbitrary) geometries as its unit operation. The expectation is that such an approach will allow a significant increase in fabrication speed over existing AM approaches. Likewise, without needing to slice a part geometry into 2D planes, we hypothesize that the stair-step layering (or other discretization) artifacts can be significantly reduced or even eliminated.

1.2 Research Strategy

1.2.1 Technical Rationale

The conceptual underpinnings for the research paths of this dissertation emerge from several considerations. First, patterning by means of light energy. Because light is one of the major patterning approaches for AM (whether broadband, LEDs, or lasers) using light to drive a "volume-at-once" AM process provides a natural promising direction of inquiry. In fact, light-based patterning is currently the sole approach that allows entire 2D layers to be fabricated at once, so moving to volumetric unit operations would appear to also require light shaping. Especially notable here is the realm of holography, which has been developed over half a century as a means for light-based recording and re-creating of 3D geometric information [34].

A second conceptual element is closely related to the first: the use of diffractive optical elements (DOEs) for light shaping. Diffraction-based optical analysis and design dominates the field of holographic and interference-based light manipulation. Using DOEs allows capabilities in light manipulation that are not accessible with ordinary imaging approaches; specifically, direct phase-shaping of the optical field. In this domain, the use of spatial light modulators (SLMs) as dynamically-reconfigurable DOEs has become widespread as the performance of the underlying liquid crystal and micromirror-based technologies has improved.

The third major conceptual frame is the use of photopolymer resins. These photosensitive liquids that solidify upon exposure to light already provide the base material for a class of light-

driven processes, including stereolithography (SLA) [14,35] and its derivatives [20,36]. A 3D patterned light field intended to form an entire 3D structure in a material requires that material to be transparent to receive the required light energy throughout the target volume. Many pre-polymer resin formulations are transparent or translucent, and readily lend themselves to being incorporated here.

1.2.2 Key Research Goals and Questions

Drawing on these major intellectual building blocks, this thesis aims to address the following specific questions:

- Assess the essential feasibility of a fabrication system that can produce volume-at-once complex 3D structures, and ideally demonstrate a functional system.
- Does this approach deliver on its promise of speed and geometric versatility and can it overcome layer-by-layer fabrication limitations? What are its other benefits and shortcomings?
- What role can dynamic digital holography play in the realm of volume-at-once fabrication? Evaluate its utility, advantages and limitations.

1.3 Thesis Scope and Structure

Having set up the overall framing and thrust for this research effort in Chapter 1, Chapter 2 continues by reviewing holographic and diffractive light shaping, the characteristics of SLMs and their key operating parameters, phase-calculation algorithm, and practical considerations for producing high-quality holographically-generated intensity patterns.

With that building block in hand, Chapter 3 presents an overview of the entire fabrication platform from a system-level design perspective, how its different subsystems interact, and some key metrics to assess the performance of the optical subsystems in particular.

Chapter 4 closely examines the key chemical processes, kinetic parameters and optical characteristics of free-radical-initiated acrylate resin systems, keeping the viewpoint and analysis as general as possible.

Bringing the resin chemistry and the optical system together, Chapter 5 covers the fully-functional demonstration of the volumetric 3D fabrication system designed and built during the course of this research. Details of the methods required to fabricate 3D structures are presented, as are example structures, as well as the results of a suite of characterization experiments. Initial conclusions about the overall 3D volume-at-once approach are made.

Finally, Chapter 6 evaluates the results and performance of this fabrication platform in comparison to other polymer-based technologies, based on metrics like build speed and feature resolution. It continues to discuss the advantages and limitations of the overall approach, as well as the specific implementation using holographic beam shaping. Lastly, I identify future directions for further research.

Chapter 2
Digital Holographic Shaping of Optical Fields

This chapter examines the use of phase-only spatial light modulator (SLM) technology for controlling optical fields, and the potential uses of patterns generated in this way for 3D structure fabrication. We first review the fundamentals of holographic recording and reconstruction of 3D geometric information, and how these are brought into the realm of dynamic digital data by using SLMs as dynamic phase masks. We subsequently consider how an SLM should best be chosen for the purposes of 3D fabrication among the available types and how their operating parameters are expected affect system performance. With an SLM technology in mind, we examine the practical considerations required to project high quality images, and briefly consider where the current advancements in SLM technology may lead with respect to 3D fabrication capabilities.

2.1 Holography Fundamentals

Originally pioneered in the 1940s by Dennis Gabor [37], for which he received the 1971 Nobel Prize in Physics, holographic recording, is in essence, an interferometric means of capturing the phase of an electromagnetic field, in addition to its amplitude. The phase of a light wave contains information about its distance travelled, therefore allowing precise recording of the 3D geometry that generated that wave. Traditional recording media for optical holograms, such as photochemical emulsions, capture the interference fringes produced from the interaction of an optical field of interest and a "reference beam." These fringes, as recorded, form a diffraction grating containing the phase information of the original light field, which can then be illuminated by a different light field (a "reconstruction beam") onto which this phase information is "imprinted" to recover and display the original 3D geometry.

The advent of digital technology and high-performance liquid-crystal displays has enabled the emergence of a new way to phase information to an illuminating light field. This is the use of SLMs, which perform the function that their name implies – they modulate incoming light fields in a spatially-varying manner. SLMs generally take the form of pixelated display panels, and can be designed to modulate either the amplitude or phase of the light field (or both, but in such cases, the phase and amplitude usually are not independent). Thus, a phase-only SLM is a computer-controlled addressable array of custom phase retarder elements. With this powerful capability, phase maps may be synthesized from digital data on a computer, and displaying these on the SLM allows the shaping of the light field impinging upon it. A correctly-designed phase map may be used to "reconstruct" 3D data that was never physically recorded, only synthetically generated from bits and bytes [38].

Thus, digital holography bypasses the static recording of optical phase-fields in physical-chemical media in favor of reconfigurable, dynamic control of these fields. The main drawback of digital holography is the much lower resolution of pixelated SLMs (~1-10 μm) compared with photochemical emulsions (whose grain size is ~10-100 nm) [39,40]. This has important consequences for the maximum diffraction angle available from digital SLM-based holograms, discussed in Section 2.3.2 below, which drives the design constraints of practical systems that use these SLMs for light shaping, as we shall see below.

Nevertheless, here we find a direct link to the additive manufacturing (AM) paradigm, in which 3D geometric information from CAD-CAM software can be directly used to control a fabrication system to produce the physical embodiment of the 3D geometry ("direct digital manufacturing"). The appeal of digital holography as a means for dynamically reconstructing 3D geometric information for AM is evident.

2.2 Image Projection by a Phase-only SLM

Prior to considering how an SLM should be chosen for applications in 3D fabrication, we require an understanding of how a phase-only SLM produces a specified intensity distribution. Since all

optical detectors, be they a CCD camera, the human eye, or a photosensitive resin to be polymerized, respond to the light intensity or amplitude, phase shaping is used here in the service of amplitude-shaping.

2.2.1 Fourier Optics and Calculation of Phase Holograms

Following the treatments of Kim [41], and Goodman [42], we can consider a generic optical beam, given by

$$E(x,y) = a(x,y) \cdot e^{-i\phi(x,y)}, \tag{2.1}$$

which is a complex-valued electric field E, with amplitude a and phase ϕ, which are both real-valued scalar quantities. Each of these varies spatially in a transverse *x*-*y* plane (the beam propagation direction is conventionally z). The intensity "seen" by a detector or a photopolymer is $I(x,y) = |a(x,y)|^2$. A full treatment of scalar diffraction theory is not required here; it is sufficient to highlight one of the main results critical for understanding projection by a phase-only SLM: the optical fields at the two focal planes on either side of a lens are Fourier transforms of each other. Thus, if we consider a generic SLM placed at the focal plane of a lens, where the field is denoted $E_{SLM}(x,y)$, with the focal plane at the other side of the lens denoted as $E_{HP}(k_x, k_y)$ (HP is the "hologram plane"), we can write

$$E_{HP}(k_x, k_y) = \mathcal{F}\{E_{SLM}(x,y)\} = \iint E_{SLM}(x,y) \cdot e^{-2\pi i(xk_x + yk_y)} dxdy \tag{2.2}$$

and

$$E_{SLM}(x,y) = \mathcal{F}^{-1}\{E_{HP}(k_x,k_y)\} = \iint E_{RP}(k_x,k_y) \cdot e^{2\pi i(k_x x + k_y y)} dk_x dk_y \tag{2.3}$$

Here $\mathcal{F}\{\}$ is the Fourier transform operator, and k_x and k_y are spatial frequencies, that map to physical coordinates (x', y') in the HP as $k_x = x'/\lambda f$ and $k_y = y'/\lambda f$, where λ is the illuminating wavelength and f is the focal length of the Fourier-transforming lens (FTL). This is

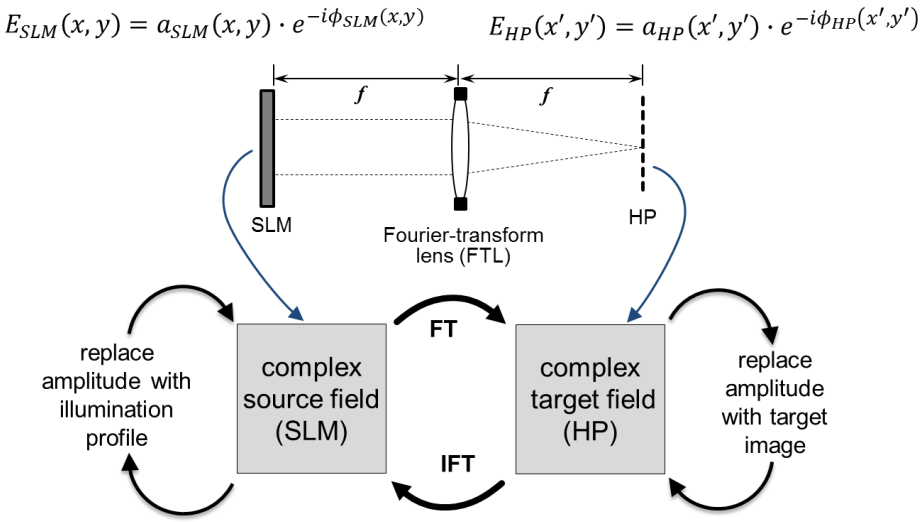

Figure 2.1. Fourier-transform pair relationship between optical fields at the focal planes on two sides of a lens. The complex fields are written out explicitly with amplitude and phase components at the top, and the iterative Gerchberg-Saxton algorithm is summarized at the bottom. FT and IFT represent forward and inverse Fourier transform operations, respectively. The iterative loop is typically initialized with either a uniform or a random phase distribution.

illustrated graphically in Figure 2.1, and the transform pair reflects the reciprocal relationship between spatial coordinates on either side of the lens.

Therefore, in order to use a phase-only SLM to generate a particular intensity distribution at the HP, a phase distribution must be computed for the SLM whose Fourier transform will yield the required intensity pattern. This phase distribution is referred to as a computer-generated hologram (CGH). Fortunately, this task has been studied extensively, and is generically known as phase retrieval. There are a variety of approaches to successful phase retrieval [43–47], of which the most widely implemented by far is the Gerchberg-Saxton algorithm (G-S) [48], originally described in 1972. This iterative method retrieves the phase distribution at an optical plane, constrained by amplitude distributions specified at that plane and a second plane, when the two planes are related by a Fourier transform. By performing successive forward and inverse Fourier transforms, graphically summarized at the bottom of Figure 2.1, the algorithm generates successive approximations until a certain error criterion is met.

Though some of the other methods for calculating phase holograms result in substantially higher-quality images, these often impose much greater computational costs, or some may only be used with limited geometries. The simplicity and speed of the G-S approach, and in particular its generality when producing unconstrained arbitrary image patterns, make it the most appropriate choice in this situation.

For all of the CGHs calculated during this work, unless otherwise specified, a starting image of 1920×1920 pixels was input into a G-S algorithm implemented in MATLAB (The Mathworks, Natick, MA, USA). For CGH computation using discrete Fourier transforms (DFT), and representing diffraction based on square liquid crystal pixels, the starting image must always be square. The resulting phase distribution was cropped to be 1080 pixels high, to fit within the SLM active area. The G-S algorithm typically ran for 15-20 iterations, which was empirically found to be a suitable balance between acceptable image quality and computation speed. Each CGH required approximately 4.7 s to calculate on an Intel 3.0 GHz Xeon based desktop PC with 32 GB of RAM.

2.2.2 Projection of 3D Optical Fields

Up to now, we have considered only the projection of 2D planar intensity distributions, and algorithms designed for 2D patterns. Being concerned with fabrication of 3D structures, however, it's imperative to consider whether and how an SLM (or, more generally, a holographic phase-modulated optical field) can be used to produce 3D patterns. A highly illuminating study of this topic comes from Whyte and Courtial, who implemented and demonstrated the 3D analog of the G-S algorithm [49]. In essence, they extended the iterative error-reduction algorithm for calculating the phase at one of two *planes* having a Fourier transform relationship with each other, to calculating the phase distribution of one of two *volumes* with a Fourier transform relationship.

The key result of this work shows that the success of reconstructing 3D geometries depends critically on having a large numerical aperture NA. This is a fundamental concept in single-

beam optical field imaging that will be examined in more detail at the beginning of Chapter 3. For the present discussion, it is sufficient to note that the solid angle accessible by an SLM (expressed as NA) is one of the critical parameters that must be evaluated when selecting an SLM for 3D fabrication.

Moving forward in this chapter, we'll continue referring to 2D optical pattern calculations using the G-S algorithm, but the preceding arguments regarding the relationship of solid angle and 3D light shaping always remains present in the background.

2.3 SLM Selection for Holographic 3D Fabrication

The key properties that would make an SLM perform well in 3D fabrication applications include high resolution, large panel size, high modulation depth, and fast response time (equivalently, high frame rate). Below we review how these metrics impact 3D fabrication performance.

2.3.1 SLM Types

The most well-known SLM is the digital micromirror device (DMD), found in millions of digital projectors, but this technology is based on an array of mechanical micromirrors which deflect light on a pixel-by-pixel basis to turn them on or off. The DMD therefore only modulates amplitude, not phase. Liquid-crystal (LC) SLM technology is required for phase-only modulation, taking advantage of the intrinsic birefringence of LC molecules to accomplish phase modulation. These SLMs are built as LC layers on a pixelated backplane of CMOS silicon circuitry, termed liquid crystal on silicon (LCoS). These types of devices have been extensively reviewed by many authors [50–52].

Briefly, the two main classes of material around which LCoS displays are built, are ferroelectric (smectic phase) and nematic LC layers. Ferroelectric type displays have only two available polarization states (thus only two phase-delay values can be imposed), resulting in binary phase gratings. The advantage of these devices is fast response time on the order of 0.1 ms, yielding very high refresh rates, up to 1-10 kHz. The alternative approach using nematic LC allows

continuous modulation of the phase delay through a range of typically at least a full wavelength (2π phase), but at the expense of much slower response time in the 1-10 ms range, and refresh rates of ~10-100 Hz. The use of multiple phase levels allows for higher diffraction efficiency and higher signal-to-noise ratio in phase-only image projection, so a nematic LCoS SLM device was chosen for the current 3D fabrication application, prioritizing contrast ratio over refresh rate.

2.3.2 SLM Resolution and Space-Bandwidth Product

Two other key parameters of SLM design relevant for 3D fabrication considerations are pixel size (pitch) and pixel count. Since the SLM behaves as a diffraction grating, the pixel pitch, δ_p, determines the maximum possible diffraction angle for redirecting light power reflected from the LCoS panel. Equivalently, this diffraction angle also represents the angular spacing between diffractive modes as they propagate from the SLM, each of which contains a copy of the target amplitude distribution. From both perspectives, it is clear that a smaller pixel size allows for a larger addressable image area within the holographic reconstruction.

Conversely, the outer dimensions of the SLM display (the overall panel size $L_x \times L_y$) determine the minimal resolvable feature in an SLM-projected image. Since the SLM represents the frequency space of the image in the HP (due to the mutual Fourier transform relationship of the two planes), then the pixels at the outermost edges of the SLM control the highest-spatial frequency image components present at the HP. In general, the closest spacing between two points in the reconstruction plane that can be controlled by a phase-only hologram is given for a single dimension

$$\Delta x = \frac{\lambda f}{L_x}, \qquad \Delta y = \frac{\lambda f}{L_y} \tag{2.4}$$

where f is the focal length of the FTL. These are the locations of the first zeros of the sinc( ) function due to convolution with the Fourier transform of the SLM's aperture in each direction, and are approximately 8.7 μm and 15.4 μm for the SLM and FTL used in our configuration.

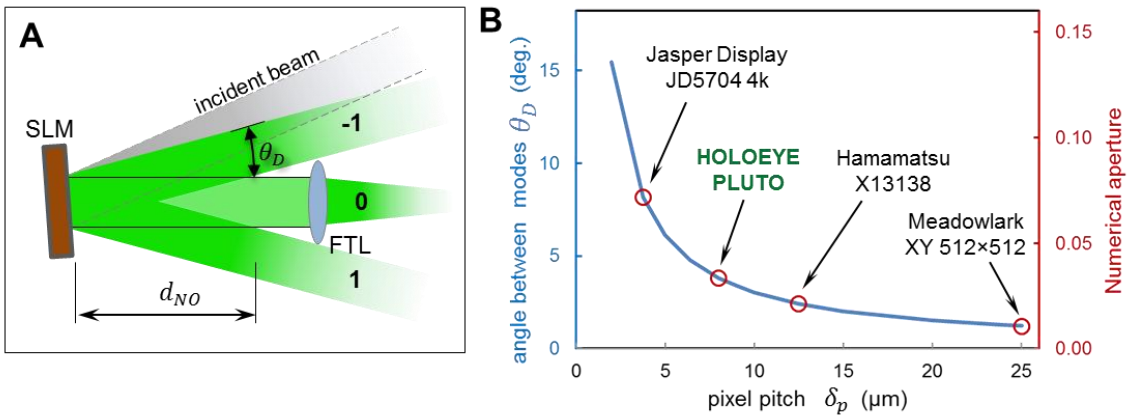

Figure 2.2: SLM diffraction angle and numerical aperture. (A) shows a near-normal incidence illuminating beam diffracting into -1st, 0th, and 1st order modes (higher orders are omitted for clarity). The minimal distance before there is no spatial overlap between diffractive modes is d_{NO}, which along with the panel size defines the SLM's NA. (B) The diffraction angle θ_D (left axis), and the corresponding NA value (right axis) is plotted as a function of the pixel pitch, indicated by the blue curve. Red circles show several currently-available commercial LCoS SLM devices. The Jasper Display device has the smallest available pixel pitch as of this writing, 3.7 μm.

The ratio of the maximum lateral displacement due to SLM diffraction to the panel size of the SLM directly corresponds to the NA of the SLM, since NA for an optical element can be defined as the ratio of its half-aperture to its focal length. Figure 2.2(A) shows the configuration of the first several diffractive modes coming off an SLM, and the geometry they define. The angular spacing of the diffractive modes is determined based on the grating equation

$$n \sin \theta_{d,m} - n \sin \theta_i = \frac{\lambda m}{\delta_p} \tag{2.5}$$

in which θ_i and $\theta_{d,m}$ are the angles of the incident and *m*th-order diffracted beams, respectively, and *n* is the refractive index of the medium. For near-normal incidence beams in air, the angle of the first mode is approximately $\theta_{d,1} = \sin^{-1} \frac{\lambda}{\delta_p}$, which is plotted in Figure 2.2(B), as is the corresponding value of the NA. A number of commercially-available phase-only SLM products are indicated in the plot, including the PLUTO SLM used in our system. The SLM's NA value is often the smallest among the critical optical elements in the whole system, and ends up defining the overall resolution performance.

In all of the work described here, we use the 0^{th} diffractive order of the SLM (shown directed through the FTL in Figure 2.2(A)). This beam contains the greatest fraction of the reflected light power, and has the most symmetric and uniform intensity distribution over the holographically-shaped image. Its central undiffracted light spot is also the strongest among the diffractive beams, and the strategy for handling this is described below, in Section 2.4.1.

The total number of SLM pixels is then a measure of the total information content within the hologram – the minimally resolvable spatial features that can be projected over the total extent of the projection area. This value is also referred to as the space-bandwidth product (SBWP) because it represents the product of the addressable space and the spatial frequency bandwidth. Thus, the best-performing SLM would have the smallest possible pixel size/pitch, and the largest possible pixel count for maximizing SBWP.

2.4 Practical Considerations for High-Quality Holographic Projection

A large number of studies have dealt with the non-idealities inherent in image projection by pixelated SLMs [53–55], and thus many techniques are available to measure and compensate them. Our aim here is to leverage these previous efforts to implement those that are most useful in the context of our system for eliminating practical barriers to

2.4.1 Eliminating Undiffracted Light

One of the most significant obstacles to the flexible and robust control of the light field in diffraction-based systems is eliminating interference from undiffracted light. Some fraction of the incident laser power reflects from the SLM without being modulated by the LC layer, generating an unwanted bright spot at the center of the build volume (with the intensity pattern that's the Fourier transform of the SLM rectangular aperture). Of the many approaches to mitigating and eliminating interference from this uncontrolled light [56–59], incorporating a high-pass beam block at the Fourier plane of the hologram projection lens (BB in Figure 3.1(B)) is the most robust implementation in this context. This approach is not pattern-dependent, nor

does it require exhaustive SLM calibration and aberration compensation; once the beam block is aligned, and the phase curvature calculated, no additional adjustments are necessary.

The shape of the beam block is designed to maximize its efficiency in rejecting un-diffracted light, while allowing maximum transmission of the holographically-controlled light field. Some approaches block half or one quarter of the lens focal plane, but this also blocks much of the designed phase-shaped light. We fabricated custom glass flats with a gold metal film to block the spot, patterned in a "star" shape, matching the dimensions of the Fourier transform of the SLM's rectangular aperture function.

The desired intensity pattern is displaced some further distance downstream by the addition of spherical phase curvature ("lens phase") to the calculated CGH. This permits the use of the full hologram space, with virtually no interference from undiffracted light.

2.4.2 Speckle Reduction

An ever-present consequence of using highly coherent illumination is speckle, arising from self-interference of the beam as it propagates through the optical system. While some have harnessed this effect for beneficial results [60,61], it is more often undesirable and needs to be reduced or suppressed [62,63]. This random intensity variation is particularly problematic for lithography, since it creates spatial noise in the reconstructed intensity pattern. In SLM-based holography, speckle noise is exacerbated by the digital noise arising from CGH calculation, as well as the discrete phase steps of the SLM pixels.

Previous reports of "speckle-free" reconstruction manage this by confining the digital reconstruction to discrete points [64,65], which is unsatisfactory here. However, it is straightforward to calculate multiple versions of a CGH that produce the same intensity pattern, by initializing the G-S algorithm with different random phases. Each of the resulting CGHs will then have different uncorrelated noise (and thus, speckle), and exposing them in rapid succession allows for an averaging effect that significantly improves the noise performance (estimated from statistical considerations to be a factor $\sqrt{N}$ for N CGHs), with an example shown in Figure 2.3.

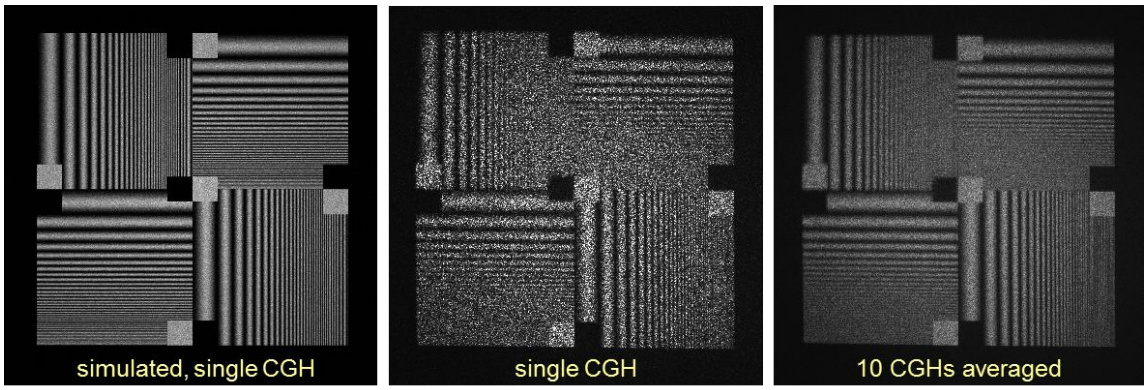

Figure 2.3: Holographic projection of the contrast/MTF test pattern, demonstrating the improved noise performance from averaging multiple CGHs generated to produce the same intensity pattern, initialized with a different random phase for each CGH. The simulated projection at left shows a Fourier transform of a single CGH in MATLAB, and the middle panel is the same CGH projected through our optical system and recorded with a CCD camera. The panel at right averages 10 separately recorded CGHs.

2.4.3 Vignetting Compensation

A third practicality of diffractive holographic image projection is an overall vignetting (image darkening near the edges and corners) imposed upon the reconstruction plane, due to the finite size of the SLM pixel as a diffraction-grating point-source. The reconstructed image is convolved with the PSF of the pixel aperture, which is a 2D sinc function that causes a drop-off in intensity toward the edges of the reconstruction plane [66,67]. For our system, we measure this illumination nonuniformity due to vignetting is measured by projecting a uniform gray optical field with the SLM, recording the nonuniform intensity distribution that results, and using the inverse of that distribution to generate a compensating intensity function that's edge-weighted. This function is then applied to modify all target intensity distributions prior to CGH computation for that optical configuration.

2.4.4 SLM Flatness

The thin layer of liquid crystal in an LCoS device must be highly flat and of uniform thickness to provide well-controlled phase modulation. Both nonuniform LC layer thickness (or nonuniform electrical birefringence), as well as curvature of the LCoS panel backplane itself impose

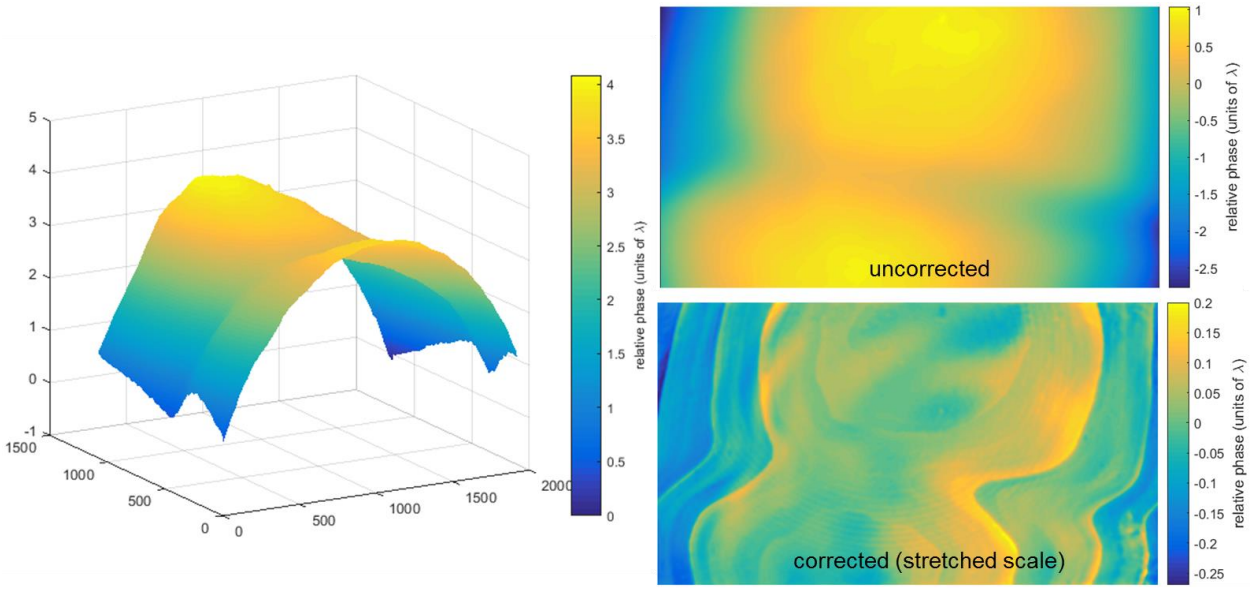

Figure 2.4. SLM Curvature Measurement and Compensation. Interferometric measurements of the SLM flatness reveal approximately 3.5λ of distortion. This can be reduced at least 10-fold (bottom right) by imposing a compensating phase function on the SLM. The main source of post-compensation distortions comes from the need for phase wrapping (discontinuities in the bottom image at right), since the SLM has a maximum modulation of approximately 1λ.

aberrations that affect image projection quality. Based on previous reports [68] and our own measurements (data not shown), it was determined that nonuniformity of LC thickness or response would not contribute sufficient aberrations to require compensation.

Additionally, direct measurements of the global SLM backplane curvature were made by using phase-shifting interferometry in a Michelson interferometer setup [69,70], shown in Figure 2.4. Although the SLM curvature is equivalent to several wavelengths, this represents a radius of curvature of approximately 30 m, therefore imposing negligible distortion. Because the full range of SLM modulation needs to be used for a compensating function, and no significant improvement in image quality was measured using the contrast/MTF test-pattern described in Section 3.2.1, the decision was taken not to include curvature compensation in routine CGH calculation algorithms.

2.5 Chapter Summary

In this chapter, exploring main performance specifications of pixelated phase-only SLM for 3D structure fabrication, the SLM's effective numerical aperture (NA) emerges as a parameter of primary importance. The numerical aperture, determined by the SLM's pixel pitch and total pixel count (SBWP), defines the maximum diffraction angle, the maximum image area that can be projected by the SLM, as well as the optical resolution limit. We find that even the highest-resolution SLMs among those available today (3.74 µm pixel pitch, approx. 8 Mpx) have relatively low NA values of 0.1 or lower, which end up being the limiting factor in defining 3D image-forming performance. Additional advances in LCoS SLM technology may be expected to improve pixel pitch by an additional factor of 2-4x, but pixel sizes below 1 µm appear unlikely without substantial demand from some other sector of the consumer market (e.g. in holographic displays). Similarly, an increase in total pixel count beyond a factor of 2-4x seems a similarly significant technological challenge. Thus, NA constraints will be the dominant limitation for using phase-shaped light to define 3D geometries for photopolymer fabrication for the foreseeable future. Most other parameters of currently-available SLMs, such as modulation depth, number of available phase levels, and speed are sufficient for 3D fabrication applications.

The other major challenge to overcome for robust 3D structure fabrication is mitigating speckle-induced spatial noise. The fundamental physics of diffractive imaging impose this obstacle: high source coherence is required to achieve high contrast in an interference-based image, but high coherence implies increased speckle. Where the optimal balance between these constrains lies will remain an area for further investigation. The current approach of "averaging" multiple rapidly-scanned CGHs to reduce spatial noise is a reasonable practical workaround, but greatly increases the computational cost of retrieving the necessary phase distributions to multiple CGHs, with only mediocre results (see Chapter 5). The possibility of using incoherent sources with amplitude-controlled (rather than phase-controlled) image projection must therefore be considered in future implementations of the volumetric 3D fabrication paradigm.

Chapter 3

Three-Dimensional Volumetric Fabrication System Design

This chapter discusses the subsystems required to implement a holographic volumetric fabrication system, in addition to the spatial light modulator. We discuss the configuration of components, and the consequences of various specific design choices, parameters, and trade-offs for system performance. Before detailing the full design, however, it is important to understand the underlying principles that necessitate the multibeam superposition approach.

3.1 Rationale for Multibeam Superposition

Polymerizing complex 3D structures in photopolymer requires equally high spatial resolution in all three basis directions. The fundamental constraint on shaping 3D optical fields for this purpose arises from the limitations of physical optics. Scalar diffraction theory, after Abbe and Rayleigh, makes clear that for a single-beam optical system with numerical aperture NA, axial resolution

$$d_z \approx \frac{2\lambda}{NA^2}, \tag{3.1}$$

is significantly worse than lateral resolution

$$d_{xy} \approx \frac{\lambda}{2NA}, \tag{3.2}$$

even for the highest NA systems. For $NA = 1.4$ (as with the highest-magnification oil-immersion objectives), $d_z = 2.9\, d_{xy}$, and indeed this 3:1 ratio is observed for the elliptical voxels written by the highest-resolution direct laser writing (DLW) systems that use such objectives [71]. As we have seen in Section 2.3.2, the NA values available with SLM-based

holographic projection are much smaller, due to the limited diffraction angle, typically $NA \approx 0.1$ for SLMs with the smallest-pitch pixels (See Figure 2.2).

This limitation of single-beam projection has been explored, but not overcome, by investigators developing algorithms to holographically define 3D optical fields with arbitrary intensity distributions at multiple axial planes [72,73], or in a 3D volume [49]. In all cases, axial feature spacing is 10-100-fold greater than the in-plane feature spacing. Whyte and Courtial [49], in fact provide an alternate useful perspective of the accessible spatial frequencies within a single-beam holographically reconstructed geometry. Recalling that a monochromatic optical field must obey the Helmholtz wave equation, it therefore must have its component spatial frequencies k_x, k_y, and k_z satisfy

$$k_x^2 + k_y^2 + k_z^2 = k_0^2 \tag{3.3}$$

where $k_0 = 2\pi/\lambda$. This is the equation of an Ewald sphere [74], and implies that the spatial frequency components in the projected pattern must be traded off against each other. When k_x and k_y are maximized, to attain fine in-plane features, the out-of-plane feature resolution defined by k_z must necessarily be minimized. A 3D reconstruction algorithm can be designed to optimize for all three directions, and indeed this is what Whyte and Courtial demonstrate, but they arrive at exactly the same NA-based limitation arising from illumination over a limited solid angle. To achieve a 3D-patterned optical field with equally high resolution in all three directions, an impractically large solid angle of illumination (at least 90°, or preferably much more) must be shaped by the illumination field.

The firm conclusion can therefore be made that a volume illuminated by a single optical beam cannot be patterned as a geometry having equally fine spatial resolution in all three dimensions. Another approach must be found to generate this type of 3D pattern.

3.1.1 The Beam-folding Solution

One possible means of doing this is to illuminate the volume using multiple patterned beams from different directions. Using multiple sources or independent SLMs imposes significantly

higher system cost and complexity, which is impractical for a prototype fabrication system exploring the feasibility of this approach. Instead, we generate the three patterned beams by deflecting three sub-regions of a single holographically-generated image using 45° mirrors, as shown in Figure 3.1(C). The three sub-beams enter the build volume from orthogonal directions, with each beam's axial resolution limitations compensated by the transverse patterns carried by its mutually orthogonal beams.

The choice of three beams is natural, corresponding to the three basis vectors in Cartesian 3-space. This multibeam superposition paradigm is one of the key innovations of this research that enables the volume-at-once concept, and the bulk of effort described in the following chapters of this dissertation is aimed at demonstrating this approach, exploring its possibilities and understanding its limits.

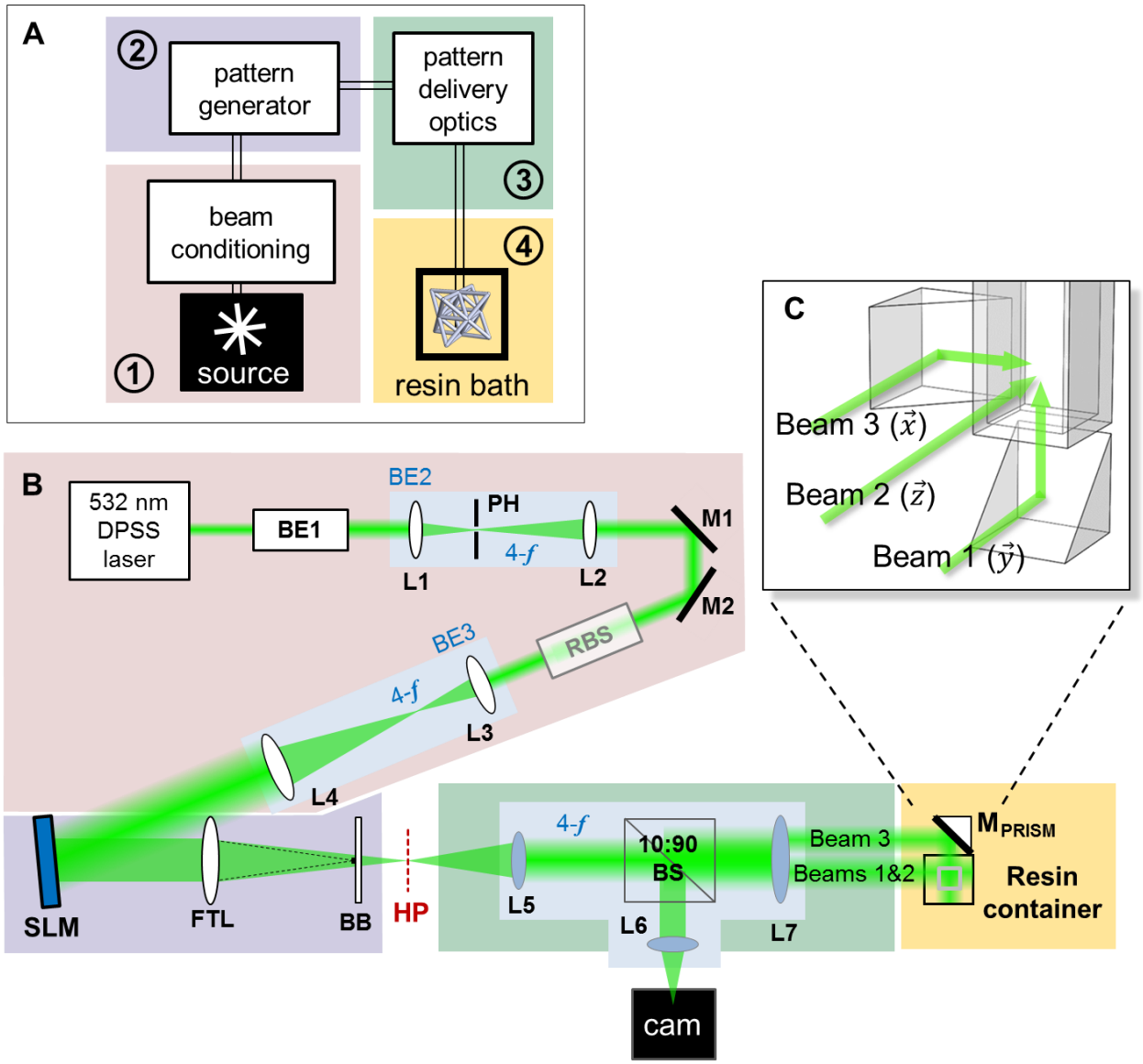

Figure 3.1: Overall design of the holographic 3D fabrication system used in this work. (A) Block diagram highlighting major functional subsystems, for which the colors of each block correspond to groups of elements in the panel below. (B) Optical layout conveying the light from source to resin. See main text for details. BE*n* – beam expanders (blue-boxed groups are telescope lens-pairs in 4-*f* configuration), L*n* – lenses, PH – pinhole spatial filter, M*n* – mirrors, RBS – refractive beam shaper, SLM – spatial light modulator, FTL – Fourier-transform lens, BB – high-pass beam block for eliminating un-diffracted light, HP – hologram plane, BS – beam-splitter. (C) Detail view of mutually-orthogonally-directed beams entering the build volume. Each beam is a sub-region of a single large-area holographic projection generated by the SLM. See Figure 5.1 for additional detail.

3.2 System-Level Design

Any photopolymer-based fabrication platform must comprise four key subsystems, displayed schematically in Figure 3.1(A). These are (1) the light source and conditioning optics, (2) an optical pattern generator, (3) projection and image-relay optics to deliver the light to (4) a liquid photosensitive resin bath. Figure 3.1(B) details the actual optical layout of the holographic 3D fabrication setup used for the bulk of experiments. Unless otherwise specified, all individual lenses are achromatic doublets. As a matter of convention, when referring to spatial coordinates in all discussions that follow, the direction of beam propagation (referred to as axial) is *z*, with the orthogonal directions (lateral or transverse coordinates) being *x* and *y*.

The source is a 532 nm continuous-wave (CW) diode-pumped solid state (DPSS) laser (Coherent Verdi V6), which is expanded in two steps (BE1 and BE2), on the way passing through a 25 μm pinhole spatial filter (PH) to improve the beam circularity and spatial coherence. Each blue-boxed region us a telescopic lens pair in the 4-*f* configuration. At the output of BE2, the beam is sized correctly for input to a refractive beam shaper (RBS - πShaper, AdlOptica). The beam shaper is only used for studies of beam profile, discussed further in Section 3.2.2.2 below, but not used during actual structure fabrication, described in Chapter 5. A final beam expansion telescope (BE3 – L3 and L4) ensure such that beam reaches the SLM with a diameter ($1/e^2$) of ~ 20 mm. This is scaled to approximately match the SLM diagonal, balancing the trade-off between illumination uniformity and efficient use of laser energy.

The optical pattern generator is a phase-only LCoS SLM (PLUTO VIS, HOLOEYE Photonics) with 1920×1080 pixels, 8 μm pitch, giving an overall display size of 15.36×8.64 mm. The 5-6 drive scheme ("bitplane sequence") is chosen to minimize electrically-induced phase flicker noise [75,76]. The phase response is tuned using a manufacturer-supplied calibration curve to give a linear function from 0 to 2.1π for 8-bit image data (grayscale values from 0 to 256). These choices result in the highest-contrast holographic image projection.

The Fourier transform of the CGH displayed on the SLM then gives the desired intensity distribution at the build volume (see Chapter 2). The *f*=250 mm lens (FTL) immediately after

the SLM produces this Fourier transform, with an image of the desired pattern first forming at the hologram plane (HP). Additional spherical phase added to the CGH at calculation time is used to de-focus the HP beyond the FTL's natural focal plane (where it would normally appear in focus) by approximately 40 mm, while blocking un-diffracted light at the FTL focal plane. See Section 2.4.1 for a brief discussion of this technique. This produces clean holographic reconstructions virtually free of undesirable content.

Finally, the light field reconstructed at HP is image-relayed through the 10% reflective arm of a 90:10 beamsplitter, via a 1.67× reduction telescope (L5 and L6) onto a CMOS camera (GO-5000M, JAI). This provides exposure monitoring, as well as image quality metrics and diagnostics, as described in the next section. The 90% arm of the beamsplitter passes the rest of the holographically shaped light down to the resin container via a 2× expansion telescope (L5 and L7).

The rest of this section reviews a few design considerations and optimization efforts for these subsystems, and describe high-level performance requirements they must satisfy. Before arriving there, however, this is a convenient opportunity to briefly discuss several useful diagnostics and measurements for evaluating their performance. We will consider such metrics for optimizing the design parameters of some of the subsystems.

3.2.1 Optical System Figures of Merit

For an optically-driven fabrication system, getting the necessary performance out of the optical components is the first critical requirement for controllable fabrication behavior, and therefore appropriate diagnostics need to be chosen. For diagnostic purposes, the holographically-projected images are directed onto the camera included in the setup (Figure 3.1) is used to take images of 2560×2048 pixels, each 5 μm square, with camera exposure values adjusted appropriately to capture the varying dynamic range of projected images.

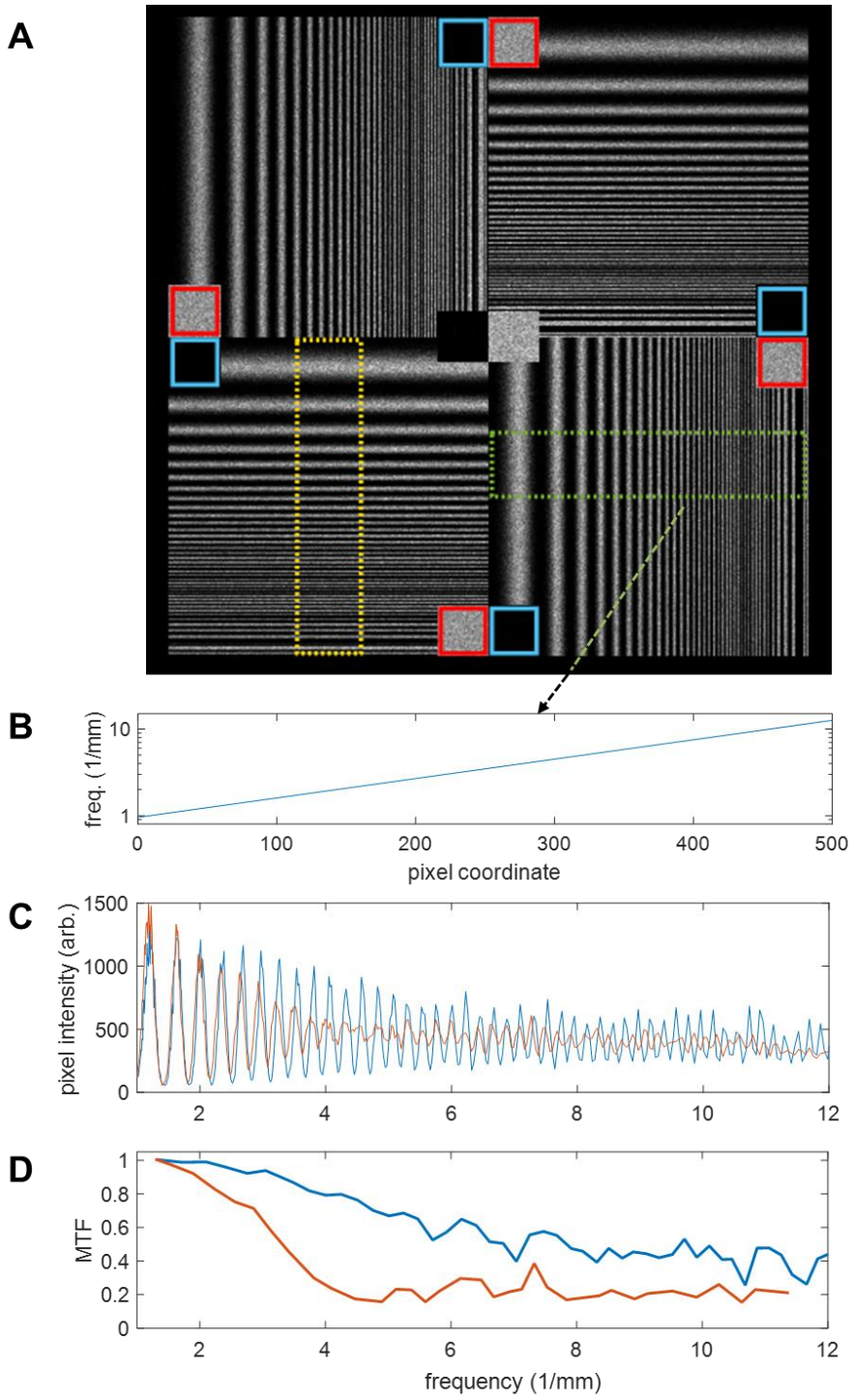

Figure 3.2. Image quality test pattern. (A) A MATLAB-simulated projection of a CGH for the test pattern, with overlays detailing the areas used to measure contrast (blue and red boxes) and MTF in the horizontal (green) and vertical direction (yellow box). (B) The frequency of the sinusoidal grating fringes varies exponentially as a function spatial coordinate. (C) A typical fringe intensity plot for horizontal (blue) and vertical (red) directions, and (D) the MTF calculated from them.

A variety of image quality metrics have been proposed [57,54], of which the two most relevant for pattern projection for photopolymer curing are contrast ratio and feature resolution. Figure 3.2 details a test image pattern for measuring image contrast and resolution measurements. For digital images, contrast ratio is most simply defined as the ratio of intensity between the brightest pixels (red boxes in Figure 3.2(A)), and background areas (blue boxes) not expected to receive any light. Feature resolution can be measured in a variety of ways, and here we choose to measure the system's modulation transfer function (MTF).

The MTF is a measurement of the loss in contrast for finer and finer image features. It is often used to measure component-level and system-level optical performance in imaging systems for applications ranging from microscopy to photography and machine vision. More formally, the modulation depth of an image area, M, is the ratio of its "AC component" to its "DC component" (the fluctuation in intensity as a fraction of the mean value):

$$M = \frac{i_{max} - i_{min}}{i_{min} + i_{max}} . \tag{3.4}$$

Here, i_{max} and i_{min} are the brightest and darkest pixels of the image area being evaluated. The MTF is the local modulation depth M_{loc} as a fraction of the global maximum modulation depth M_{glob} dependent on the spatial frequency of the local features, ξ. In the constrast/MTF pattern used here, the frequency, ξ, is an exponential function of the pixel coordinate, shown in Figure 3.1(B).

$$MTF = \frac{M_{loc}(\xi)}{M_{glob}} \tag{3.5}$$

The global modulation depth, M_{glob}, is calculated from the same blue- and red-boxed areas in Figure 3.2(A) used to compute the contrast ratio. is used as the global modulation depth. Separate MTFs are computed in both coordinate directions, since the performance is expected to differ due to the nearly twofold larger horizontal pixel count of the SLM, compared with the vertical.

An additional metric important for a laser-driven imaging system in particular is to measure spatial noise resulting from laser speckle. In the test pattern employed here, the standard deviation of intensity values from the white image areas serves as a measurement of noise.

3.2.2 Laser Source Considerations

If phase-only holographic beam shaping is to be used to produce patterns for 3D fabrication, the light must self-interfere, and therefore, must be coherent. Although holographic recording is possible with incoherent sources, for example with Fresnel holography [77,78], this is impractical for projecting light for lithographic patterning, so in this work the emphasis is on using coherent diffraction/interference. Non-laser sources such as LEDs have wavelength spectral bandwidths of at least 1-10nm, limiting their coherence length to a few micrometers. In addition, the light delivered to the SLM must ideally consist of flat phase-front plane waves, which implies spatial coherence, so from both these considerations laser sources are a must.

Though most of the experiments for this research here were carried out using 532 nm illumination, this wavelength is restrictive, since very few initiator choices are available with absorption at this wavelength. Moreover, any initiator molecules sensitive at 532 nm will thus be sensitive to room light, which is highly undesirable. The feasibility of using shorter-wavelength laser sources was therefore also evaluated in limited experiments to give the holographic 3D multi-beam superposition approach greater versatility. Although many photoinitiator molecules have excellent absorption in the mid- to near-UV wavelength range (200-400 nm), these wavelengths require the use of more expensive optical glass (fused silica, etc.), and present greater safety hazards. Here the preference was for wavelengths near 400 nm, since these have been used by many stereolithography-like platforms for free-radical polymerization. As Chapter 4 will later discuss, having modest light absorbance, as many photoinitiators do in this range, is actually an advantage for the volumetric 3D fabrication process.

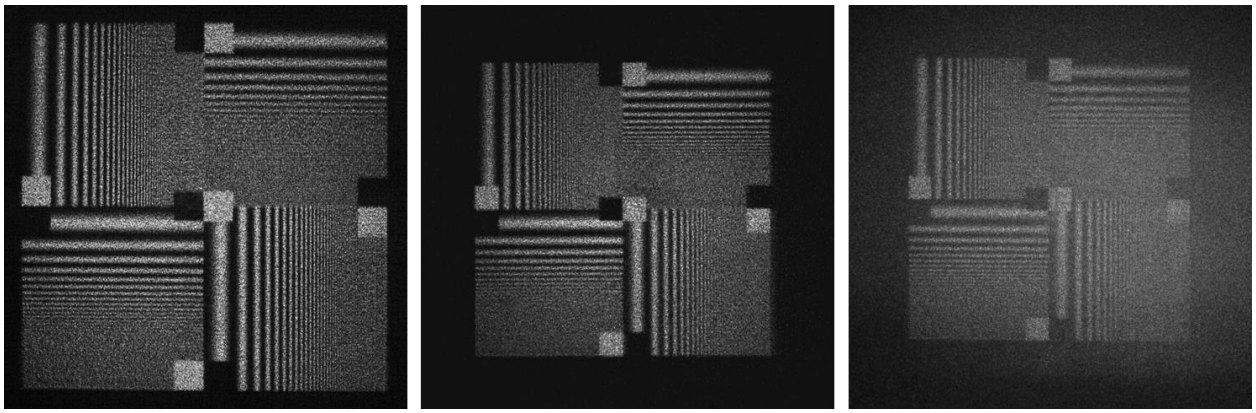

Figure 3.3. Laser Source Coherence Effect on Holographic Image Contrast. The three images are projections of the same test-pattern using (left) the 532 nm 6W DPSS laser, (center) the 405 nm 45 mW single-mode diode laser, and (right) the 405 nm 150 mW diode laser emitting on two-modes. See Table 3.1 for details and contrast measurements.

To this end, in addition to the 532 nm DPSS source, some tests were carried out using a single-longitudinal mode diode laser (CrystaLaser, Reno, NV) at 405 nm, and a higher-power 405 nm diode lasing on two adjacent modes (Toptica Photonics, Victor, NY). Some key parameters of these lasers are summarized in Table 3.1 below.

3.2.2.1 Coherence and Available Power

In terms of temporal coherence, the 532 nm DPSS laser is highly frequency-stabilized and emits on a single longitudinal mode, which gives it an extremely narrow spectral linewidth. It is specified by the manufacturer at < 5 MHz (<0.000005 nm), corresponding to a coherence length of >50 m.

The minimal coherence length requirement for the system here is much shorter: it must only exceed the path length differences for any light rays in the system that must interfere. In our

Table 3.1 Summary of Characteristics For Different Lasers Tested

Laser Type	Max. Power (W)	Spectral Linewidth (nm)	Coherence Length (mm)	Contrast Ratio
532 nm DPSS	6.0	5×10^{-6}	5×10^{4}	25.1
405 nm SLM diode	0.045	1×10^{-4}	1,640	13.6
405 nm 2-mode	0.15	0.5	0.33	5.3

configuration, this is only ~1-2 cm. However, additional coherence improves the contrast of reconstructed intensity fields at the build volume, thus benefitting lithographic fidelity, though at the expense of speckle noise. Figure 3.3 and shows a direct comparison between images of the contrast/MTF test pattern projected using the 532 nm and both 405 nm lasers, with Table 3.1 providing quantitative comparison of the contrast ratio from the three sources.

Laser spatial coherence is apparent from the beam profile shape and how closely it matches an ideal Gaussian function. Although spatial coherence can be improved by the use of spatial filtering (passing the beam waist through a pinhole), this operation imposes a penalty in available beam power. From experience with different quality beams, spatial coherence was found to be less critical than temporal coherence for image quality.

In terms of available optical power, in the holographic configuration of our system, about 10% of the total beam power incident on the SLM ends up propagating to the build volume[1]. It is trivially true that more power from a photopolymerization source is desirable for faster fabrication or coverage of larger areas. Higher power nearly always translates to bulkier and more expensive systems, and more spatial coherence likewise means higher cost. Among 405 nm sources, there is a trade-off between coherence and power output, and one of the side-issues explored here was to assess the minimal power requirements of the 3D volumetric process. As we will see from the fabrication results presented in Chapter 5, even as little as 1 mW from each of the three beams is sufficient intensity to successfully cure structures.

3.2.2.2 Optimal Beam Shape[2]

As we touched upon in Chapter 2, though phase-only liquid crystal SLMs have been extensively studied, calibrated, and optimized, the characteristics of the incident illumination have received

[1] Although manufacturer-cited and literature-reported diffraction efficiencies for phase-only SLMs are typically much higher e.g. 60%, such measurements are scaled to the 0th diffractive order mode power, rather than the total incident beam power.

[2] The material in this section is adapted from a paper presented at the Optical Society of America (OSA) 2016 conference on *Digital Holography and Three-Dimensional Imaging* held in Heidelberg, Germany, titled "Optimal Source Beam Shaping for Digital Holographic Lithography" [79].

little consideration. Nearly all work with SLM-based holographic image projection uses TEM_{00} Gaussian laser beam illumination, sometimes specified to be "slightly overfilled" [80], and in other cases under-filled [81]. The size of the beam relative to the SLM active area strongly affects the overall system power efficiency, imposing a trade-off with illumination uniformity, but quantitative optimization of these parameters has not been carried out. As one potential solution, a variety of commercially available refractive beam-shapers are able to convert a Gaussian beam profile to a "tophat," profile (approximately uniform intensity over a certain radius), with very high efficiency, while preserving the beam's phase front [82,83].

To measure how key beam shape parameters affect the quality of reconstructed holographic images, a closer study was carried out based on the image quality metrics developed in Section 3.2.1. Specifically, we compared the uniform illumination of a tophat beam with Gaussian beam profiles at different overfill ratios, OF. $OF = 1$ is defined as being a Gaussian beam whose $1/e^2$ intensity diameter (4σ) is matched to the diagonal dimension of the SLM. Larger beam overfill ratios represent more uniform intensity, with the limiting case being the completely uniform tophat profile. When the RBS is in use, its tophat output profile is image-relayed by the BE3 telescope in Figure 3.1(B) to the SLM. For Gaussian beam profiles, the RBS is removed, and a range of beam overfill conditions are obtained by switching out L3 and repositioning it appropriately.

An additional concept related to the effects of beam shape on image quality, hologram tiling is worth exploring. This has been suggested by some investigators as a means of mitigating illumination non-uniformity [64–66]. Here, tiling was evaluated by cropping the computed CGH to the centermost 1080×1080 pixels, and tiling this twice over the area of the 1920×1080 px area of the SLM. Further tiling of smaller pixel-count holograms was not attempted, as this quickly reduces the spatial resolution, since the overall size of the tiles decreases, limiting the intensity control to discrete points in the reconstruction plane (see Section 2.4.2).

Along with these experimental measurements, simulated projections were also tested as an ideal case, using simple 2D FFT transforms in MATLAB of the calculated complex-valued optical

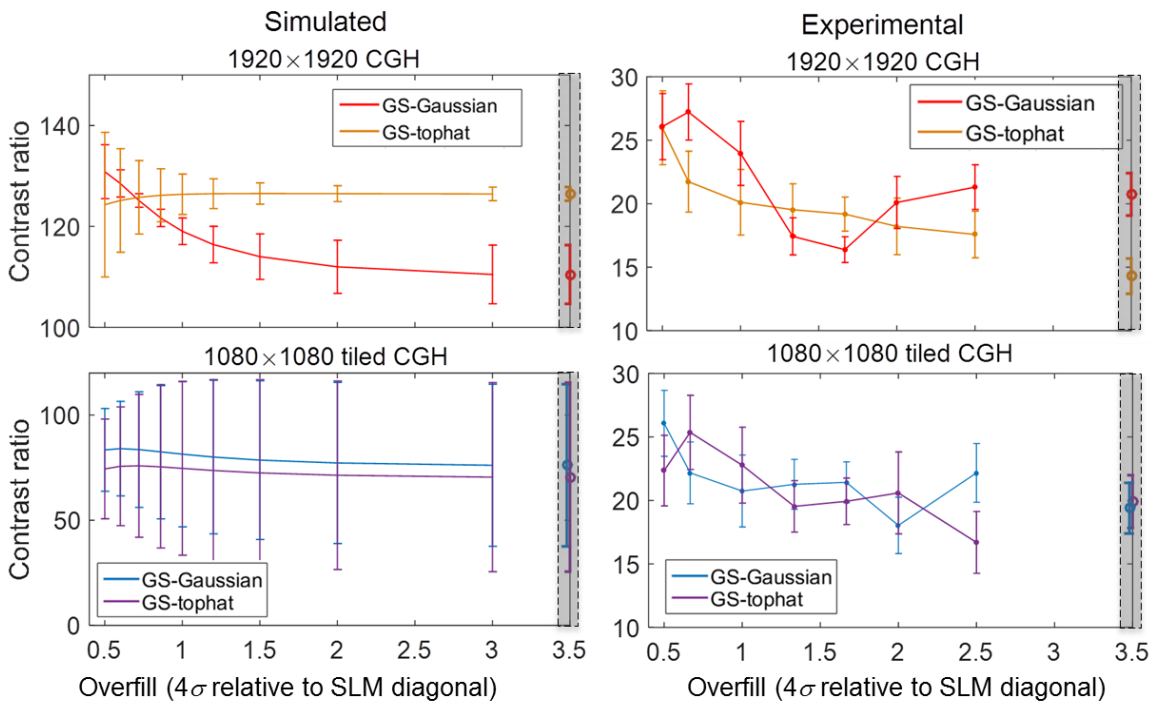

Figure 3.4. Laser source beam profile effects on the contrast and noise of projected images. The gray-shaded areas at the right edge of each plot are data from the tophat-profile beam.

fields, convolved with the calculated point-spread function of the projection lens. The optical fields comprised the CGHs as the phase and the appropriate illumination profiles as the amplitude. Here, another beam-shape parameter variation was also added, in which the illumination used during G-S algorithm interations for CGH computation (see Chapter 2) was either uniform (simulating a tophat) or Gaussian ($OF = 1$).

Figures 3.4 and 3.5 summarize the results of this study. Though the trends seen are not particularly strong, some useful conclusions regarding the choice of beam-shape can be made. First, the use of tiled holograms brings no benefit to projected image quality. Though experimentally, contrast and image noise are not significantly different with and without tiling, simulations suggest that tiling reduces contrast and increases noise. Tiling is therefore not worth incorporating from an image quality perspective, though calculating reduced-pixel-count holograms will speed up calculation time.

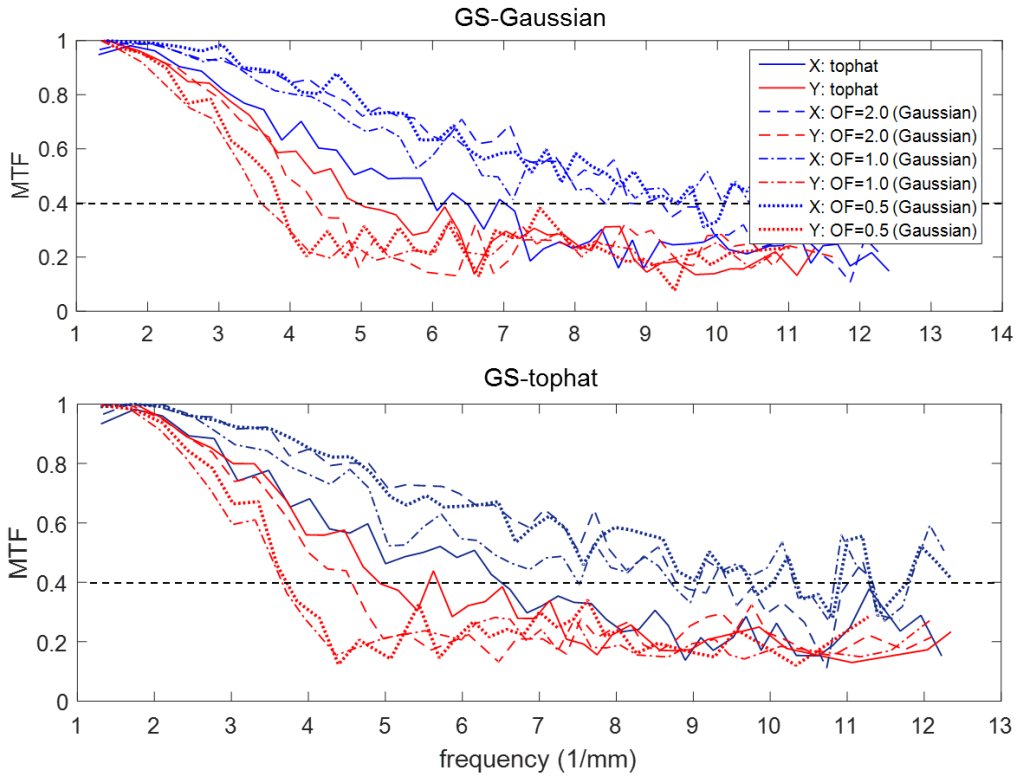

Figure 3.5. Laser source beam profile effects on holographic image feature resolution. MTFs for the tophat-illuminated condition are more equivalent for the two SLM axes than with Gaussian illumination profiles. The dashed line at MTF=0.4 provides an arbitrary reference threshold.

Neither experimental nor simulated results indicate that tophat-profile beams bring benefits in contrast and image noise. When using Gaussian-profile illumination, the dependence on overfill factor is weak, with slight contrast benefits seen experimentally for beams slightly underfilling the SLM. It is therefore appropriate to choose slightly under-filled illumination to prioritize the efficient utilization of source beam power. Interestingly, the simulations with full-size 1920×1920 CGHs (Figure 3.4 top left) imply that using tophat profiles in the G-S algorithm is preferable, though the experimental measurements (top right) do not support this.

Finally, the MTF measurements in Figure 3.5 add an interesting nuance to the use of tophat illumination: the significant difference between the horizontal and vertical MTF (blue vs. red curves) seen with Gaussian illumination is nearly eliminated with uniform illumination. That is, horizontal resolution worsens, while vertical resolution improves. This interesting detail bears

further investigations, but this has minimal impact on the overall conclusions of this study, so it remained outside the scope of this work.

3.3 Image Delivery Optics

This group of elements within the overall optical configuration controls the magnification of the reconstructed image at the hologram plane $I_{HP}(x, y)$, when it reaches the build volume. The image is scaled to fit the 10 mm dimension of the resin container, designed for mm-scale part sizes, with a magnification factor of approximately 2×. The final image-relay lens in the present system has a focal length of 250 mm (NA=0.1), with a field of view of 25×25 mm, and each beam's depth of focus is greater than 10 mm. As we saw in Figure 2.2, the NA of our SLM is smaller, approximately 0.03, and is therefore the element that has the strongest influence on the depth of focus, rather than the final image-relay lens. One practical benefit of this long depth of focus is that the unequal path lengths between the central beam and the folded side and bottom beams are inconsequential, as all three beams remain sufficiently in focus to overlap correctly without additional compensation. With a higher-NA system, focusing compensation by means of phase curvature may need to be applied to the folded beams (and not the direct central beam), which is only possible using holographic beam shaping.

3.4 Resin Formulation

The liquid prepolymer resin used for most of the experiments here is the short-chain monomer poly(ethylene glycol) diacrylate, with an average molecular weight M_n=250 (PEGDA 250). Irgacure 784[3] was used as the photoinitiator, because as it is one of the few initiators that absorbs at the 532 nm wavelength of our holographic source laser. Its manufacturer-supplied absorption spectrum is shown in Figure 3.6. Published estimates of its molar extinction coefficient at 532

[3] Bis(η5-2,4-cylcopentadien-1-yl)-bis(2,6-difluoro-3-(1H-pyrrol-1-yl)-phenyl) titanium; CAS # 125051-32-3

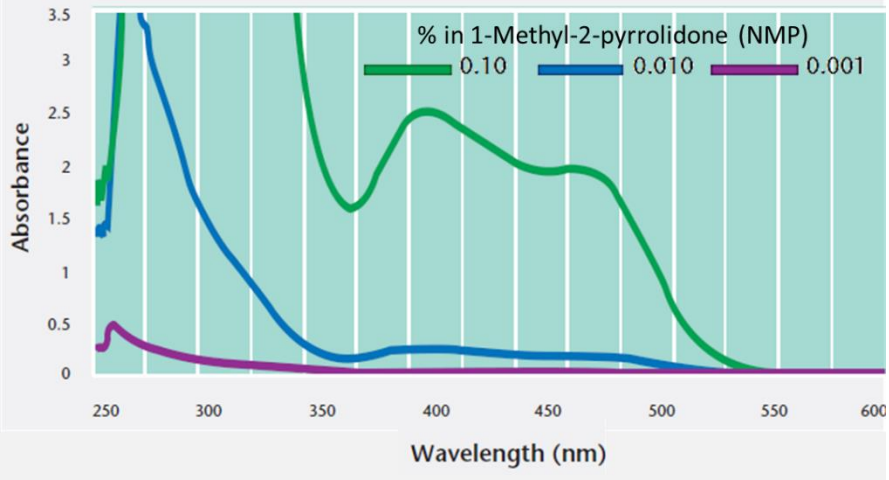

Figure 3.6: Manufacturer-supplied absorbance data for Irgacure 784. Reproduced and modified from Ciba Specialty Chemicals *Photoinitiators for UV Curing*.

nm, ε_{532}, are in the 100-150 L/mol/cm range [84,85], while direct measurement of absorbance from mixtures formulated for this work yielded in a value of approximately 45 L/mol/cm.

3.5 Chapter Summary

The material presented in this chapter provides system-level design considerations for a fully-realized holographic volumetric 3D fabrication system. The most important result is the necessity of overlapping several optical beams within the build volume to make up for the limited axial resolution available from any single-beam optical configuration. The natural choice in 3D space is to overlap three beams, which permits performance with equivalent resolution in all three spatial dimensions.

Only two beams may be used, entailing a corresponding reduction in geometric versatility along one dimension. Or additional beams beyond three may be used, coming from additional angles, but at the cost of more complex "folding" optics, and more complex resin container design to properly direct them into the build volume. The relative costs and benefits of this are largely geometry-dependent (for instance, structures with many 45°-oriented struts or planes will benefit from beams directed along the same angle). A rigorous mathematical treatment of this topic is

surely a fertile subject for future inquiry, but for the moment remains outside the scope of the present work.

Two other conclusions emerge from the study of optimal source beam characteristics. The first is that the use of refractive beam shaping to attain uniform illumination of the SLM (tophat-profile rather than Gaussian) provides only limited benefits, and mostly does not warrant the increased alignment stringency that it requires. The second is that reasonably high laser source coherence (approx. ~GHz or ~0.5 pm bandwidth or narrower) is needed to attain image contrast better than 10:1 for SLM-projected images, which is an approximate empirically-derived lower limit that allows sufficient contrast between cured and uncured photopolymer areas. These design constraints are then useful for bounding additional design parameters of other subsystems in the overall 3D fabrication platform.

Chapter 4

Photochemistry of Acrylate Resins

Free-radical initiated photopolymerization is an extensively-studied phenomenon [86,87]. It involves an interplay of several dynamic processes that include absorption of photons from the illumination source, a variety of chemical transitions, diffusion of reacting species, as well as the energy balance of these processes. While a complete treatment of this subject is certainly beyond the scope of this dissertation, there are several important dependencies that are critical to take into account for successful 3D volumetric fabrication system design. Because these dynamics are so complex and interrelated, we present only some of the parameters in absolute or quantitative terms, with others limited to being described in relative or qualitative fashion within the scope of this work.

In this chapter, we review a number of background concepts and the key physical and chemical frameworks relevant to designing a multibeam superposition-based volumetric 3D fabrication system. The treatment here is as general as possible, in order to enable broad applicability to any acrylate resin system. The specific application of these background concepts within the volumetric 3D fabrication platform are detailed in Chapter 5.

4.1 Main Reaction Mechanisms

In broad qualitative terms, the simplest photosensitive resin comprises a (usually liquid) monomer, and a photoreactive initiator species. Additional components, such as a photoabsorber (to control light penetration), additional monomer molecules (to control reaction rate or solution viscosity), and chemical quencher species (to minimize undesired polymerization) may be present, but are not required.

As in all radical chain reactions, the various chemical transformations that take place during photopolymerization can be grouped into three major processes, namely: initiation, propagation, and termination. Below, we summarize a simplified set of reaction mechanisms characterizing these processes, with the goal of retaining sufficient detail to understand the key dependencies of the process dynamics, while omitting much nuance that is not relevant for the scope of the present work (and studied extensively by other investigators).

Initiation is the generation of new radicals by photocleaving, which is the generation of primary initiator radicals due to absorption by initiator molecules (denoted as PI) of incoming photons with energy $E_{phot} = h\nu$ (the photons are of a frequency $\nu = \mathrm{c}/\lambda$, with Planck's constant h providing the proportionality between frequency and energy).

$$PI + h\nu \rightarrow R_1 \bullet + R_2 \bullet \qquad (4.1)$$

The two species resulting from photolysis are chemically distinct, but usually assumed to behave identically for polymerization reaction purposes, and we do likewise here, representing them generically as $R\bullet$ below. The initiation step continues as the radical attacks the carbon-carbon double bond of a monomer acrylate end-group M, forming a covalent bond as it transfers the radical to that acrylate.

$$R \bullet + M \overset{k_i}{\rightarrow} RM \bullet \qquad (4.2)$$

The reaction propagates as this newly-radical-terminated molecule in turn attacks the C-C double bond, bonding with an adjacent acrylate monomer end-group. The polymer molecule continues growing in chain-wise fashion, as its radical reacts and moves to an adjacent molecule's end-group. Such a molecule mid-propagation is referred to as a macroradical, indicated by $\mathrm{M_n}\bullet$:

$$RM_n \bullet + M \overset{k_p}{\rightarrow} RM_{n+1} \bullet \qquad (4.3)$$

The macroradicals are not necessarily linear molecules—this is the case only if each monomer molecule has just one acrylate end group. With multi-acrylate molecules (such as diacrylates like the PEGDA 250 used here), the growing polymer network can branch and cross-link. Finally, the reaction terminates when two radicals encounter each other, either joining into a

single molecule (recombination) or producing two separate non-radical molecules (disproportionation).

$$RM_n \bullet + R\mathrm{M}_\mathrm{m} \bullet \xrightarrow{k_t} RM_{\mathrm{n+m}} \tag{4.4}$$

$$RM_n \bullet + R\mathrm{M}_\mathrm{m} \bullet \xrightarrow{k_t} RM_\mathrm{n} + RM_\mathrm{m} \tag{4.5}$$

All reactions are assumed to be irreversible. Each reaction is described by a kinetic rate constant (k_i, k_p and k_t for initiation, propagation, and termination, respectively), and each reaction rate is the product of its rate constant and the concentrations of its respective reactants. Thus, generically:

$$r_x = k_x[X_n][X_m], \tag{4.6}$$

with a bracketed symbol denoting the molar concentration of that species. The relative rates of the reactions, and the resulting rate of polymerization, vary dynamically, depending on a complex interaction of parameters. The "constants" k_p and k_t, for instance, are not constant at all, but vary as a function of temperature, local resin viscosity, and double-bond conversion (with all three of these changing with reaction progress). The details of these kinetics have been extensively modeled and studied by others, and are not critical to the main focus of this work.

4.1.1 Influence of molecular oxygen

However, an additional aspect of radical polymerization reactions especially salient for the present work is the scavenging of radical species by molecular oxygen (O_2). When dissolved O_2 is present in the resin, for instance due to equilibration with an oxygen-containing ambient atmosphere, the O_2 reacts with available radicals (these can be both photocleaved initiator molecules, as well as macroradicals, hence denoted as $X\bullet$), competing with the chain initiation and propagation reactions of Equations 4.2, and 4.3.

$$X \bullet + O_2 \xrightarrow{k_{O2}} XO_2 \bullet \tag{4.7}$$

The resulting peroxide radicals do not contribute to polymerization and quickly lead to reaction termination. This inhibition process has been known for decades [88,89], as it presents problems for complete conversion of monomer to polymer. As early as the mid-1980s, Decker

and Jenkins characterized the chaining of peroxides produced during O_2 radical scavenging, and they and others have developed approaches to circumvent it [90,91]. More recently, Dendukuri *et al*. [30] used this inhibition behavior to enable a stop-flow lithography process, in which monomer was prevented from polymerizing at the walls of an O_2-permeable microfluidic channel, polymerized particles to be produced without sticking to channel walls. In similar fashion, O_2-inhibited polymerization against a gas-permeable membrane has been used to assist in layer-by-layer stereolithography systems [22,92].

The reaction rates for chain propagation and for radical scavenging by O_2 are given by $k_p[M][R\bullet]$ and $k_{O2}[O_2][R\bullet]$, respectively, where $[M]$, $[O_2]$, and $[R\bullet]$ are the concentrations of monomer, oxygen, and radicals, respectively. In low-viscosity acrylates (~10-100 cP), the O_2 reaction rate constant k_{O2} is many orders of magnitude higher (~10^7-10^8 L/mol/s) than that for chain propagation ($k_p \sim 10^3$-10^4 L/mol/s) [90,93]. Thus, in a region with O_2 present, the oxygen molecules will be first to react with the primary radicals generated upon initial light exposure, preventing appreciable polymerization from taking place, until sufficient O_2 has been consumed in the local vicinity for the propagation reaction rate to compete with radical scavenging by O_2, i.e. when $k_{O2}[O_2] \sim k_p[M]$. Decker and Jenkins [90] determined that in acrylate monomers similar to the PEGDA used in this work, $[O_2]$ must be reduced to ~10^{-6} mol/L from an air-equilibrated value of ~10^{-3} mol/L, i.e. two to three orders of magnitude. The time for this to take place is referred to as the "induction time" of the reaction, or "inhibition time," designated t_i.

In Chapter 5, we will present experimental measurements of t_i, and identify the relevant practical process parameter bounds that relate to it. Here we continue to discuss general considerations.

4.1.2 Reaction Induction Time

This induction time plays a critical role in the polymerization process. It is this oxygen inhibition mechanism that provides the nonlinearity in the polymerization process that allow spatial confinement in three dimensions. A simple calculation of t_i may be made from the

following relationship:

$$t_i \approx \frac{[O_{2,\mathrm{EQ}}]}{R_{init}}, \tag{4.8}$$

where $[O_{2,\mathrm{EQ}}]$ is the dissolved oxygen concentration pre-reaction in equilibrium with the ambient, and R_{init} is the reaction initiation rate (equivalent to the photoradical generation rate). As mentioned, $[O_{2,EQ}]$ must be nearly fully depleted for appreciable polymer formation to begin. As the induction period ends, polymerization of the resin begins to change the density and refractive index of the mixture, and the polymer becomes visibly discernible (see also Section 5.2). At this point, the material can be considered cured, albeit incompletely (see Section 4.3 below). Attaining complete curing in radical-initiated acrylates can be a challenge, and improvements on this front will be important. Nevertheless, Equation 4.8 can be used as a reasonably accurate estimate of the length of the induction period, but only under two simplifying assumptions.

The first assumption is that R_{init} does not change during the exposure. This is typically the case under constant illumination conditions, but only if the volumetric absorbance of the resin does not change with time as the reaction progresses. However, if the starting photoinitiator concentration $[PI]$ is low enough for a significant fraction of available PI molecules to be cleaved and scavenged during the induction period, R_{init} becomes time-varying and the induction time estimate becomes more complex.

The second key assumption is that the exposure time is shorter than the timescale of O_2 diffusion within the resin over length scales relevant to features being built. Below, we examine situations in which these assumptions do not hold.

4.2 Absorbed Photon Energy

The initiation rate R_{init} depends on local photon absorption conditions in each region of the resin. It can be most generally written as

$$R_{init}(x,y,z) = \varphi \frac{I_{abs}(x,y,z)}{N_A h\nu} \tag{4.9}$$

with $I_{abs}(x,y,z)$ denoting the absorbed light power per unit volume (units of mW/cm^3) at a given resin location. The spatial coordinates are explicitly notated here, as we are interested here specifically in bulk phenomena, and depth-dependent light attenuation constitutes an important variable in the volumetric fabrication process. In Chapter 5 we more carefully consider the variation of this quantity in all three dimensions, but here we focus our attention on the axial coordinate (z) as a beam propagates deeply into the resin. Other quantities in Equation (4.9) are φ the quantum efficiency of radical generation, and the denominator to convert the light intensity to molar photon flux (just as for Equation 4.1).

To successfully produce volume-at-once structures by multibeam superposition, all regions of the resin to be cured need to simultaneously accumulate the energy required for curing. This means a uniform initiation rate R_{init} throughout the curing regions, and therefore uniform volumetric absorption of light energy I_{abs}. Completely uniform absorption is, of course, unphysical, so in the next section, we examine the physico-chemical resin parameters that govern the spatial variation of this absorption.

The depth-dependent light absorbance $I_{abs}(z)$ is derived from the light attenuation profile, given by the Beer-Lambert law, which relates the attenuation of light in the resin due to a single absorbing dissolved species to the concentration and absorptivity. Absorbance is defined as

$$A = \log_{10}\left(\frac{I_0}{I(z)}\right) = \varepsilon[PI]z \tag{4.10}$$

Here, I_0 is the illumination intensity at the resin surface, and A is the absorbance of the solution, and we see the linear dependence on the path length (or penetration depth) z, the molar extinction coefficient, ε, of an absorbing species, and its concentration $[PI]$—the relevant absorber here is the photoinitiator. For generality of the analysis, we group the initiator concentration and extinction coefficient into a single absorption coefficient

$$\alpha = \varepsilon[PI] \tag{4.11}$$

with units of inverse length. This parameter has the advantage of being readily obtained directly

from a spectrophotometer measurement, which gives the resin absorbance from detecting the light transmitted through a sample. Because cuvette path lengths are manufactured to tight tolerances, the measurement provides a high-quality value for α without requiring precise knowledge of ε or measurement of $[PI]$. The absorbance is then simply $A = \alpha z$.

Thus, inverting the Beer-Lambert definition of absorbance, the depth-dependent attenuation profile through a sample

$$I(z) = I_0 e^{-2.3\varepsilon[PI]z}. \tag{4.12}$$

The actual volumetric absorbance is obtained from the derivative of $I(z)$ with respect to the resin depth:

$$\begin{aligned} I_{abs}(z) = \frac{dI(z)}{dz} &= 2.3\varepsilon[PI]e^{-2.3\varepsilon[PI]z}I_0 \\ &= 2.3\alpha e^{-2.3\alpha z}I_0. \end{aligned} \tag{4.13}$$

We define the pre-factor multiplying I_0 in Eq. (4.13) as a volumetric absorbance factor.

$$a_V(z) = 2.3\alpha e^{-2.3\alpha z} \tag{4.14}$$

Figure 4.2 summarizes the light intensity attenuation profiles $I(z)$ for various values of α as well as the value of $a_V(z)$ derived from each one. It must be emphasized that this analysis is completely general: so long as the parameter α is known (and absorption, rather than scattering is the dominant process in the resin), the results do not depend on the actual initiator concentration, illumination wavelength, nor specifics of the resin.

In situations when the light intensity does not vary significantly through the depth of the resin, such as thin films, the exponential can be omitted, so that $I_{abs}(z) \approx 2.3\alpha I_0$ and Eq. (4.9) simplifies to $R_{init} = 2.3\ \varphi\alpha I_0/N_A h\nu$. In the bulk fabrication scenario, this approximation may be retained for small values of α, below approximately 0.2, for which the absorbance over the entire depth profile varies by <20%. The more general approach is required, however, for most volumetric multibeam situations.

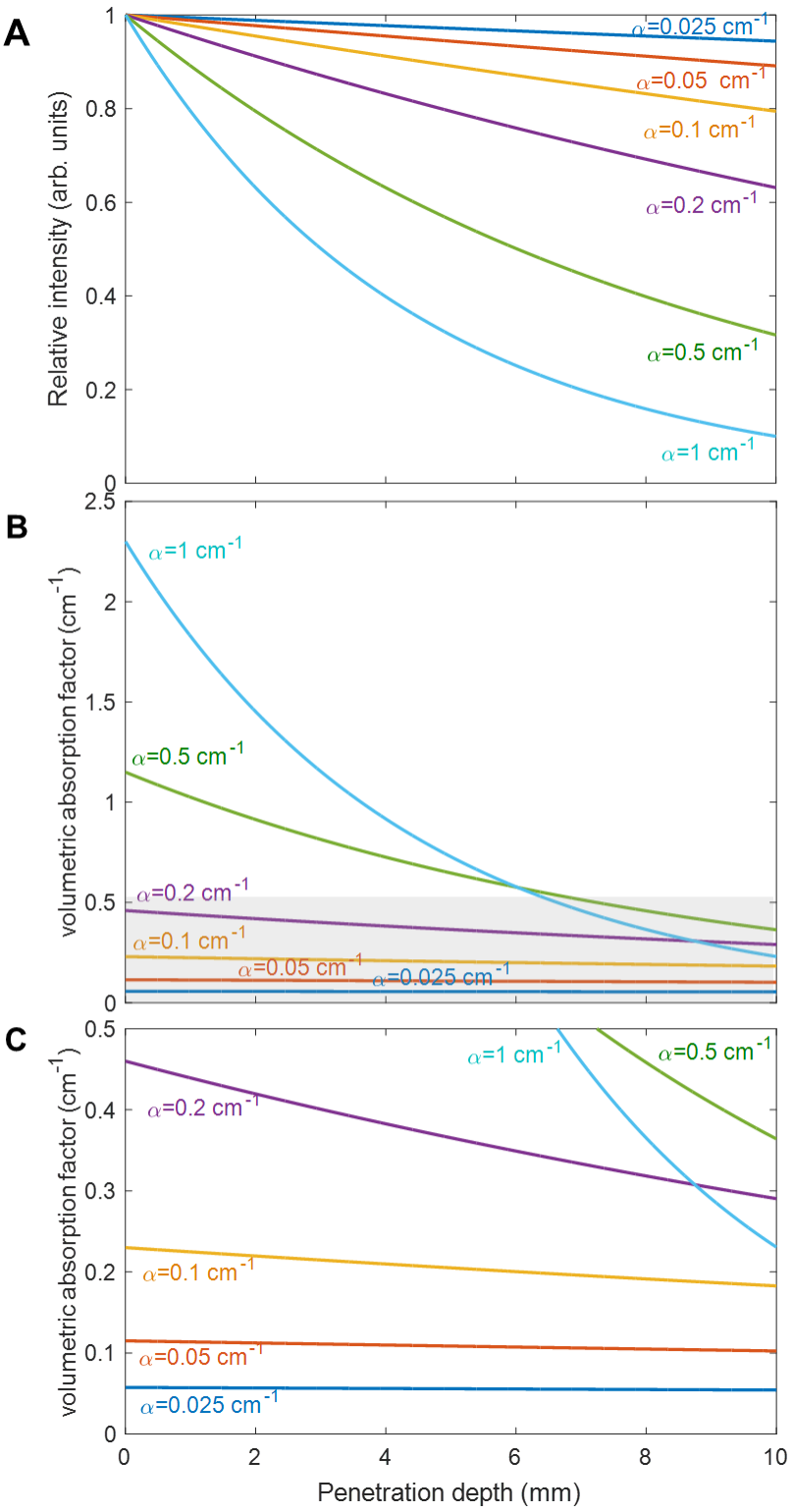

Figure 4.2: Depth-dependent light absorption in resins. (A) shows Eq. 4.10, $I(z)$, and (B) shows Eq. 4.13, $a_V(z)$ on the 10 mm spatial scale relevant to the present work, with (C) showing a closer view of the gray region in panel (B).

We therefore find that the minimum variation in absorbed energy is achieved when α is small, that is when either one or both of $[PI]$ and ε are minimized. As a practical matter, however, since it is the product of α and I_0 that controls the induction time, and therefore the timescale for part curing, the available power from the illumination source will dictate how α is to be chosen. A related practical limitation also arises from the need to keep α small. As the photoinitiator concentration $[PI]$ is decreased, the molar concentration of PI molecules must not drop below the molar concentration of dissolved O_2 molecules. As mentioned above in Section 4.1.2, this situation results in a nearly-complete depletion of photoinitiator by oxygen scavenging, and the induction time t_i extends substantially or even indefinitely, with structures failing to form.

Figure 4.3 summarizes the interplay of resin absorbance, illumination intensity, and exposure time, assuming the curing time is dominated by t_i, at an equilibrium O_2 concentration, $[O_{2,\mathrm{EQ}}] \approx 1$ mM. The calculations that yield these results are given in Appendix B. It is important to emphasize here that this analysis remains completely general, independent of source wavelength, as long as physical quantities are appropriately scaled in molar terms.

This analysis allows formulation parameters to be chosen based on desired curing behavior, or on the available incident light power, or on available initiator species. For instance, lines of constant ε indicate the behavior of a particular initiator species mixed at different concentrations. Or, given a laser source with a certain maximum power output, appropriate resin formulation conditions may be designed. In general, with an initiator and source wavelength selected, a resin's curing behavior may be predicted from the concentration $[PI]$ and its corresponding α value. To avoid reaching the PI-depletion regime, a resin must be formulated to reside in the right half of this plot, with $[PI] > 2$ mM. Lower values of α, and thus higher irradiances will be required for large resin containers, in which the absorption must be kept uniform over a larger spatial extent (see Section 5.1). Conversely, for producing smaller overall parts with finer features, a smaller resin container, and higher values of α may be used.

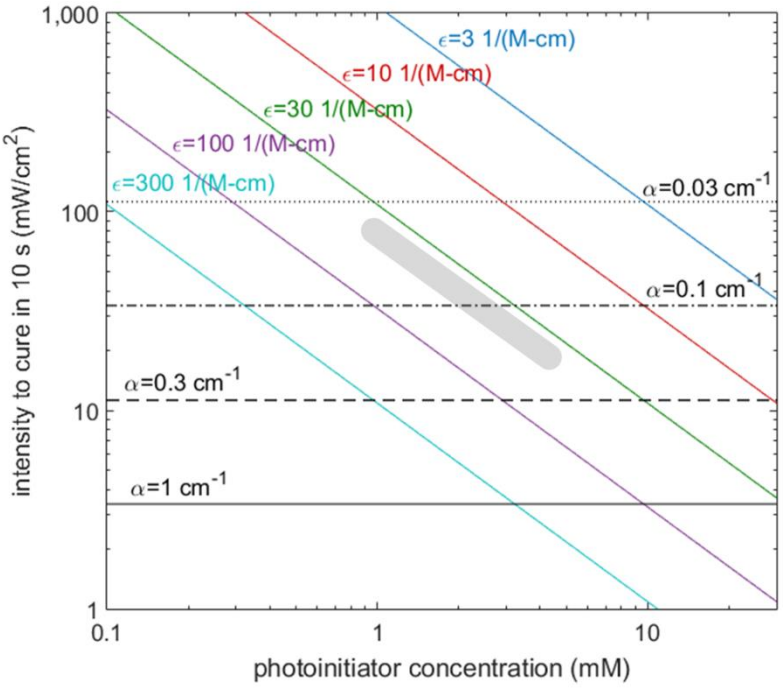

Figure 4.3: Summary of resin parameters and curing times. The approximate range of conditions used for the work described in Chapter 5 is denoted by the gray-shaded region.

4.3 Degree of Cure

Thus far in the discussion, the polymerization reaction has been examined in detail through its induction period, at the end of which the polymerization rate increases dramatically and a significant fraction of monomer molecules begin to be converted to polymer. The extent to which this takes place is intuitively termed "degree of cure," (DOC) but more formally it is defined as the conversion fraction of C-C double-bonds to single-bonds. This conversion is directly measurable by methods such as Raman scattering spectroscopy [94] or infrared spectroscopy [89] methods, by measuring the relative area of spectral peaks corresponding to the relevant interatomic bonds.

Polymer curing is not a digital "on-off" process. As the polymerization progresses, the material gradually transitions from liquid to solid, passing through a threshold known as the gel point (typically defined in rheological terms, at the point when the storage modulus exceeds the loss

modulus). The conversion fraction at the gel point is highly dependent on the specific pre-polymer chemistry, and is complex to measure. Flory-Stockmayer Theory [95–98] can be used to estimate that gelation for a di-functional monomer (such as the PEGDA 250 used in this work) takes place at 0.33 conversion. We will touch upon the issue of DOC again in Chapter 5, as we specifically consider the formation of structures during the 3D volume-at-once process.

4.4 Other Resin Considerations

Two other aspects of photopolymer behavior are important in any polymerization reaction, and especially to the 3D volumetric fabrication process of this thesis: thermal behavior, and diffusion of dissolved and reacting species.

4.4.1 Thermal Effects

Bond formation by radicals linking together acrylate functional groups is an exothermic process. Heats of polymerization can be ~10^4-10^5 J/mol, depending on the monomer in question [99,100]. Heat evolved during the reaction raises the local temperature, which affects all resin parameters from rate constants to species diffusivity. Although detailed analysis and temperature-dependent behavior is beyond the scope of this work, one practical consideration that comes into play in the 3D volumetric system is the possibility of convective motion induced in the resin due to heat evolved in the polymerizing structure. If the polymerization proceeds too quickly, the rate of thermal energy produced overwhelms the resin's ability to dissipate heat (dependent on its thermal diffusivity), setting up buoyant convection. In some of the experiments that will be described in Chapter 5, convective upward motion of curing parts was observed, confirming this phenomenon. Balancing the reaction rate against the thermal timescales to avoid convection becomes another consideration when formulating a resin. The resin's viscosity is another parameter that may be used to manage unwanted convection.

4.4.2 Diffusion of Reacting and Dissolved Species

During the reaction, every chemical species present can diffuse throughout the reaction volume, and diffusion coefficients drop as the reaction proceeds. Because a molecule's diffusivity, D, is a function of the molecule's size, r, dissolved molecular oxygen is usually the most mobile, since is the smallest species present in the liquid resin. During the induction period t_i, the re-diffusion of O_2 into illuminated regions where it is being depleted is a key process that affects the total length of this period. The diffusivity of all species is also inversely dependent on the mixture viscosity, η, given by the Stokes-Einstein relation, $D = k_B T/6\pi\eta r$ (valid for dilute spherical particles or radius r at low Reynolds number, and providing a reasonable first-order approximation here). Since the timescale for diffusion over a certain length scale is inversely proportional to the diffusivity, that time will be directly proportional to the viscosity: $\tau_D \propto \eta$. Similarly to convection management, viscosity can be used to control O_2 diffusion.

4.4.3 Resin Stability

The photoinitiator used in this work presents a cautionary note. Irgacure 784 is an example of an initiator for which a measurement of the absorption coefficient α may not sufficiently characterize its performance. As a titanocene (metal-coordinated compound), Irgacure 784 exhibits poor chemical stability once solubilized. In addition to degradation by dissolved ambient oxygen, the manufacturer also in the product literature that in the "presence of donor molecules (e.g. ketones, amines, cyanates and others), a slow ligand exchange reaction may occur leading to decomposition." Acrylate species are also among those that can lead to decomposition.

In our resin formulations, this is characterized by a slow upward drift of the value of α, even if the mixed resin is kept completely in the dark. Increases in α of 0.05 to 0.1 are measurable over timescales of 3-10 days, and substantially more than that after a few weeks. As α rises, however, the actual photo-activity of the initiator decreases, evident from increasing cure times. Thus, a

measurement of α, as described in Section 4.2 above, is only valid to correctly predict the performance of this resin when it is freshly mixed.

As a point of contrast, another commonly-used stereolithography initiator, Irgacure 819[4], dissolved in the same PEGDA-250 monomer, remains stable for much longer timescales, with α and photo-activity unchanging over months within the experimental measurement uncertainty. In general, caution must be taken to ensure that a resin shelf-life limitations or other confounding factors do not affect the process design.

4.5 Chapter Summary

Having established a firm footing for understanding the photopolymerization process, we are prepared to properly investigate its specific behavior during volumetric structure fabrication. We now have the framework required to understand and quantify depth-dependent energy absorption by the resin, which controls 3D structure formation. These energy absorption profiles define the uniformity of curing over the 3D volume, indicating that the volume absorption coefficient (the product of PI mola extinction coefficient and its concentration) should ideally not exceed 0.2 at the full depth of the resin volume. In the next chapter, a compensation scheme will be presented, which can extend this operating range somewhat.

We have also seen the critical role played by the inhibitory effect of dissolved O_2. The induction phase of the reaction, during which essentially no polymer is forming, provides the critical "threshold" behavior that enables the 3D structure to be confined in space. That is, oxygen inhibition allows regions where the superimposed light intensity is sub-threshold (i.e. where only one or two beams are present, rather than all three beams) to remain unpolymerized, when the curing dose in three-beam regions has already been attained. This has similarities with two-photon polymerization (2PP), also assisted by an O_2-dependent thresholding behavior [101]. However, in 2PP, achieving simultaneous absorption of multiple photons requires extremely

[4] Phenylbis(2,4,6-trimethylbenzoyl) phosphine oxide; CAS #162881-26-7

high laser fluences (~TW/cm^2) [102] only available from expensive femtosecond laser sources, whereas the multibeam single-photon approach explored here requires only modest source intensities.

The analysis developed in this chapter also yields a quantitative first-order model for predicting the ~1-10s-scale curing times required for the typical resins used for this work. At the same time, because much of the curing light energy is used to deplete molecular oxygen, rather than to form the structure, efficiency gains (and likely geometric benefits) may be realized using resins with lower O_2-solubility, or controlled equilibrium dissolved O_2, or entirely free of molecular oxygen, with a different chemical species used as an inhibitor.

Therefore, from a photochemical process viewpoint, an ideal resin for 3D volumetric multibeam fabrication should have the following characteristics:

- Low but nonzero O_2 solubility in the liquid prepolymer
- A photoinitiator with a small molar extinction coefficient ε at the operating wavelength (~10 L/mol/cm or lower)
- High resin viscosity (~0.5-5 Pa-s)

The chemical components used for the experiments in this work only meet some of these requirements. These components were chosen largely based on availability and prior experience with similar photopolymer processing. The availability and process characteristics of materials for formulating resins that better align with these criteria is a key topic for further investigation.

Chapter 5
Three-Dimensional Volumetric Structure Fabrication

This chapter brings together all of the component subsystems detailed in previous chapters, describing the complete holographic fabrication process used to produce 3D volume-at-once structures. It describes the beam compensation scheme that allows the curing energy to be delivered to all regions as necessary. Continuing to a systematic study of key fabrication parameters, we develop a fuller understanding of the combined optical-photochemical process within the framework developed in the previous chapter. This allows us to define practical bounds within the parameter space. We present structure fabrication results under a variety of conditions, and discuss advantages, limitations and challenges for the presently-configured system.

5.1 Pattern Generation for Multibeam Superposition

The first step for the successful fabrication of 3D parts requires the computation of an image pattern to project for the superposition of the three beams. This is a two-step process, with the first step being the decomposition of the 3D geometry into projections along orthogonal directions. The second step is to calculate the compensating lateral intensity gradients to be applied to each beam, based on resin attenuation measurements, in order to have all cured regions of the part accumulate the target curing dose simultaneously.

Decomposition of the target geometry into orthogonal projections is currently an empirical process. In the simplest terms, each of the three images is the 2D projection of the target geometry along each direction. As this is currently a purely manual design process, relying on

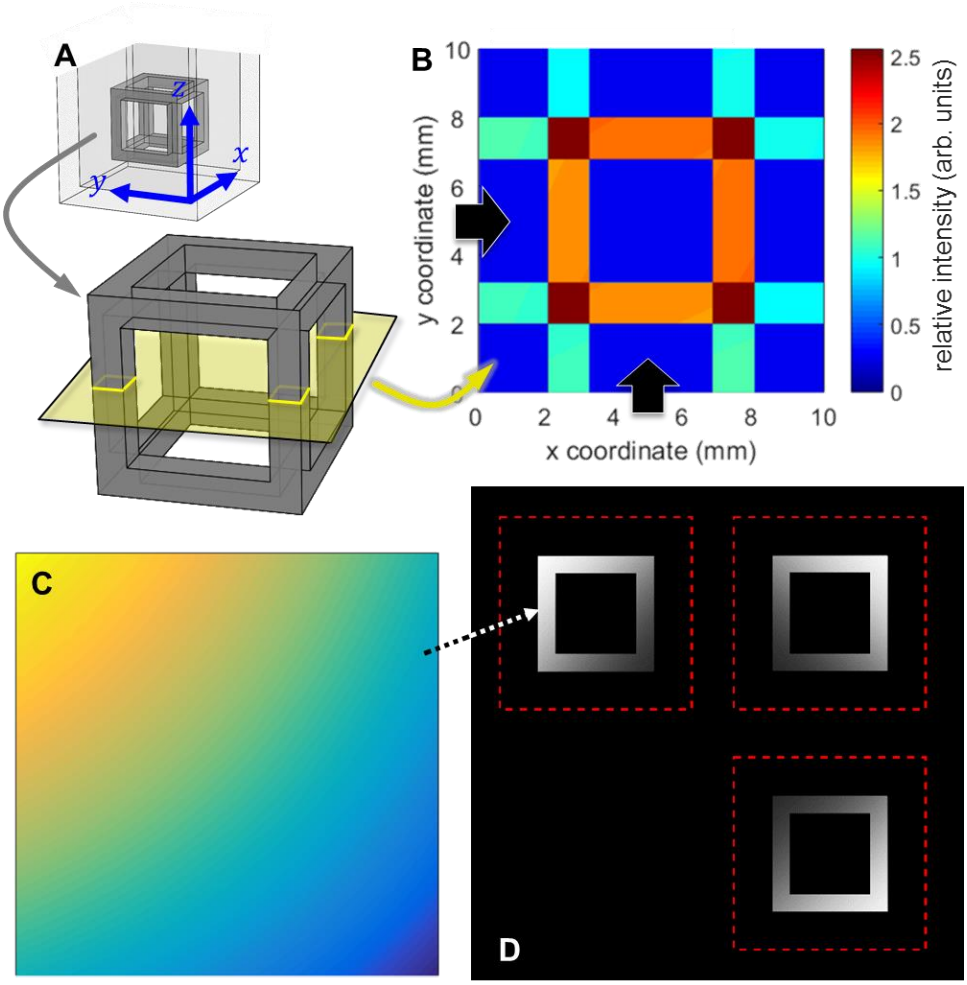

Figure 5.1: Set-up of 3D multi-beam attenuation model and mutual beam compensation. (A) The target position of the cube in the resin container, the relevant coordinate system, and a sample horizontal plane, for which the intensity distribution (normalized to the intensity of a single beam at the container wall) due to 3-beam illumination is shown in (B). Panel (C) is a typical 2D weighting function (shown in color to emphasize the curvature) used to adjust the intensity distribution in each beam, with (D) showing a full 3-beam intensity-compensated image projection, which is then input into the CGH computation algorithm. Red dashed boxes indicate the approximate extent of the 10×10×10 mm build volume.

operator intuition, this is an area ripe for more detailed investigation, outside the scope of this dissertation.

5.1.1 Mutual Beam Compensation

The beam compensation scheme is derived from a comprehensive 3D intensity distribution model, developed based upon the Beer-Lambert law. The model is used for calculating the

required transverse intensity gradients for compensation of depth-dependent energy absorption in the resin. The compensation requirement is for 3-beam overlap regions to receive the same peak energy dose, which allows the entire 3D structure to cure simultaneously, while regions receiving less than the cure dose remain unpolymerized (see Section 5.2 below and the discussion surrounding Figures 5.4 and 5.5, especially Equation 5.4 for measuring and predicting the actual energy dose for curing). Once the required transverse compensation gradients are computed, they are applied to the projected images prior to CGH computation (see Section 2.2.1), resulting in the desired redistribution of light energy at the build volume by the generated CGH phase pattern.

Figure 5.1(A) and (B) summarizes the 3D model, which is set up in a 10×10×10 mm volume (the MATLAB code with the complete details of this set of calculations can be found in Appendix B). For each axis, the projected image beam enters the resin at the 0 coordinate, and propagates in the positive direction. The beams are assumed to be prismatic (i.e. the light pattern does not vary along the propagation direction), which is a good approximation of the low-NA (long depth-of-focus) optical system described in this work. The projected cube geometry is 6 mm on a side, centered in the build volume, with each cube face 2 mm from the adjacent container wall. This structure provides a generic geometry for calculating the transverse compensation for any geometry that does not exceed its size, since the cube edge features are located at the extremes of the relevant volume. There they experience the greatest intensity nonuniformity, which results in the most variation in volumetric energy absorption. Therefore, if the difference between the extremes experienced by the cube edges can be adequately compensated, features in the interior of the volume will also be sufficiently compensated.

This compensation is computed from the spatial variation of the volumetric absorption factor $a_V(x, y, z)$ as defined in Equation 4.14. The product of $a_V(x, y, z)$ [units of 1/cm] and the illuminating beam intensity $I(x, y, z)$ [mW/cm^2] is the absorbed optical power per resin unit volume $I_{abs}(x, y, z)$, which directly translates into photoradical generation rate (see Equations 4.9, 4.12 and 4.13). The compensation gradient is therefore calculated as a 2D weighting

function $I_{adj}(x, y)$ to adjust the beam intensity of the three projected image subcomponents ($I_{adj}(x, z)$ and $I_{adj}(y, z)$ are simple rotations of the $I_{adj}(x, y)$ function). Figure 5.1(C) shows a typical $I_{adj}(x, y)$ compensation function, and the resulting intensity-adjusted image for the cube geometry is Figure 5.1D.

The volumetric absorption factor is greatest at the corner of the cube nearest to where all three beams enter the resin (and the spatial coordinates have their minimal values within the cube volume) $a_{V,max} = a_V(x_{min}, y_{min}, z_{min})$; conversely, the corner farthest downstream for all three beams has the minimal value $a_{V,min} = a_V(x_{max}, y_{max}, z_{max})$. For each beam propagation direction, the adjustment gradient is therefore

$$I_{adj}(x) = a_{V,min} + a_L(x) + a_L(x_{max}). \tag{5.1}$$

Here, $a_L(x)$ denotes a "lost absorption" value, which is the amount that needs to be compensated; i.e. it is proportional to the deficiency in absorbed energy farthest from the beam source relative to the side nearest the beam source, due to attenuation in the resin

$$a_L(x) = \frac{a_{V,max} - a_{V,min}(y)}{2}, \tag{5.2}$$

The factor of 1/2 accounts for the fact that for each beam two orthogonal beams are providing compensation. Along each direction in a particular z-plane, a_L is a function of the other beam's attenuation (hence $a_L(x)$ is a function of y and vice versa). The 2D intensity adjustment function $I_{adj}(x, y)$ is then simply the product of the normalized $I_{adj}(x)$ and $I_{adj}(y)$ functions.

Figure 5.2 summarizes the results of the optical attenuation model. Simultaneously with calculating the required intensity gradient, this model permits a process designer to determine the uniformity of the resulting intensity distribution. We calculate this uniformity parameter as the relative standard deviation (RSD = standard deviation as a percentage of the mean value) of the peak 3-beam overlap absorption factor values near all eight corners of the cube. These sample areas are boxed in white in Figure 5.2A, and Figure 5.2B presents uniformity results from the simulation for a range of values of the absorption coefficient α as defined in Equation 4.11.

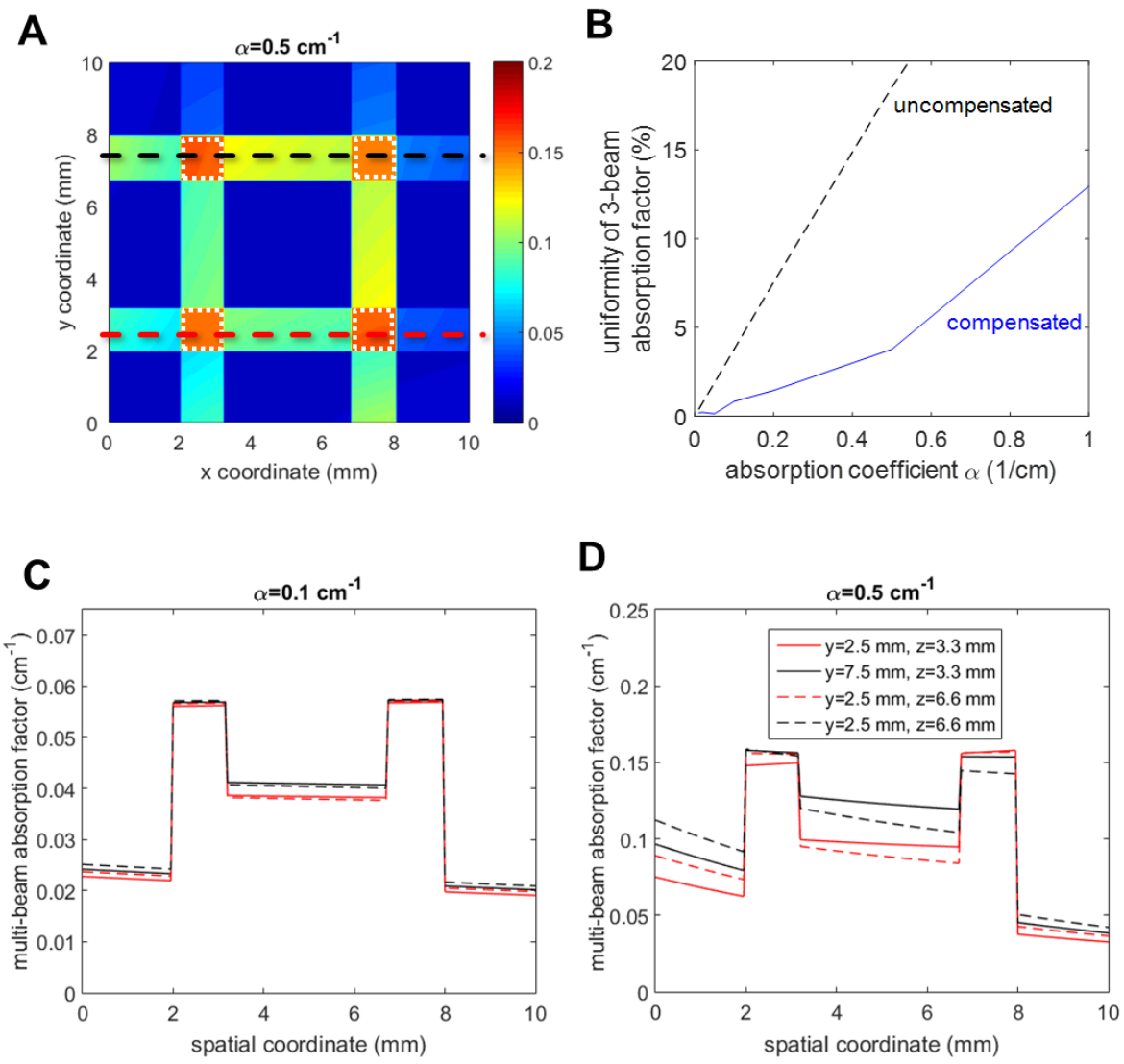

Figure 5.2: Multi-beam mutual compensation limits. (A) Plots a typical 2D plane distribution, similar to that shown in Fig. 5.nA, but here showing the variation in the volumetric absorption factor, rather than light intensity. The four white-boxed locations of maximum intensity are averaged at two different *z*-planes near the extremities of the cube, and their RSD is computed as the uniformity parameter in (B). Panels (C) and (D) show single *x*-coordinate-dependent absorption factor plots, for values of α that yield well-compensated ($\alpha = 0.1$ cm^{-1}) and borderline inadequately compensated ($\alpha = 0.5$ cm^{-1}) maximum absorption factors, respectively. Each plot shows two different *y* locations, corresponding to the red and black dashed lines in panel (A), at two different *z*-planes. The legend in panel (D) applies to (C) as well.

By this approach, an effective upper bound on the range of usable resin absorbance values for this process can be identified. We select this bound at a uniformity parameter of 3.5%, at which point the difference between maximum and minimum volumetric absorption coefficients exceeds

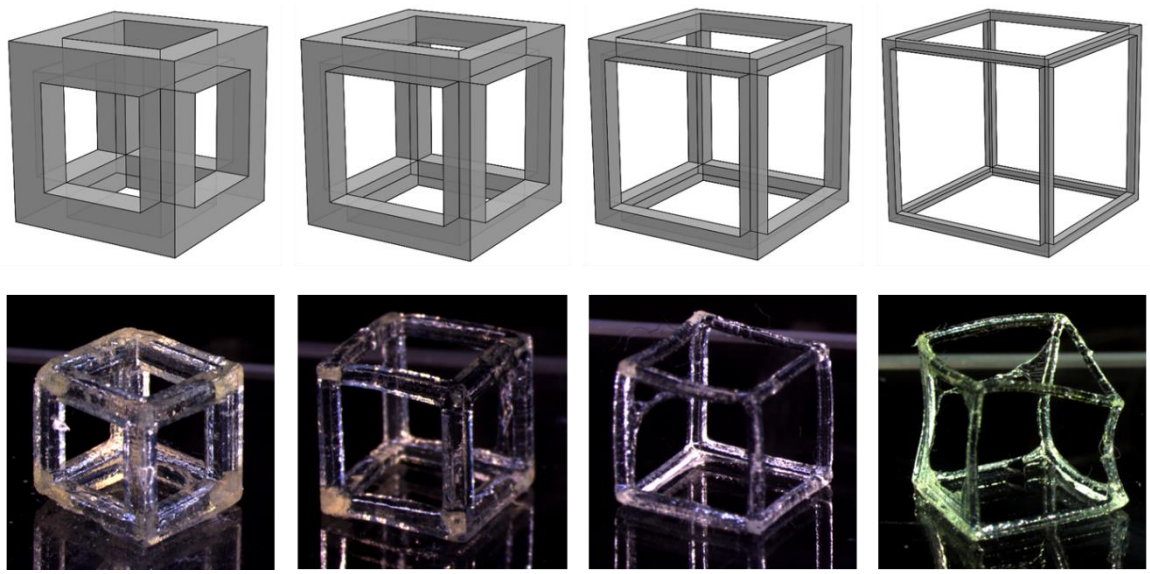

Figure 5.3: Cube structure series used for photopolymerization kinetics study. Top row: CAD models, bottom row: examples fabricated using single-exposures. All cubes are designed to have an outer edge dimension of 6 mm, and strut thicknesses of (L to R) 1.2, 0.9, 0.6 and 0.3 mm. The distortions in the thinner-strut parts are post-fabrication due to handling forces on the very soft polymer.

10% of the mean value, and structures don't completely form from a single exposure. Whereas without compensation, uniformity becomes worse than this threshold at approximately $\alpha = 0.1$ cm^{-1}, the compensation scheme described here extends this to $\alpha = 0.5$ cm^{-1}, significantly widening the usable process window. Figures 5.2C and 5.2D show compensated profiles at these values, with the absorption factor distribution at $\alpha = 0.5$ cm^{-1} being the upper bound of usable uniformity. This is one of the fundamental limitations of the multibeam superposition approach, because absorbance is fundamentally a nonlinear phenomenon, whereas the intensity superposition of multiple beams is linear. As absorbance increases, the spatial nonuniformity of absorbed energy likewise increases, and this nonlinear effect cannot be adequately compensated by linear superposition of intensity profiles.

This result from analyzing the absorption coefficient parameter space can be generalized to different resin container sizes simply by re-scaling to the container size. Thus, whereas the for this container whose size is 1 cm α should be less than 0.5 cm^{-1}, for a 5 cm container, the maximum usable is 0.1 cm^{-1}, and for a 3 mm container, it is 1.67 cm^{-1}.

5.2 Curing Kinetics Study

A detailed study of curing kinetics was carried out using a family of isotropic cube structures as test objects (Figure 5.3). The cubes are 6mm on a side, with strut sizes ranging from 0.3 to 1.2 mm. Fabrication experiments were carried out for photoinitiator concentrations between 0.05% and 0.2% by weight, at a range of laser power settings. This geometry allows measurement of key time-points during the polymerization process as structural features begin to appear in the resin bulk. The first solidification of cube edges (struts - regions of highest intensity with contributions from all three beams) corresponds to the 3-beam curing threshold. This is followed by the appearance of cube faces at the 2-beam threshold. These features are identified when they first become visible in the resin, indicating a refractive index change in the material. The working assumption is that this represents the polymer gel point, at approximately 30% double-bond conversion (see Section 4.3).

The time between the 3-beam and 2-beam thresholds bounds the useful process window for optimizing the 3D structure. Consequently, we noted the time point that resulted in the best fully-formed part (typically just before reaching the 2-beam threshold) which is informally referred to as the "cure time." These are the data presented in Figure 5.4(A). Fully-formed parts were removed from the resin and excess unpolymerized liquid resin was removed by rinsing with a solvent, most often ethanol (less frequently in acetone) for 30 s.

Because the resin's refractive index changes as the material polymerizes, light propagation through the volume becomes distorted. For the structures fabricated so far, the exposure is terminated shortly after the 3-beam threshold is reached, so these distortions don't have a measurable impact on the parts produced. As more repeatable process control is developed, and parts begin to be produced with smaller feature resolution, requiring finer control of exposure times and spatial localization of doses in 3D, the spatial distribution of the illumination will need to be dynamically adjusted as polymerization sets in, to counteract refractive-index-induced distortion to the curing dose distribution.

Ideally, such dynamic compensation can also mitigate nonuniformity in degree of polymerization throughout the cured volume. This nonuniformity is currently an unavoidable result of oxygen re-diffusion into the polymerizing volume, even with well-formed parts. This is most readily observed during rinsing, in situations when nearly- or partially-incorporated material at the surface is unevenly washed away by solvents (this is especially true for more aggressive solvents such as acetone). Additionally, uneven residual stresses in the structure may cause warping, as seen in the thin-strut cubes of Figure 5.3. More fully-polymerized structures may be achieved by post-curing in a photoinitiator-loaded solvent [94]. Further efforts to improve polymerization uniformity will certainly be needed in follow-on work.

Continuing the exposure beyond the 2-beam curing point eventually overcures the build, with single-beam illuminated regions also beginning to polymerize. The cube structure also provides a generic geometry for calculating the necessary lateral compensation in the intersecting beam profiles, and for assessing the spatial uniformity of the target energy dose, based on the relative timing of cube edge appearance.

Our fabrication results indicate that structures can be successfully fabricated using exposures between 1 and 25 seconds and incident laser beam powers, P_B, between 6 and 45 mW for each beam. We find that the resin must absorb a minimum of 200-300 mJ/cm^3 of energy for a part to form, with additional energy required for fine features or low [PI] conditions, as discussed below.

Figure 5.4A summarizes the raw curing data from this study, plotted as a function of I_0, the illuminating beam irradiance entering the cuvette in "bright pixel" areas of the image pattern. I_0 [mW/cm^2] is estimated from two power measurements at the cuvette plane, the beam power P_B [mW] and the background intensity I_{BG} [mW/cm^2], taken by an optical power meter (Thorlabs PM100D with S120C sensor). The areas of the projection where this is measured are shown in Figure 5.4B by the yellow circles for P_B (for each exposure experiment the three beams' power values are averaged) and the green dashed circle for I_{BG}. The calculation for I_0 is then

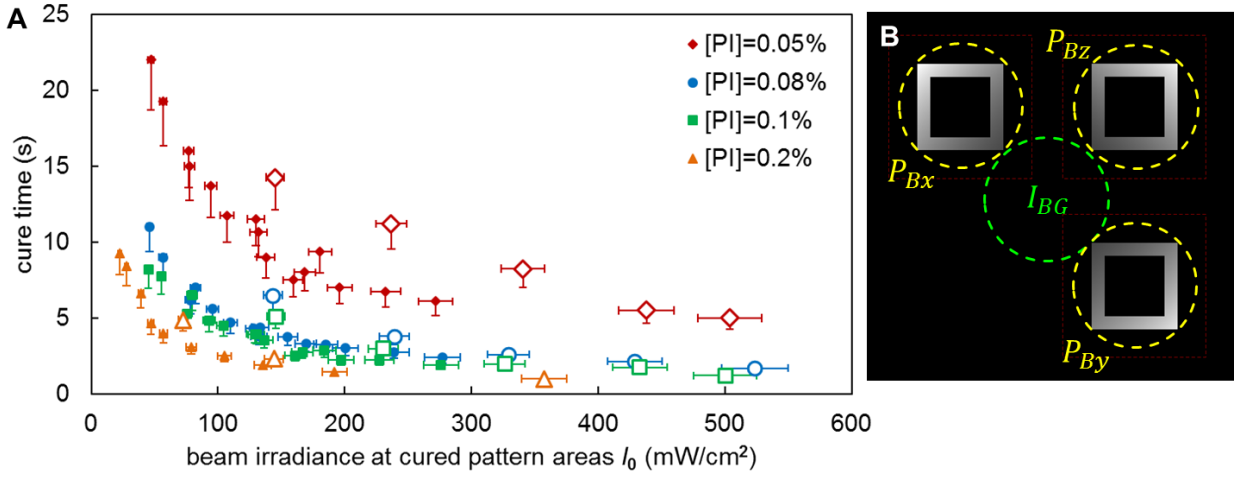

Figure 5.4. Experimentally measured curing times. (A) The times needed to cure good quality parts under various beam intensity condition. Open symbols represent data for the thinnest cube struts (0.3 mm). The main text discusses the significance of their non-alignment with the rest of the data. Vertical error bars are given one-sided due to the tendency of cure time measurements to bias upward owing to gradual photoinitiator degradation. This estimate of the data reproducibility is made as 15% of the measured value, based on N=3 replicate measurements at several representative experimental conditions. Horizontal error bars are given as 5% based on similar considerations. (B) The areas used to measure I_0 values impinging on the resin container.

$$I_0 = \frac{P_B - I_{BG}(A_S - A_P)}{A_P}, \tag{5.3}$$

where A_S is the full area of the power meter sensor, and A_P is the bright pixel area. This calculation assumes that the background illumination I_{BG} (scattering due to diffractive inefficiency) is uniformly distributed over the area immediately adjacent to pattern features. This was verified to be a reasonable approximation when imaging the projected pattern and its background with the process monitoring camera (see Figure 3.1).

From the data in Figure 5.4A, it is evident that the cure times for all 0.3 mm struts (open symbols) are extended in all cases, compared to thicker-strut cure times at identical beam irradiances. This dependence of the curing behavior on feature size is attributed to the 0.3 mm struts being sufficiently thin for oxygen re-diffusion during the exposure, thus extending the time required to cure. When the strut thickness length scale is comparable to the O_2 diffusion length

over the exposure timescale, additional oxygen diffusing in during exposure requires additional energy for the part to cure. For the low-viscosity PEGDA 250 resin used here ($\mu \approx 12$ cP), O_2 diffusivity is estimated to be $D_{O2} \approx 1.5\times10^{-9}$ m^2/s based on diffusivity in similar resins [93,100,103], which corresponds to a diffusion time $\tau_{O2} = x^2/6D_{O2}$ of 2-3 seconds over a length scale of $x \approx$ 100-200 μm. For this reason, we observe a plateau of curing energy doses for struts thicker than approx. 0.4 mm, and an increase in curing times below this size. At the highest irradiances, when cure times drop below 2 seconds, the 0.3 mm struts fall back into line with the rest of the data.

Similar data to Figure 5.4(A) are shown in Figure 5.5, reflecting the 3-beam curing threshold times for the various cubes and resin parameters. However, here the illuminating intensity is recast in terms of $I_{abs} = a_V I_0$, the light power absorbed per unit volume, as defined by Equation 4.13. This is calculated for each structure based on an average estimated value of I_0, as given by Equation 5.3, and an average value of a_V (see Figure 4.2(B) and (C)). This is justifiable, since the resin formulations of this study all have $\alpha \leq 0.2$ cm^{-1}, which therefore means that a_V varies less than 15%, and the intensity compensation for each beam is correspondingly modest.

Reformulated in this way, the cube fabrication experiment results are shown in Figure 5.5(A), excluding the data from the thinnest 0.3 mm struts (open symbols of Fig. 5.4). The volumetric light power density absorption can also be directly converted into a reaction initiation rate, R_{init}, as given by Equation 4.9 (here calculated under an assumption of 100% quantum efficiency, a maximum that is not attained in practice). This parameter is shown as a second x-axis at the top of Figure 5.5(A). In figure 5.5(C), from I_{abs} we derive an estimate of the actual volumetric energy dose delivered to 3-beam regions as

$$E_{CURE} = a_V I_0 t_{CURE} \tag{5.4}$$

where t_{CURE} is the cure time, defined as being equvalent to t_i. This energy dose has a "sharp" threshold that must be exceeded only around the gelation transition, i.e. the minimum energy that

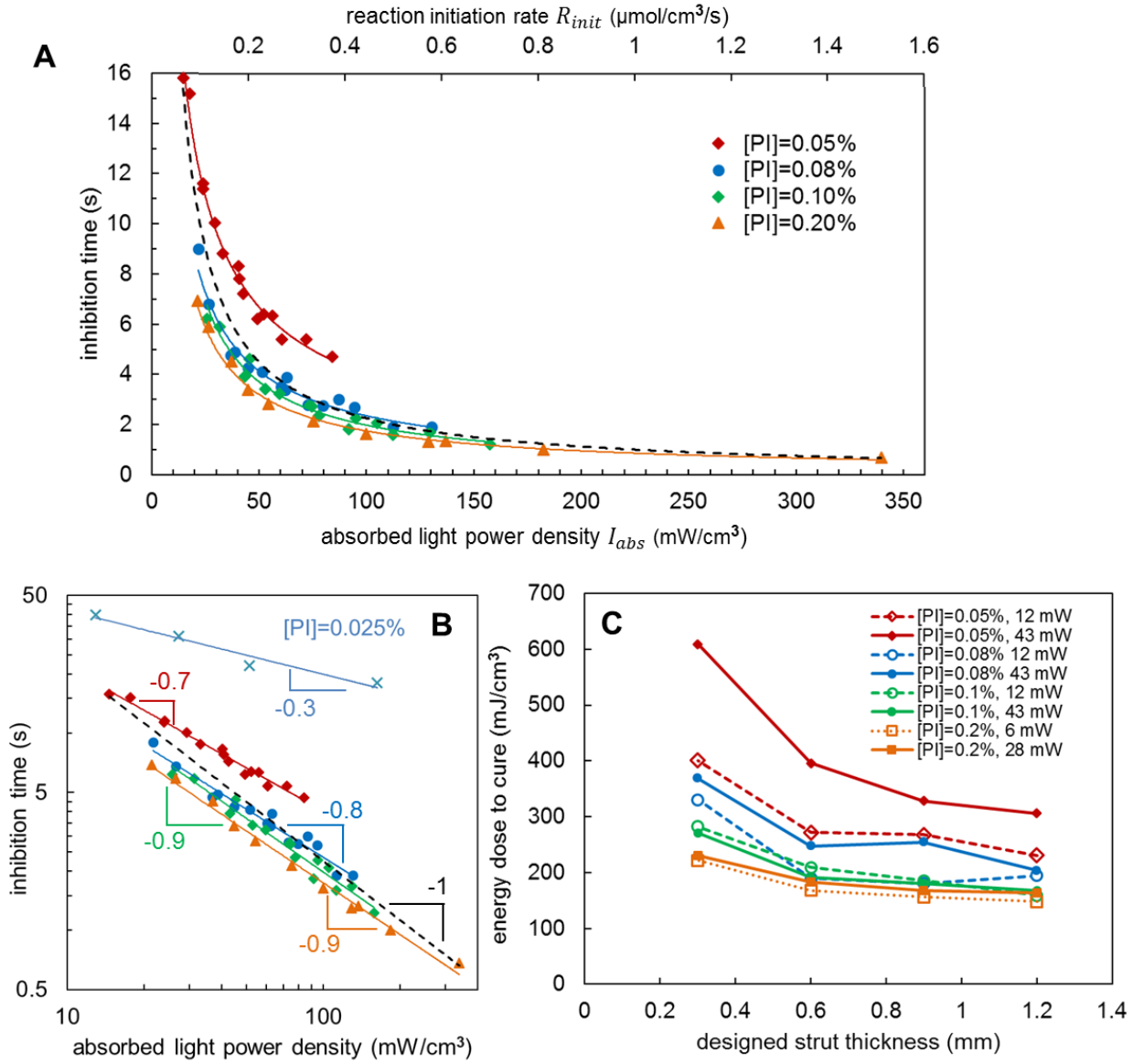

Figure 5.5: Induction time and curing dose dependence on key process parameters. (A) Summary of polymerization induction times prior to initial 3-beam region polymerization, as determined by the first appearance of cube edges. The black dashed line is the equation $t_i = [O_{2,EQ}]/R_i$, where the variables on the right-hand side are estimated from measurements of system parameters or similar resin formulations. This data-set includes strut sizes from 0.6 to 1.2 mm. (B) A log-log representation of the data from panel (A) with an additional set of data for lower $[PI]$ added. (C) Energy doses required to cure cube struts (3-beam superposition regions), plotted for the highest and lowest beam power P_B used at each photoinitiator concentration.

needs to be delivered for a part to hold together (see also Section 4.3). The required additional energy (and its distribution) to cure parts completely remains a topic of ongoing investigation.

The results shown in Figure 5.5 confirm and highlight a number of important features of this process. First, we observe a fabrication regime in which the time for structure formation is nearly completely defined by the resin induction time t_i, as defined in Section 4.1.2, and Equation 4.8. For features 0.6mm and larger, we see the first 3-beam strut features appearing consistent this induction time. When $[PI]$ is in excess relative to $\left[O_{2,EQ}\right]$ (estimated here as $\approx 1.2\times10^{-3}$ M, from descriptions of similar low-viscosity multifunctional acrylate monomers in the literature [90,93]) R_{init} remains approximately constant throughout the induction period and the inverse relationship between t_i and R_{init} is unmodified.

However, when $[PI]$ is approximately equal to $\left[O_{2,EQ}\right]$ (in absolute molar terms), by the time that dissolved O_2 has been depleted, little to no PI remains available for polymerization to proceed. This means that $[PI]$ and therefore R_{init} both become time-varying, decreasing with time, and induction times are significantly extended. We see this in Fig 5.5A for the resin with 0.05% $[PI]$ (which is $\approx 1.6\times10^{-3}$ M), approximately matching $\left[O_{2,EQ}\right] \approx 1.2$ mM. Below this threshold, curing times are extended many-fold, or even indefinitely such that complete structures do not form, even when light energy continues being delivered to the resin. This is seen in Figure 5.5B, where induction times for $[PI] = 0.025\%$ are added, continuing the trend of the data from $[PI] = 0.05\%$ of increasing curing times. The log-log view of these results in Figure 5.5B reveals the additional feature that decreasing $[PI]$ leads to a decreased slope in the power-law fit. Decker and Jenkins [90] suggest that chain peroxidation reactions during O_2 scavenging (when one PI radical consumes more than one O_2 molecule) may be associated with reduced slope, and become more pronounced at low illumination intensities when the initiation rate is low. Here, the low initiation rate is a consequence of low $[PI]$, so whether chain peroxidation is the mechanism responsible for this behavior is a hypothesis that remains to be investigated.

Figure 5.5C provides another perspective on the size-dependence of the energy required to cure. There is a clear increase in curing energy for the smallest strut size at all intensity conditions. When $[PI]$ is sufficiently higher than $\left[O_{2,EQ}\right]$, only a weak dependence of the curing energy on the beam power, P_B, is observed, whereas as $[PI]$ is lowered closer to $\left[O_{2,EQ}\right]$, a strong

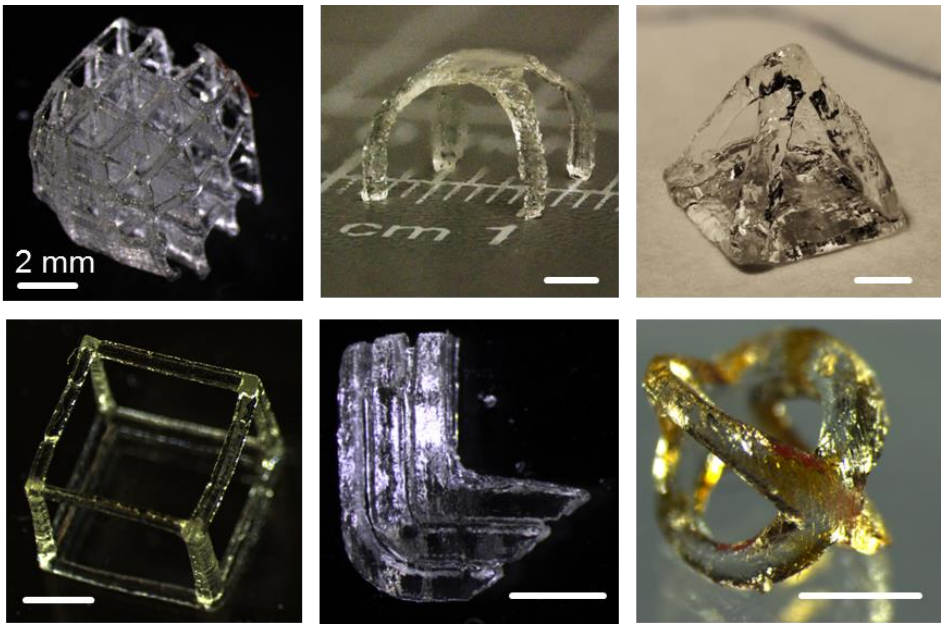

Figure 5.6: Example structures fabricated by the volumetric 3-beam superposition technique. All structures shown were fabricated by a single exposure, between 5 and 10 s duration. Scale bars are 2mm.

dependence on P_B emerges, with higher intensity counterintuitively requiring longer cure times. The working hypothesis, as yet unverified, is that this arises because at higher beam power, all of the PI is depleted more quickly, as O_2 scavenges it, and longer wait times are required for any additional PI to re-diffuse into the polymerization zone, while energy continues being delivered to the resin.

5.3 Fabrication Results and Discussion

Figure 5.6 shows a representative variety of geometries that can be fabricated by this method, including beams, planes, and struts at arbitrary angles, lattices, and symmetric and asymmetric geometries. Significantly, no constraints exist on span, bridge, and cantilever elements, and curves may be produced without layering artifacts, which are all major challenges with standard AM layer-by-layer approaches. The prototype system designed during this research effort has to-date been used to fabricate several hundred individual parts/objects. No supporting substrate is required during a build (though one can be used, when desired). The ability to fabricate in the

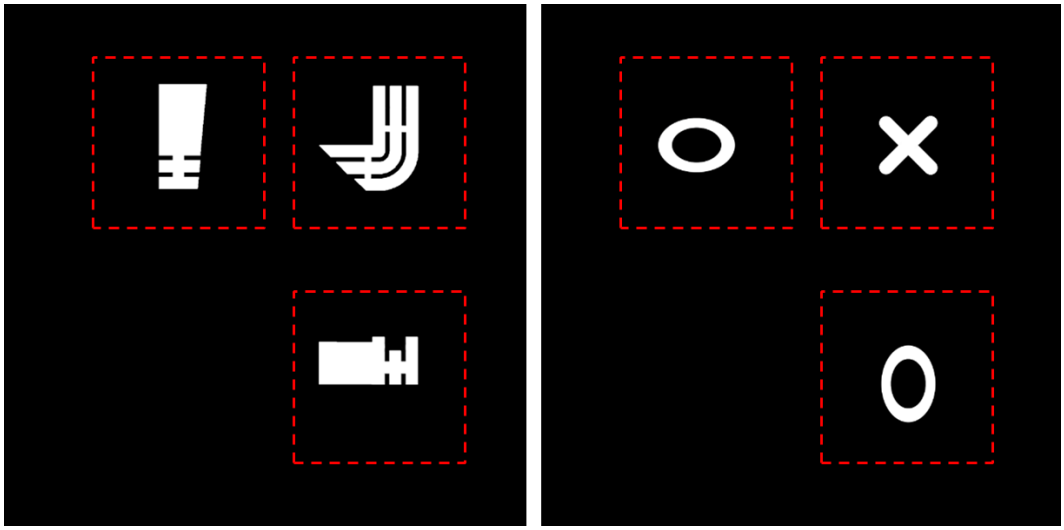

Figure 5.7: Dissimilar profiles in each of the superimposed beams. The set of patterns at left is used to produce an LLNL logo structure similar to the center panel of the bottom row of Figure 5.6, and the patterns at right result in the crossed-rings structure of the lower right-most panel. As in Figure 5.1 the red dashed boundaries indicate the boundaries of the 10 mm cube build volume, relative to the projected patterns.

resin bulk, with no supporting material required, and without substrate present is a unique feature of this approach which can be advantageous in many contexts.

One such application is the fabrication of structures from very soft materials such as hydrogels, which can be produced wholly *in situ.* Made by other means, these would not be self-supporting, or would be damaged or destroyed by shear forces arising from fluid motion or interlayer residual strains. Indeed, some structures with fine features fabricated in the present work were extremely soft (see, for instance, Figure 5.3). Generally, however, the aim is to produce parts made of fully-cured hard polymer; this was not the case for many structures, which exhibited qualitative evidence of being only partially cured. This is not surprising, given that exposures were often stopped just past the gelation point (see also Sections 4.3 and 5.2). However, complete characterization of the mechanical properties of fabricated structures in relation to the exposure parameters was outside the scope of the present work. Exploring such mechanical properties in conjunction with the polymer DOC (or as double-bond conversion fraction) is an important direction for further investigation.

It is worth noting that the surface roughness of the parts seen in Figure 5.6 arises from speckle noise present in holographically-projected images (see Section 2.4.2), and not from layering. This roughness is on the scale of ~100 μm in the currently-configured system, but may be made smaller or larger, depending on the beam delivery optics. Re-diffusion of inhibitory oxygen helps to smooth out rough surface effects, and the development/rinsing conditions have a strong effect on surface roughness (e.g. acetone rinsing produces significantly rougher parts). Only qualitative observations have been collected about this aspect of the process at this point.

As first suggested in the discussion of laser coherence and power in Section 3.2.2.1, it is worth assessing the minimal source power necessary for the volumetric fabrication process to work. The single-mode 405 nm laser with maximum output of 45 mW, after phase-shaping by the CGH yields approximately 1 mW per beam at the resin container, corresponding to 1-10 mW/cm^2 in image pattern areas. Referencing the design space of Figure 4.3, a PEGDA resin was formulated with the initiator Irgacure 819, which absorbs strongly at 405 nm, with an approximate extinction coefficient $\varepsilon_{405} = 500$ L/mol/cm. Mixed at 1.5 mM, just above the equilibrium O_2 concentration, this initiator gives an absorption coefficient of $\alpha = 0.77$ cm^{-1}, somewhat beyond the upper limit identified in Section 5.1.1 and Figure 5.2. Indeed, structures begin to form in three-beam regions after induction times near 10 s, but producing uniform parts is challenging, as expected.

5.4 Limitations and Challenges for Volumetric Multibeam Superposition

The key limitation to the volumetric approach explored here arises from the prismatic nature of the illuminating beams – as each beam does not vary along its axial direction, the task of patterning along that dimension falls on the other two beams. Although the geometries that can be fabricated are complex, they are not fully arbitrary. For instance, it is not possible to generate a solid sphere or a spherical shell.

These limitations arise partially from the specific system configuration used during this work, in which the depth of focus of the illuminating beams is larger than the resin container size. A configuration using a shorter depth of focus would axially constrain the region of 3-beam

maximum curing dose for each beam, and this could slightly improve upon the constraints due to the prismatic beams, but this only partly mitigates that fundamental limitation.

More progress can be made by using multiple dissimilar exposures within the same volume to assemble sub-volumes into the required complex shape. For instance, an octet truss lattice unit cell [9] can be made by first exposing the inner octahedron, then exposing the surrounding tetrahedra, possibly in multiple steps. In such cases, the timing between exposures must be carefully controlled relative to the diffusion of O_2, to prevent unwanted polymerization in single- or two-beam region of a later exposure that overlaps with a single- or two-beam region of an earlier exposure. This will also be true for any structure that is to be created by tiling adjacent volumetric subunits together.

We have already discussed in Chapter 5 the necessity of assuring a uniform absorbed energy dose through the cure volume, and the resulting process constraints required by the multibeam superposition method. An additional consequence of this is the varying degree of monomer conversion (DOC) that results throughout the part. Furthermore, because significant oxygen is consumed during the polymerization, using a large fraction of initiator molecules, and being incorporated into the polymer matrix as peroxy radicals becoming peroxide chains, this negatively impacts the long-term chemical stability and mechanical properties of the resulting polymer. These are key challenges to overcome for the technology going forward that will need to be addressed, both to achieve the necessary uniformity for reliably and correctly generating desired geometric features, as well as to ensure good mechanical properties of the final structure. Post-curing in solvent with photoinitiator is one approach to this issue [94], but further investigation in this area will surely be required.

As a final consideration, the fundamental physico-chemical basis of this fabrication paradigm requires a nearly-transparent fabrication material which exhibits oxygen-inhibition effects. Therefore, generalizing this approach beyond the set of photopolymers with these two properties will prove challenging (even by loading these polymers with particulate nanomaterials, as is often done with polymer resins to expand their functionality).

Chapter 6
Conclusions and Outlook

The results of Chapter 5 demonstrate unambiguously that the multibeam volumetric fabrication method is a viable approach to creating aperiodic 3D structures as unit operations of an additive manufacturing platform. Referring to the Research Goals laid out in Section 1.2.2, the feasibility question regarding this paradigm has been answered in the affirmative, having here conceptualized, designed, built and tested a fully functioning holographically-driven volume-at-once 3D fabrication system prototype. This approach does indeed allow very fast fabrication of 3D geometries in seconds, without layering or support material. Though the prismatic shape of the overlapped beams presents some limitations to full geometric generality, the available geometries nevertheless span a wide range of possible structures than traditional multi-beam or interference-based lithography. The major constraint for using this method is for the build volume to be mostly transparent, and minimally absorptive, for now being limited to polymer materials. Attaining uniform and complete curing of the fabricated part is another challenge that must be overcome, though this also crops up in other photopolymer-based systems.

Lastly, we have found the use of dynamic digital holography as the operating principle for this approach not to be strictly necessary. The system complexity imposed by holography does not bring sufficient benefit without significant further advances in pixelated SLM technology. Fortunately, the overall volumetric fabrication approach remains viable and powerful with non-holographic illumination. We are now in a position to evaluate its performance, consider the consequences of design choices, and formulate the next set of design modifications. Here, we benchmark its capabilities in comparison to other polymer-based fabrication methods, and review the specific advantages and drawbacks of the overall multibeam superposition approach. Finally, we suggest some directions for fruitful follow-on investigations.

6.1 System Performance Metrics

There are a wide variety of ways to evaluate the performance of an AM platform. Standards and test objects for AM fabrication methods are only beginning to emerge [104,105], and largely emphasize pattern dimensional fidelity and the mechanical properties of deposited materials. Because the volume-at-once method is in its infancy, more development and optimization will need to take place before this technology space has matured sufficiently for evaluation based on such standards.

Instead, we consider a range of *ad hoc* system performance standards, suitable for placing this technology within the context of other AM methods, focusing mainly on polymer-based processes, both commercially-available and those reported in the research literature. This includes assessing build speed, minimum feature resolution, maximum build volume and part size, and a measure of complexity or information density available to the process. The semi-quantitative comparisons below are an initial assessment based on current fabrication results, and reasonably-expected expanded capabilities with little additional development. More rigorous studies of each aspect will more clearly illuminate the ultimate performance limits of the volumetric approach.

6.1.1 Fabrication Speed

When comparing this volumetric fabrication method to layer-by-layer or point-by-point methods in terms of speed, two metrics that can be considered: voxels cured per unit time, and volumetric material deposition rate.

6.1.1.1 Voxel rate

For a 0D voxel-based system, the highest voxel rate is attained by galvanometer-scanned direct laser writing (DLW) systems. Those commercially sold by Nanoscribe, GmbH (Karlsruhe, Germany) write diffraction-limited voxels approximately 100-200 nm in width at speeds up to 10 mm/s, which corresponds to ~10^4-10^5 voxels/s. A 2D layer-at-once platform such as projection micro-stereolithography has a voxel rate defined by the pixel count of the projection device

within a layer build-time. The highest-resolution systems use HD resolution (1920×1080) images [20] and exposures of ~10 seconds, yielding ~10^5 voxels/s, though many implementations of layer-at once are slower by a factor of 10 or more. The volumetric multibeam system, at a conservative estimate, can be considered to have a 100 µm cubic voxel (see the section on Feature Resolution below), with exposures as fast as 1 s, so parts fitting within a 7-8mm cube quickly exceed 10^5 voxels/s, approaching 10^6 voxels/s.

Of course, being a volumetric method, rather than voxel-by-voxel, the comparison is only somewhat valid. Moreover, scaling the side length of the build volume up 2-fold, or scaling the minimum feature dimension down 2-fold is readily within reach, so the voxel rate can increase nearly an order of magnitude before any physical limits need be considered. Thus, when measured by voxel rate, our volumetric approach is competitive with and poised to surpass some of the highest-speed commercial and advanced-stage research AM systems.

6.1.1.2 Material deposition rate

In terms of volumetric deposition rate, the fabrication results from the prior chapter suggest that the entire addressable fabrication volume may be polymerized within the timescales as the tested exposure lengths (1-20 s). This is a cubic volume about 0.9 mm on a side (0.73 cm^3) curing in one second, as currently configured, corresponding to a volumetric rate of 2.5×10^5 mm^3/hr. This is comparable to the layer-at once continuous-interface liquid production (CLIP) method [22], and also comparable to the maximum build of the highest-throughput commercial SLA and SLS platforms, which claim speeds that translate to 10^5-10^6 mm^3/hr deposition rates. With our volumetric system, using a larger resin container, the build rate may be limited by heat evolution during polymerization, so perhaps a more realistic estimate is to assume a volumetric fill factor of 0.1-0.3, reducing the rate 3- to 10-fold. However, as discussed in the next section, scaling the volumetric multibeam approach by using a larger container is expected to overcome this rate reduction.

6.1.2 Feature Resolution and Accuracy

The feature resolution of the volumetric method is currently estimated to be 100 μm, as seen in Figure 5.6 where the smallest features are on this size scale. Many parts with elements of this size were too soft to successfully remove from the liquid. This arises mainly due to the structures being highly compliant due to low degree of cure (DOC), especially with small struts and features. Unlike micro-scale layer-based stereolithography methods [20,22,106], in which an absorber species is incorporated into the resin (which does not participate in the polymerization reaction, but only limits the light penetration depth) to control the spatial extent of polymerization, absorbers can't be used in our volumetric approach, since maximum resin transparency is required to achieve uniform polymerization with the structure.

From studying the photochemical process, it's clear that the ability to accurately reproduce smaller features will be determined by the resin parameters that govern polymerization kinetics, rather than optical system performance. It will be critical to properly balance O_2 diffusion (as the fastest-diffusing species) against the reaction initiation rate, R_{init}, thereby defining the DOC throughout a given geometry. Relatedly, because diffusing O_2 is such a key participant in this dynamic picture, feature density plays just as important a role as feature size. Closely-spaced fine-scale features cure faster than those sparsely-placed. These dynamic non-equilibrium processes cannot be tractably predicted without using finite-element computational approaches, so a thorough treatment is beyond the scope of our discussion here.

However, a limited investigation was carried out using computational modeling in COMSOL, in collaboration with Todd Weisgraber at Lawrence Livermore National Laboratory. A reaction-diffusion model was implemented, based on the framework described by Bowman and co-workers [93,100]. The kinetic parameters were adapted from those used for polymerization reactions with a 1,6-Hexanediol diacrylate (HDDA) resin, and tuned to match the experimental measurements reported in Chapter 5. The initial results suggest that resolution at least down to 25 μm may be successfully achieved, though with increasing distortion and size inaccuracy as feature size decreases. The model predicts that reducing the equilibrium dissolved oxygen

concentration $[O_{2,\mathrm{EQ}}]$ will improves feature accuracy and reduce distortion more effectively than increasing illumination power. These results are being more fully explored and are in preparation for publication. Additional parameters like increasing resin viscosity and more deliberate tailoring of the molar extinction coefficient remain to be investigated.

The optical resolution of this system also has an impact on the ultimate feature resolution, but it is of secondary importance to resin effects. As mentioned in Section 2.3.2, the resolution at the HP from SLM diffraction is 8.7 and 15.3 μm for the horizontal and vertical directions, respectively, which is currently scaled 2× by the magnifying optics, resulting in a source-image pixel at the build volume corresponds to 17.7 μm. This minimal spacing can be scaled larger or smaller, as the overall projected image is scaled to match the resin container, but optical resolution is not expected to limit the system performance until resin performance is improved.

To compare the speed and resolution metrics of our new technology to the state of the art, the volumetric deposition rate and minimum feature size for a range of existing polymer-based AM methods were analyzed. These are shown in Figure 6.1. Resolution is rendered as spatial frequency, ξ, so that better performance gives higher numbers (in units of mm^{-1} or line-pairs per mm similarly to optical resolution figures). Spatial frequency is defined as $\xi = 1000/2\Delta x$ where Δx is the minimum line-width given in microns. A table containing the data used to produce this plot may be found in Appendix A.

We see that the volumetric approach is comparable in its performance to some of the highest-speed commercial SLA and SLS platforms.

6.1.3 Build Volume and Part Size

As currently configured, maximum part size and build volume are essentially the same, and are limited by the internal volume of the spectrophotometer cuvette, which is approximately 1 cm^3. Similarly to many other AM approaches, overall part size (and fabrication speed) must be traded off against resolution and minimum feature size. When scaling part size up by using a larger container, the volume of resin addressable by beam-folding a single projected image becomes

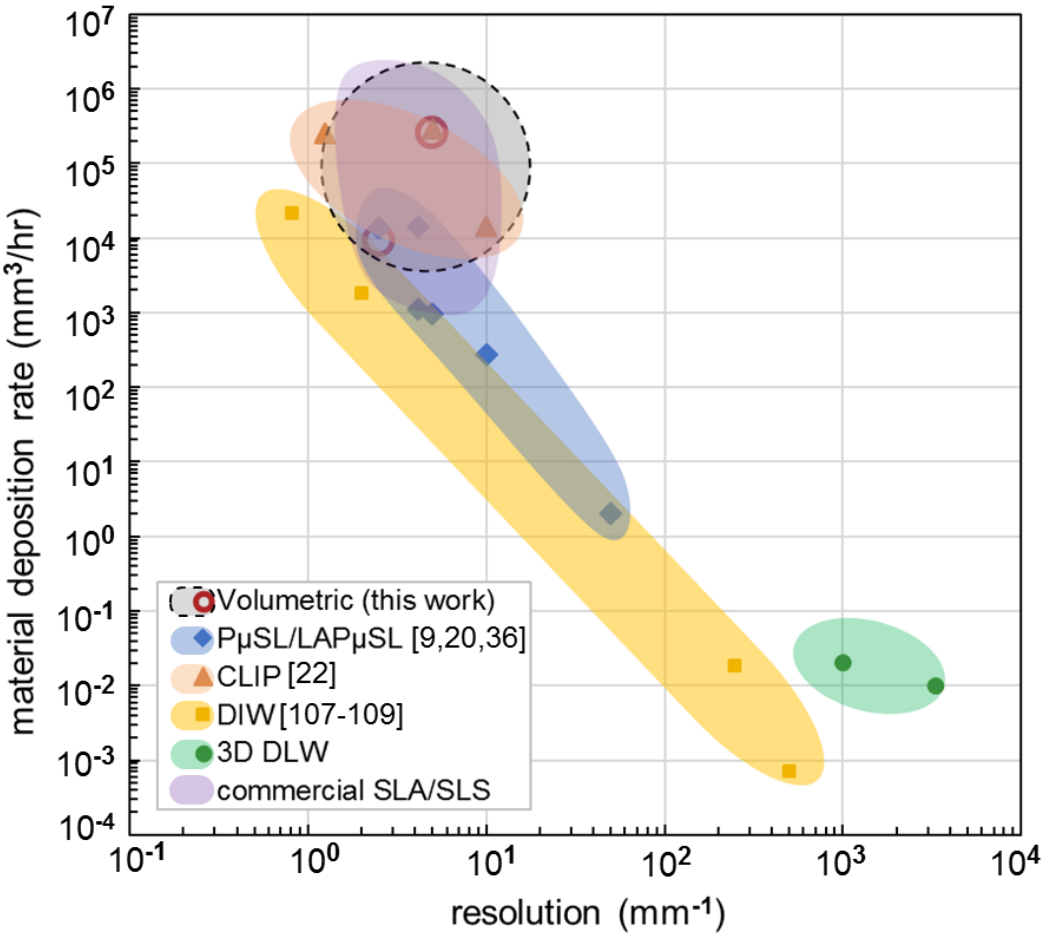

Figure 6.1: A process performance comparison of volumetric fabrication to other polymer-based AM methods. The gray dashed-boundary oval encloses fabrication results from two scenarios, and represents an assessment of the near-term potential of the volumetric fabrication method reported in this work. Plotted data points represent specific published results, or system operating parameters known to the authors first-hand. PμSL/LAPμSL refers to projection micro-stereolithography and its large-area variant. [9,20,36]. SLA refers to stereolithography, and SLS to selective laser sintering. Commercial system performance is based on manufacturer specifications.

limited by the field of view of the final image-relay optics. For instance, instead of a 2× magnification, increasing the final projection to 5× would increase the maximum single-image accessible volume by 15-fold, while decreasing the incident illumination intensity 6.25-fold (this is the factor by which the projection area is increased). The necessary light intensity would require increasing the laser head power setting to approximately 2.9 W (to give 11.5 mW/cm^2 per beam at the build volume), which is available in our system, given the 6W maximum power

from the 532 nm DPSS source used here. However, this would be just at the threshold of maximum intensity that the phase-only SLM can handle without damage, so this cubic volume ~2.5 cm on a side likely represents the maximum that this holographically-driven system can attain for single-exposure full-volume structures if other subsystems are left unmodified.

A more robust and flexible way to scale the build volume for much larger parts is to use independent sources and SLMs (or other pattern-projection devices) to produce each of the beams for superposition. For instance, using three LED-driven amplitude-modulated SLMs similar to those found in the large-area projection microstereolithography (LAPμSL) platform [36] should easily allow scale-up to a build volume of at least 10×10×10 cm. This volume is unlikely to be addressable by a single exposure, due to available light intensity, and would entail tiled exposures of adjacent sub-volume elements. This is most readily accomplished by scanning galvanometric mirrors, akin to the way the LAPμSL system tiles 2D images to assemble larger 2D image layers. In this situation, movement of cured sub-volumes must be prevented while new sub-volumes are being added. This can be realized either by incorporating substrate surfaces or struts on which early sub-volumes are cured, or the viscosity of the resin must be raised to ensure no movement on the timescale between exposures.

The final consideration for build volume scale-up is the resin absorbance, which, as described in Chapters 4 and 5 has significant implications for uniformity of polymerization rate, and sets practical upper limits on photoinitiator loading. The simplest way to analyze this is to require that the absorbance through the full depth of the build volume remain less than 0.5—as we have seen, this allows the mutual beam compensation algorithm to produce a reasonably uniform distribution of absorption coefficients. This corresponds to a value of $\alpha \approx 0.3$ cm^{-1} for the 1 cm cuvette, and $\alpha \approx 0.03$ cm^{-1} for the 10 cm on a side volume considered for scale-up. The generalized resin parameter space mapping in Figure 4.3 provides a means to estimate the source intensities required to attain reasonable curing time with resins of various formulations. From it, we can estimate that to ensure this low volumetric absorption factor (while maintaining a high enough $[PI]$ level to avoid operating too close to $[O_{2,EQ}]$), a photoinitiator with $\varepsilon =$ 5-10 M^{-1}cm^{-1}

must be used. Then, a source irradiance of 100 mW/cm^2 or more at the build volume will allow for exposures of ~10 s or less.

Ultimately, based on these considerations, the maximum build size of this fabrication paradigm will be limited by the following, in approximate order from most to least constraining: (1) the maximum size of an available container with optical-quality walls, (2) the total available light power, (3) the availability of low-absorbing initiators at the necessary wavelength, and finally, (4) the rate of heat evolution from curing polymer.

6.1.4 Part Complexity – Information Density

The concept of part "complexity," can be considered as a combined metric that brings together resolution and maximum part size. A conceptually related view is to describe this as the process information density—that is, the number of independently-controlled volume elements (voxels – acting as informational units similar to digital bits) that can be produced within a certain part volume. As a notional test geometry, we can consider "cured" and "uncured" minimum-size voxels arrayed as a 2D or 3D checkerboard pattern within the build volume. We can then ask whether every one of those "bits" can be independently turned "on" and "off" and how the technology performs as far as the ratio of maximum part size relative to the minimal voxel size.

With volumetric multibeam fabrication, due to the prismatic ("extruded" pattern) beam geometry, not every voxel within the full build volume is independently controllable, so the 2D pixel count of each beam must be summed, rather than multiplied. In the present configuration, with each beam having minimum features of 100 μm over an area of 10×10 mm, each contains 100×100 "information pixels" yielding 3×10^4 controllable voxels in a single exposure. Following the arguments in the previous sections regarding scaling of single-exposure features (down to 25 μm) and part-size (up to 25 mm on a side), this is 1 Mpx per beam pattern, so the overall volume will attain 3×10^6 controllable voxels. Beyond this, we will approach the maximum number of controllable points within an image being limited by an SLM's total pixel count, i.e. the SBWP.

This compares extremely favorably with multibeam interference lithography. Here, though the photonic lattices exhibit finely-resolved submicron structure, the voxels are not independently controlled; rather, the number of beams, beam size and coherence length, and phase relationship between them define the information density. By a very rough qualitative estimate, compared with the values above, the build complexity here is only ~10^1-10^3, depending on any patterning within the interfering beams.

Comparing to other polymer-based AM technologies, for many examples the ratio of maximum linear part dimension to minimum feature size is ~10^2–10^3. Typically, all minimum-size voxels can be patterned in all 3 dimensions, giving single-build complexity factors (without tiling) somewhere between 10^6 and 10^9. However, as discussed in Section 6.1.1.1 above, since voxel rates are typically ~10^5 voxels/s, build times for such complex parts can quickly exceed many hours.

We conclude that the 3D volumetric multibeam superposition approach, though early in development, is comparable on many performance metrics to existing polymer-based fabrication methods, and is primed to quickly exceed them with additional optimization. Based on the foregoing discussion, it is expected that the most likely path toward a commercially-viable platform rooted in this technology may be found by using larger resin containers and multiple independent amplitude-modulated beam pattern sources.

6.2 Holography as a Basis for 3D Volumetric Fabrication

One of the key questions posed at the outset of this dissertation work concerned the feasibility and utility of using holographic light shaping for 3D volume-at-once fabrication. The feasibility of this approach has been demonstrated, but in a way that was perhaps not initially expected. This work demonstrated volume-at-once structures being built by using optical *amplitude* superposition. This was accomplished here by means of *phase-controlled* shaping of the optical field, hence the use of diffractive holographic techniques. However, so far no compelling reason

has been found to conclude that ordinary image-relaying and amplitude-modulating optics cannot be used to accomplish the same results.

Holographic phase-controlled pattern projection does bring with it two key advantages. The first is the approximately constant total power directed into the build volume by the phase-only SLM, regardless of the target intensity distribution. This means that the total source beam power impinging on the SLM is redistributed over the projected intensity patterns. This is an efficiency benefit, as dark image areas don't simply mean that light is "thrown away," but this efficiency must be measured in the context of the overall lower efficiency of the SLM as a diffractive optical element.

The second advantage of phase-controlled intensity pattern generation is the capability for dynamic transverse scanning and axial re-focusing by adding grating and lens phase to the calculated holograms. Without phase-controlled optics such effects must be accomplished by mechanical components such as scanning mirrors or adjustable lens assemblies. It is possible to take advantage of these translations of the projected pattern in 3D space, for instance to tile multiple complex sub-volumes into a larger complex part with multiple exposures, with no changes to the optical configuration. Likewise, in a configuration where the relative path lengths of the superposed beams differ from each other enough to require focus adjustment, and especially if this must happen dynamically during a build (when tiling sub-volumes) the holographic approach has significant advantages over optomechanical components for accomplishing the same.

Nevertheless, diffractive beam shaping by holography carries with it a set of drawbacks whose collective impact is enough to outweigh the benefits given above in most situation. The most general of these is the increased complexity and cost of a holographic system, since phase-only SLMs are more expensive than amplitude-modulating ones, and a laser source with sufficient coherence to allow holography is typically more expensive than a source with lower coherence. Moreover, the coherence of holographic-quality lasers means significant speckle noise is intrinsic to such systems. Speckle must be handled in some fashion, and even when it is, it

reduces the part quality (see Sections 2.4.2 and 5.3). Most importantly, the requirement to calculate the CGH phase patterns for image projection imposes a significantly larger computational burden on holographic systems (in our implementation that uses multi-CGH averaging to overcome speckle noise, this computational burden is even greater).

Therefore, the conclusion must be made that holographic optical field shaping imposes too great a cost in additional resources to be worthwhile, using pixelated phase-only SLM technology. It may become worthwhile if additional capabilities requiring holography were incorporated. For instance, independent control over both the phase and amplitude of the beams in the volume-at-once context would allow imposing a prescribed phase relationship between the overlapping beams, thus combining our volumetric multibeam paradigm with multibeam interference lithography. This can provide μm-to-mm scale features with submicron photonic crystal-like microarchitecture. Independent phase and amplitude control, however, is highly challenging to achieve in practice, and requires at least separate SLMs for phase and amplitude.

In addition, if phase-only SLM technology advances far enough to bring the pixel pitch into the size scale of the light wavelength, the limitations on single-beam 3D pattern shaping deriving from small diffraction angles and numerical apertures would be significantly improved (also eliminating loss of light energy into higher-order diffractive modes). Here, holographic patterning by single-beam diffraction from an SLM may become a means to generate arbitrary 3D patterns in space for polymer-based fabrication.

6.3 Future Work

With the basic framework of volumetric multibeam superposition fabrication formulated, a number of useful directions can be pursued, some of which have been alluded to in earlier sections of this dissertation. This section collects them together and highlights the most promising directions to improve the versatility, reliability and quality of this method.

6.3.1 Resin Properties

The most fruitful path toward improving process control and part fidelity is to gain a deeper and finer understanding of the full set of resin parameters. These can be explored in computational simulation, by extending the initial model described in Section 6.1.2 above, coupled with experimental validation of the important effects.

6.3.1.1 Viscosity

As discussed in Section 4.4, resin viscosity plays two key roles in the volumetric curing process, affecting the diffusivity of resin components, and buoyant effects due to density changes and convection. Raising the mixture viscosity is expected to slow down the action of these buoyant and convective forces acting during the polymerization. With little exception, the cross-linked polymer is slightly denser than the liquid resin, so parts sink after they polymerize, which works against the upward motion due to heating during polymerization. Avoiding this complex interplay altogether is preferable to carefully measuring and controlling it. Possible acrylate additives that will raise the overall viscosity, and compatible with the free-radical initiated chemistry used here, include bisphenol-A glycerolate diacrylate (BPA-DA, viscosity 2000-4000 mPa-s) or pentaerythritol triacrylate (PETA, viscosity 600-1000 mPa-s), and many specialty resins from manufacturers such as Rahn AG. Ultimately, these efforts are anticipated to provide better access to the smallest feature scales.

6.3.1.2 Oxygen Control

Since O_2 inhibition plays such a vital role in this process, gaining more control over its behavior can pay significant dividends. Though O_2 is necessary to help define the spatial extent of the polymerization, the amount of O_2 dissolved in acrylates in equilibrium with room air is likely higher than optimal for this process. It may be expected that reducing the O_2 dissolved in the liquid at the start of an exposure by approximately 10-100-fold will yield significant benefits in curing speed, uniformity, and feature resolution, with much less of the initial photon flux is used up to deplete the inhibiting O_2.

This may be accomplished by enclosing the build vessel in an oxygen-controlled environmental chamber. Also, chemical additives have been demonstrated [91] which scavenge oxygen, reducing the initiator primary radicals needed to deplete it. Alternatively, it is worthwhile to investigate polymers that have lower O_2 solubility than the typical acrylates, reducing the oxygen present without additional control.

6.3.1.3 Direct Measurement of Kinetic Parameters

So far, the resin photochemical kinetics have been sufficiently well-described by using kinetic constants and material properties from similar acrylate monomers. Measuring the actual parameters of the relevant resin formulation in use will, of course, create higher fidelity in modeling process conditions and improve the predictive power of computational efforts. This is accessible by using real-time FTIR or Raman spectroscopic methods to monitor the chemical conversion of monomer to polymer with the relevant initiators under controlled illumination and environmental conditions.

6.3.2 Process Monitoring

As is the case for any AM process, real-time monitoring is highly beneficial for improving understanding of the process dynamics, and gaining further control of process parameters. One possibility is to use machine vision to precisely detect the point at which structural features appear, and the time-dependent curing behavior. This may be made more sophisticated by Schlieren imaging to increase the sensitivity of the measurement to changes in refractive index. This information may then be fed back to a control algorithm to adjust the illuminating beam power, ultimately finely tuning the polymerization rate to avoid deleterious effects like excessive heating. Adding *in situ* temperature measurements of the polymerizing material during the reaction, or similar *in situ* measurements of $[O_2]$ by micro-scale dissolved oxygen probes will provide additional dimensions of process information, and in the long run may become standard parameters that should be monitored at all times for robustness of the build.

6.3.3 Geometric Versatility

One final important direction for further investigation is a more detailed exploration of the ultimate limits of geometries that may be build using multibeam superposition. This will likely require collaboration with experts in topology, to mathematically define the geometrical space that can be described by prismatic geometries. This will likely yield more general algorithms for beam pattern generation directly from 3D CAD data. It is envisioned the outcome may be something like a decomposition into a limited set of basis functions, linear combinations of which can fully span the geometries available to our process.

Appendix A

Source Data Table for Speed/Resolution Comparison Plot (Fig. 6.1)

Tech-nology class	System Description	Min. feature size (μm)	Volume build rate (mm^3/hr)	Notes	Reference or Data Source
3D Volu-metric	LLNL / MIT prototype (this work)	200	9000	Typical part: 0.5 cm^3/20 sec	Direct experience with system
		100	252000	Max. volume / min. exposure of current config.: 0.7 cm^3/sec	
2PP DLW	Nanoscribe	0.15	0.01	Using 63X objective	Direct experience with system
		0.5	0.02	Using 25X objective	
Projec-tion Stereo-litho-graphy	PμSL	10	2	1x2 mm x 1 mm/hr	[9,20]
	LAPμSL	50	270		[36] and personal correspondence with system designer
	LaPμSL	100	960		
	LAPμSL	120	1093		
	LAPμSL II	200	13670		
	LAPμSL II	120	13853		
CLIP	Carbon3D	400	250000	Shoe: 100x25 mm x 100 mm/hr	[22]
		100	288000	Argyle: 24x24 mm x 500 mm/hr	[22]
		50	14400	Paddles: 24x24 mm x 25 mm/hr	[22]
DIW	J. Lewis @ UIUC	1	0.000707	1 μm filaments at 250 μm/s	[107]
	J. Lewis @ UIUC	2	0.0181	Ceramic: 2 μm filaments at 1600 μm/s	[108]
	LLNL DIW	610	21041	20 mm/s	[109]
	LLNL DIW	250	1767	10 mm/s	Personal correspondence
Comm. SLA	3DS ProJet 12000	45	16254	56 μm XY, 30 μm layer rez; 43x27mm area x 14mm/hr	3DS website specs
	Autodesk Ember	50	46080	50 μm XY, 50 μm layer rez; 64x40mm area x 18 mm/hr	Autodesk website
	FormLabs Form2	100	2000	2 cm/hr, ~10x10mm area; rook example part	Formlabs website specs
Comm. SLS	3DS sPro 230 HD-HS	100	300000	3.0 L/hr, 100 μm layers/XY rez	3DS website specs
	EOS P770	250	1000000	400 μm laser spot x100 μm layer x 20 m/s scan speed	EOS website spec datasheet

Appendix B

Selected Important MATLAB Functions, Methods and Scripts

B.1 Resin Parameter Space Calculation (generates Figure 4.3)

```
concvec=logspace(-4,-1.5,30); % PI concentration vector, units mol/L
IntVec=logspace(-3,0,30); % light intensity vector, units mW/cm^2
epSet=[3,10,30,100,300]; % extinction coefficients, L/mol/cm
alphaSet=[0.03,0.1,0.3,1]; % abrosprtion factor, 1/cm
t_iTGT=10; % target curing time, seconds
O2_conc=1E-3; % estimated equilibrium O2, mol/L
O2cm=O2_conc/1000; % mol/cm^3
N_A=6.022E23; % Avogadro's number 1/mol
hv=3.734E-19; % J/photon at 532nm

for j=1:numel(epSet)
    alphas(:,j)=concvec*epSet(j);
    % calculate volume absorption factor at z=0.5 according to Eq. 4.14
    AbsFac1(:,j)=2.3*alphas(:,j).*exp(-2.3*alphas(j)*0.5);
end;
% invert combination of Eq 4.9, 4.13, 4.14 to calculate needed intensity
I_req1=1/3*O2cm/t_iTGT./AbsFac1*N_A*hv;

% graphics handling block: plot varied epsilons for constant alpha values
figure; loglog(concvec*1000,I_req1*1000);
xlabel('[PI] (mM)'); ylabel (['intensity to cure in ',num2str(t_iTGT),' s
(mW/cm^2)']);
hold on; axis([0.1 30 1 1000]);  ax=gca; ax.FontSize=14;
for j=1:numel(epSet)

txthandle=text(concvec(4)*1000,max(I_req1(:,j)*100),['\epsilon=',num2str(epSe
t(j)),' L/(mol*cm)']);
    txthandle.FontSize=14;
end;

for k=1:numel(alphaSet)
    alphaS2(:,k)=repmat(alphaSet(k),[numel(concvec) 1]);
    AbsFac2(:,k)=2.3*alphaS2(:,k).*exp(-2.3*alphaS2(k)*0.5);
end;

% Analogous calculations as above, but varied alpha values for constant
% epsilons (gives horizontal lines)
I_req2=1/3*O2cm/t_iTGT./AbsFac2*N_A*hv;
loglog(concvec*1000,I_req2*1000);% ax.gca;

for k=1:numel(alphaSet)

txthandle=text(concvec(20)*1000,min(I_req2(:,k)*1250),['\alpha=',num2str(alph
aSet(k)),' cm^{-1}']);
    txthandle.FontSize=14;
end;
```

B.2 3D Beam Superposition & Absorption Coefficient Model (for Section 5.1.1 and Figure 5.2)

```
clear all;
% alphas=[0.001,0.002,0.005,0.010,0.02, 0.05, 0.1]; % 1/cm
% compExpFactor=[0.25, 0.38, 0.62, 0.8, 0.95, 1.2, 1.8]; % empirical factor
for balanced compensation
[cuvX,cuvY,cuvZ]=meshgrid(0:0.05:10,0:0.05:10,0:0.05:10); % set up spatial
grid within build volume, units mm

A=0.045; % units of 1/mm; for 1/cm multiply by 10

%resin attenuation along each direction
IabsY=2.3*A*exp(-2.3*A*cuvX);
IabsX=2.3*A*exp(-2.3*A*cuvY);
IabsZ=2.3*A*exp(-2.3*A*cuvZ);
Iabs3D=(IabsX+IabsY+IabsZ); % total I_abs value from superimposed beams
Iabs3Dnorm=(IabsX+IabsY+IabsZ)/3; % mean I_abs value at all points in space
Cratio=13; % contrast ratio between white and black-projected areas

Iabs3Dmax=Iabs3D(41,41,41); % max possible three-beam absorption
MissingIx=0.5*(Iabs3Dmax-Iabs3D(:,:,160)); % Eq. 5.2
MissingIy=0.5*(Iabs3Dmax-Iabs3D(:,:,160));
XprofileAdj=(IabsX(160,160,160)+max(max(MissingIx))+MissingIx); % Eq. 5.1
YprofileAdj=(IabsY(160,160,160)+max(max(MissingIy))+MissingIy);
XYprofileAdj=(XprofileAdj.*YprofileAdj);

% set up illumination pattern of the square box
Boxprofile=ones(size(Iabs3D(:,:,1)))/Cratio;
Boxprofile(41:64,41:160)=1; Boxprofile(136:160,41:160)=1;
Boxprofile(41:160,41:64)=1; Boxprofile(41:160,136:160)=1;

BoxAdj=Boxprofile.*(XYprofileAdj.^1.1); % selected value of compExpFactor
from above (chosen based on alpha) is used here as the exponent
BoxAdj=BoxAdj/max(max(BoxAdj));

% imprint attenuation in each dimension on the three intensity images,
calculate absorption due to each beam
for i=1:size(IabsX,1)
    Xbeam(i,:,:)=squeeze(IabsX(i,:,:)).*BoxAdj;
end;
for j=1:size(IabsY,2)
    Ybeam(:,j,:)=squeeze(IabsY(:,j,:)).*BoxAdj;
end;
for k=1:size(IabsZ,3)
    Zbeam(:,:,k)=squeeze(IabsZ(:,:,k)).*BoxAdj;
end;

IabsT=Xbeam+Ybeam+Zbeam; % superimpose absorbed energy from all beams

%% graphics handling block
axisMax=ceil(max(IabsT(50,:,101)*1.25*10))/10;

% plot a planar slice through the 3D geometry
```

```
figure; subplot(1,2,1);
pcolor(IabsT(:,:,101)); shading interp; axis equal; axis([1 201 1 201]);
colormap jet; colorbar; caxis([0 axisMax]); title(['\alpha=',num2str(A*10),'
cm^{-1}']);
xlabel('x coordinate (mm)'); ylabel('y coordinate (mm)');
ax = gca;
ax.XTick = [1,41,81,121,161,201]; ax.YTick = [1,41,81,121,161,201];
ax.XTickLabel = [0,2,4,6,8,10]; ax.YTickLabel = [0,2,4,6,8,10];

% plot line-scans through the 3D geometry at a couple depths and Y positions
subplot(1,2,2);
plot(cuvX(1,:,101),IabsT(51,:,66),'LineWidth',1,'Color','r'); hold on;
plot(cuvX(1,:,101),IabsT(151,:,66),'LineWidth',1,'Color','k');
plot(cuvX(1,:,101),IabsT(51,:,132),'--','LineWidth',1,'Color','r');
plot(cuvX(1,:,101),IabsT(151,:,132),'--','LineWidth',1,'Color','k');
axis ([0 10 0 axisMax]); title(['z=3.3 mm, \alpha=', num2str(A*10),' cm^{-
1}']);
xlabel('spatial coordinate (mm)'); ylabel('total absorption coeff. (cm^{-
1})');
lgdHandle = legend('show');
lgdHandle.String={'y=2.5 mm, z=3.3 mm','y=7.5 mm, z=3.3 mm','y=2.5 mm, z=6.6
mm','y=7.5 mm, z=6.6 mm'};

%% uniformity calculation block
% calculate absorbed energy values at a variety of points throughout
% structure and max/min absorbed values
MaxCornerIabs=mean(mean(mean(IabsT(41:62,41:62,41:62))));
MinCornerIabs=mean(mean(mean(IabsT(138:158,138:158,138:158))));
MidPlaneIabs(1)=mean(mean(IabsT(41:62,41:62,66)));
MidPlaneIabs(2)=mean(mean(IabsT(41:62,138:158,66)));
MidPlaneIabs(3)=mean(mean(IabsT(138:158,41:62,66)));
MidPlaneIabs(4)=mean(mean(IabsT(138:158,138:158,66)));
MidPlaneIabs(5)=mean(mean(IabsT(41:62,41:62,132)));
MidPlaneIabs(6)=mean(mean(IabsT(41:62,138:158,132)));
MidPlaneIabs(7)=mean(mean(IabsT(138:158,41:62,132)));
MidPlaneIabs(8)=mean(mean(IabsT(138:158,138:158,132)));

AllIabsVals=[MaxCornerIabs,MinCornerIabs,MidPlaneIabs];
RSDall=std(AllIabsVals)/mean(AllIabsVals);

% output uniformity calculations to standard output
disp(['MaxCorner =', num2str(MaxCornerIabs), '  MinCorner =',
   num2str(MinCornerIabs), ' 1/cm']);
disp(['z=5.0mm Iabs =', num2str(MidPlaneIabs), ' 1/cm']);
disp(['MeanIabs =', num2str(mean(AllIabsVals)), ' 1/cm; range=',
   num2str((max(AllIabsVals)-min(AllIabsVals))/mean(AllIabsVals)*100), '%']);
disp(['MeanRSD ', num2str(RSDall*100),'%']);
```

B.3 Gerchberg-Saxton Algorithm With Gaussian Intensity Profile

```
function [phi_out] = GSalgGauss(I_target, numIts, I_src)
% Gerchberg-Saxton algorithm with non-uniform (Gaussian) intensity profile.
% Default Gaussian has sigma width parameter equivalent to 1/4 diagonal.
% Input parameters are target image and source illumination intensity
% Runs for a fixed number of iterations.
% Variable naming convention:
% --> E_x : complex-valued electric field x
% --> A_x : real-valued amplitude of field x {= abs(E_x)}
% --> I_x : real-valued intensity of field x {= (A_x).^2}
% --> phi_x : phase of field x {= angle(x)}, calculated range -pi to pi

[Ypx,Xpx]=size(I_target);
if Xpx ~= Ypx
    disp('Source image for CGH is not square!');
    phi_out=zeros(Ypx,Xpx);
    return;
end;

% set up grid for Gaussian illumination and generate intensity profile
if (nargin < 3)
    DefaultSigma=sqrt(Xpx^2+Ypx^2)/4;
    [Xcoord,Ycoord]=meshgrid(-Xpx/2+1:1:Xpx/2, -Ypx/2+1:1:Ypx/2);
    I_src = exp(-(sqrt(Xcoord.^2+Ycoord.^2)./(DefaultSigma)).^2/2);
end;

if (nargin < 2) numIts=20;
end;

%% prepare source image: shift (account for FFT's shift), normalize and plot
I_tgtShift = single(fftshift(I_target));
I_tgtNormShift = I_tgtShift/max(max(single(I_tgtShift)));

%% initialize G-S loop variables

A_B = sqrt(I_src); % source intensity distribution converted to amplitude
E_A = ifft2(I_tgtNormShift); %A is first approx. of source field by inverse
FT from target image

%% Gerchberg-Saxton iterative loop
for iterCnt=1:numIts
    E_B = A_B.*exp(1i*angle(E_A)); % B is complex field at SLM
    E_C = fft2(E_B); % C is projection of complex field at target (projecting
the SLM field)
    E_D = sqrt(abs(I_tgtNormShift)).*exp(1i*angle(E_C)); % D is target
amplitude profile w/ phase data from latest iteration
    E_A = ifft2(E_D);
end;

phi_out = angle(E_A);
```

B.4 Script to Calculate "Stack" of CGH Phase Masks for Rapid Cycling on the SLM

```
function [phiStack,CGHstack] = genCGHstack_wrapper(outFile, inFile)
% This function generates a stack of CGHs from one source image to be cycled
% on the SLM; includes defocus (lens shift) and vignetting compensation
% (VComp)
%
% INPUTS:
% outFile: output filename
% inFile: input filename (optional, can omit and pick via dialog)
%
% OUTPUTS:
% phiStack: Stack of phase values, -pi to pi
% CGHstack: Stack of CGHs, adjusted for 8 bit grayscale

%% Input parsing block
prms=LoadSysParams;
disp(['Generating stack of ' num2str(prms.CGHstackSize) ' CGHs.']);

if (nargin < 2)
    [inFile, inFilePath] = file_path_retrieve ('C:\~holoAM-COMMON');
end;

if (nargin < 1)
    outFname =
strcat(num2str(prms.CGHstackSize),'CGHstack_defautOutput.mat');
    outFile=strcat(inFilePath,outFname);
end;

%% Read source image and check size
sourceImg=single(imread(strcat(inFilePath,inFile{1})));
sourceImg=sourceImg./max(max(sourceImg)); %normalize

[Ypx,Xpx]=size(sourceImg);
if Ypx ~= prms.TgtImYpx || Xpx ~= prms.TgtImXpx
    disp('Source image size is unexpected!');
    return;
end;

% apply vignetting compensation
load(prms.CurrentVCompFile, 'VCompMatrix');
sourceImg=sourceImg.*VCompMatrix;

% calculate absorbance adjustment matrix (AAM) and apply correction
% this is a variation on the function given in Appendix B.2
sourceImg=sourceImg.*calcAAM (sourceImg);

% Calculate Gaussian illumination profile
sigma=sqrt(Xpx^2+Ypx^2)/4;
[Xcoord,Ycoord]=meshgrid(-Xpx/2+1:1:Xpx/2, -Ypx/2+1:1:Ypx/2);
I_src = exp(-(sqrt(Xcoord.^2+Ycoord.^2)./(sigma)).^2/2);
```

```
%% Calculate lens shift (defocus)
lensShMatrix=lensShiftRadiansCalcOnly(prms.df,prms.lambda,prms.SLMpxPitch,prm
s.SLMypx,prms.SLMxpx);

timeStamp=tic;  % start timer to measure speed of calculations

%% Calculate CGHs
parpool(4) % use parallel computing capability for speedup
disp('CGHs done: ');

parfor k = 1:prms.CGHstackSize % use this for loop when using parallel proc.
% for k = 1:prms.CGHstackSize % use this for loop for regular
    rawPhi = GSloopOnly(sourceImg, prms.GSiters, I_src); % sized 1920x1920
    rawPhi = rawPhi(421:1500,:); % select the SLM-size central 1080x1920 area
    phiStack(:,:,k)=mod(rawPhi-lensShMatrix,prms.SLMmodDepth);
    CGHstack(:,:,k)=fliplr(uint8(phiStack(:,:,k)/prms.SLMmodDepth*255));
    if (mod(k,10)==0)
        disp([' ' num2str(k)]);
    end;
end

toc(timeStamp)

save(outFile,'CGHstack');
```

B.5 System Parameter Loading Function

```
function SysParams = LoadSysParams()
% This function defines variables used by various functions
% SysParams: Struct containing variables

%% Calibration
SysParams.SLMmodDepth = 2.1*pi; %SLM phase modulation at 255 gray value,
assume linear scale
SysParams.PrevCurvCompFile = '20170112-CurvComp_radians.mat'; %Filename
containing curvature compensation data
SysParams.CurrentVCompFile = 'VCompMatrix_MS_20170509.mat';
SysParams.df = -0.026; % Defocusing of hologram beyond FTL focal. Positive
for shifts downrange. Unit: [m]
SysParams.lambda = 405e-9; % Laser wavelength [m]
SysParams.stgDirectionFlag=1;
SysParams.PSIFpause=0.5; % time to pause between collecting each of the 5
Hariharan interferometry frames

SysParams.VigComp_Exp = 200; % Camera exposure time for Vignetting
Compensation (may be different from otherwise because of uniform target
image) [us]
SysParams.VigComp_ROI = [750 300 2300 1850]; % Cam pixels where Vignetting
Compensation should be calculated [xLeft yTop xRight yBot]

 %% Hologram generation
SysParams.GSiters = 15; %Number of GS iterations
SysParams.VigComp = true; %Apply vignetting correction (LSC a.k.a.
"vignetting")
SysParams.CGHstackSize = 600; %Number of holograms to generate for each
target image

%% SLM properties and control
SysParams.SLMypx = 1080; %Number of SLM pixel rows
SysParams.SLMxpx = 1920; %Number of SLM pixel columns
SysParams.SLMpxPitch = 8E-6;
SysParams.SLMinitImage=imread('CGH_TH_Quads&Blocks-1920defoc.png');
```

B.6 Main SLM Hardware Control Functions

(The SLM microdisplay is addressed as an additional monitor attached to the system, and controlled via the PsychToolbox package (http://psychtoolbox.org/) an open-source set of hardware control tools originally designed for accurately-timed presentation of graphical/visual stimuli for cognitive research).

SLM Initialization

```
function SLM = SLMinit_PTB(initImage)
% This function initializes the SLM using PsychToolbox
% SLM: Identifier for the SLM output by the function

[SLMypx,SLMxpx]=size(initImage);
if (SLMxpx ~= 1920 || SLMypx ~= 1080)
    disp('Initial SLM image must be 1080x1920 pixels!');
    return;
end;

% Open and initialize SLM window
SLM.window = Screen('Preference','SkipSyncTests',1);
SLM.window = Screen('OpenWindow',2);

% Put something on the screen to catch any (one-time) warnings
Screen('PutImage',SLM.window,initImage);
Screen('Flip',SLM.window); % draw new image on SLM screen
```

Rapid Cycling of Images on the SLM from a Stack of CGHs

```
function SLMloopFast(SLM,CGHstack)

CGHstackSize=size(CGHstack,3);

while 1
    t = tic; % use timing to determine actual output framerate
    for k = 1:CGHstackSize
        SLMtextureData=Screen('MakeTexture',SLM.window,CGHstack(:,:,k));
        Screen('DrawTexture',SLM.window,SLMtextureData);
        Screen('Flip',SLM.window); % draw new texture on SLM screen
        pause(0.01); % prevents runaway looping - 100 Hz max speed, hardware
                        only capable of 60 Hz
        Screen('Close',SLMtextureData);
    end
    disp(['Current SLM FPS:', num2str(round(CGHstackSize/toc(t)))])
end
```

References

1. I. Gibson, D. Rosen, and B. Stucker, *Additive Manufacturing Technologies* (Springer New York, 2015).

2. C. W. Hull, "Apparatus for production of three-dimensional objects by stereolithography," U.S. patent 4575330 (March 11, 1986).

3. C. R. Deckard, "Method and apparatus for producing parts by selective sintering," U.S. patent 4863538 (September 5, 1989).

4. S. Singh, S. Ramakrishna, and R. Singh, "Material issues in additive manufacturing: A review," J. Manuf. Process. **25**, 185–200 (2017).

5. M. Zavala-Arredondo, N. Boone, J. Willmott, D. T. D. Childs, P. Ivanov, K. M. Groom, and K. Mumtaz, "Laser diode area melting for high speed additive manufacturing of metallic components," Mater. Des. **117**, 305–315 (2017).

6. L. R. Meza, S. Das, and J. R. Greer, "Strong, lightweight, and recoverable three-dimensional ceramic nanolattices," Science **345**, 1322–1326 (2014).

7. L. Li, A. Tirado, I. C. Nlebedim, O. Rios, B. Post, V. Kunc, R. R. Lowden, E. Lara-Curzio, R. Fredette, J. Ormerod, T. A. Lograsso, and M. P. Paranthaman, "Big Area Additive Manufacturing of High Performance Bonded NdFeB Magnets," Sci. Rep. **6**, (2016).

8. T. Bückmann, M. Thiel, M. Kadic, R. Schittny, and M. Wegener, "An elasto-mechanical unfeelability cloak made of pentamode metamaterials," Nat. Commun. **5**, (2014).

9. X. Zheng, H. Lee, T. H. Weisgraber, M. Shusteff, J. DeOtte, E. B. Duoss, J. D. Kuntz, M. M. Biener, Q. Ge, J. A. Jackson, S. O. Kucheyev, N. X. Fang, and C. M. Spadaccini, "Ultralight, ultrastiff mechanical metamaterials," Science **344**, 1373–1377 (2014).

10. R. Guo, Z. Li, Z. Jiang, D. Yuan, W. Huang, and A. Xia, "Log-pile photonic crystal fabricated by two-photon photopolymerization," J. Opt. Pure Appl. Opt. **7**, 396–399 (2005).

11. A. D. Boardman, V. V. Grimalsky, Y. S. Kivshar, S. V. Koshevaya, M. Lapine, N. M. Litchinitser, V. N. Malnev, M. Noginov, Y. G. Rapoport, and V. M. Shalaev, "Active and tunable metamaterials," Laser Photonics Rev. **5**, 287–307 (2011).

12. Y. Lee, X. Lu, Y. Hao, S. Yang, R. Ubic, J. R. G. Evans, and C. G. Parini, "Directive millimetre-wave antenna based on freeformed woodpile EBG structure," Electron. Lett. **43**, 195 (2007).

13. J. Xu, X. Jiang, N. Fang, E. Georget, R. Abdeddaim, J.-M. Geffrin, M. Farhat, P. Sabouroux, S. Enoch, and S. Guenneau, "Molding acoustic, electromagnetic and water waves with a single cloak," Sci. Rep. **5**, 10678 (2015).

14. F. P. W. Melchels, J. Feijen, and D. W. Grijpma, "A review on stereolithography and its applications in biomedical engineering," Biomaterials **31**, 6121–6130 (2010).

15. C. Y. Yap, C. K. Chua, Z. L. Dong, Z. H. Liu, D. Q. Zhang, L. E. Loh, and S. L. Sing, "Review of selective laser melting: Materials and applications," Appl. Phys. Rev. **2**, 041101 (2015).

16. T. Gissibl, S. Thiele, A. Herkommer, and H. Giessen, "Two-photon direct laser writing of ultracompact multi-lens objectives," Nat. Photonics **10**, 554–560 (2016).

17. J. A. Lewis, "Direct Ink Writing of 3D Functional Materials," Adv. Funct. Mater. **16**, 2193–2204 (2006).

18. W. Chen, L. Thornley, H. G. Coe, S. J. Tonneslan, J. J. Vericella, C. Zhu, E. B. Duoss, R. M. Hunt, M. J. Wight, D. Apelian, A. J. Pascall, J. D. Kuntz, and C. M. Spadaccini, "Direct metal writing: Controlling the rheology through microstructure," Appl. Phys. Lett. **110**, 094104 (2017).

19. A. J. L. Morgan, L. Hidalgo San Jose, W. D. Jamieson, J. M. Wymant, B. Song, P. Stephens, D. A. Barrow, and O. K. Castell, "Simple and Versatile 3D Printed Microfluidics Using Fused Filament Fabrication," PLOS ONE **11**, e0152023 (2016).

20. X. Zheng, J. Deotte, M. P. Alonso, G. R. Farquar, T. H. Weisgraber, S. Gemberling, H. Lee, N. Fang, and C. M. Spadaccini, "Design and optimization of a light-emitting diode projection micro-stereolithography three-dimensional manufacturing system," Rev. Sci. Instrum. **83**, 125001 (2012).

21. M. P. Lee, G. J. T. Cooper, T. Hinkley, G. M. Gibson, M. J. Padgett, and L. Cronin, "Development of a 3D printer using scanning projection stereolithography," Sci. Rep. **5**, (2015).

22. J. R. Tumbleston, D. Shirvanyants, N. Ermoshkin, R. Janusziewicz, A. R. Johnson, D. Kelly, K. Chen, R. Pinschmidt, J. P. Rolland, A. Ermoshkin, E. T. Samulski, and J. M. DeSimone, "Continuous liquid interface production of 3D objects," Science **347**, 1349–1352 (2015).

23. M. J. Matthews, G. Guss, D. R. Drachenberg, J. A. Demuth, J. E. Heebner, E. B. Duoss, J. D. Kuntz, and C. M. Spadaccini, "Diode-based additive manufacturing of metals using an optically-addressable light valve," Opt. Express **25**, 11788 (2017).

24. Y. Lin, A. Harb, K. Lozano, D. Xu, and K. P. Chen, "Five beam holographic lithography for simultaneous fabrication of three dimensional photonic crystal templates and line defects using phase tunable diffractive optical element," Opt. Express **17**, 16625 (2009).

25. K. Ohlinger, J. Lutkenhaus, B. Arigong, H. Zhang, and Y. Lin, "Spatially addressable design of gradient index structures through spatial light modulator based holographic lithography," J. Appl. Phys. **114**, 213102 (2013).

26. H. Ning, J. H. Pikul, R. Zhang, X. Li, S. Xu, J. Wang, J. A. Rogers, W. P. King, and P. V. Braun, "Holographic patterning of high-performance on-chip 3D lithium-ion microbatteries," Proc. Natl. Acad. Sci. **112**, 6573–6578 (2015).

27. L. Yuan and P. R. Herman, "Laser Scanning Holographic Lithography for Flexible 3D Fabrication of Multi-Scale Integrated Nano-structures and Optical Biosensors," Sci. Rep. **6**, (2016).

28. M. C. R. Leibovici and T. K. Gaylord, "Photonic-crystal waveguide structure by pattern-integrated interference lithography," Opt. Lett. **40**, 2806 (2015).

29. M. C. R. Leibovici and T. K. Gaylord, "Custom-modified three-dimensional periodic microstructures by pattern-integrated interference lithography," J. Opt. Soc. Am. A **31**, 1515 (2014).

30. D. Dendukuri, S. S. Gu, D. C. Pregibon, T. A. Hatton, and P. S. Doyle, "Stop-flow lithography in a microfluidic device," Lab. Chip **7**, 818 (2007).

31. K. S. Paulsen and A. J. Chung, "Non-spherical particle generation from 4D optofluidic fabrication," Lab Chip **16**, 2987–2995 (2016).

32. D. S. (Danny) Kim, Y.-T. Kao, and B. L. Tai, "Hydrostatic 3D-printing for soft material structures using low one-photon polymerization," Manuf. Lett. **10**, 6–9 (2016).

33. P. Gandhi and K. Bhole, "Characterization of "Bulk Lithography" Process for Fabrication of Three-Dimensional Microstructures," J. Micro Nano-Manuf. **1**, 041002 (2013).

34. G. Saxby and S. Zacharovas, *Practical Holography*, Fourth edition (CRC Press, imprint of the Taylor & Francis Group, 2016).

35. A. Bertsch, S. Jiguet, P. Bernhard, and P. Renaud, "Microstereolithography: a review," in *MRS Proceedings* (Cambridge Univ Press, 2002), Vol. 758, pp. LL1–1.

36. X. Zheng, W. Smith, J. Jackson, B. Moran, H. Cui, D. Chen, J. Ye, N. Fang, N. Rodriguez, T. Weisgraber, and C. M. Spadaccini, "Multiscale metallic metamaterials," Nat. Mater. **15**, 1100–1106 (2016).

37. D. Gabor, "A New Microscopic Principle," Nature **161**, 777–778 (1948).

38. U. Schnars and W. P. Jüptner, "Digital recording and numerical reconstruction of holograms," Meas. Sci. Technol. **13**, R85 (2002).

39. G. Saxby, *Practical Holography*, 3. ed (Inst. of Physics Publ, 2004).

40. O. V. Andreeva, Y. L. Korzinin, and B. G. Manukhi, "Volume Transmission Hologram Gratings — Basic Properties, Energy Channelizing, Effect of Ambient Temperature and Humidity," in *Holography - Basic Principles and Contemporary Applications*, E. Mihaylova, ed. (InTech, 2013).

41. M. K. Kim, *Digital Holographic Microscopy*, Springer Series in Optical Sciences (Springer New York, 2011), Vol. 162.

42. J. W. Goodman, *Introduction to Fourier Optics*, 3. ed (Roberts & Company, 2005).

43. J. R. Fienup, "Phase retrieval algorithms: a comparison," Appl. Opt. **21**, 2758 (1982).

44. M. A. Seldowitz, J. P. Allebach, and D. W. Sweeney, "Synthesis of digital holograms by direct binary search," Appl. Opt. **26**, 2788–2798 (1987).

45. T. Haist, M. Schönleber, and H. J. Tiziani, "Computer-generated holograms from 3D-objects written on twisted-nematic liquid crystal displays," Opt. Commun. **140**, 299–308 (1997).

46. M. Polin, K. Ladavac, S.-H. Lee, Y. Roichman, and D. Grier, "Optimized holographic optical traps," Opt. Express **13**, 5831–5845 (2005).

47. R. Di Leonardo, F. Ianni, and G. Ruocco, "Computer generation of optimal holograms for optical trap arrays," Opt. Express **15**, 1913–1922 (2007).

48. R. W. Gerchberg and W. O. Saxton, "A Practical Algorithm for the Determination of Phase from Image and Diffraction Plane Pictures," Optik **35**, 227–246 (1972).

49. G. Whyte and J. Courtial, "Experimental demonstration of holographic three-dimensional light shaping using a Gerchberg–Saxton algorithm," New J. Phys. **7**, 117–117 (2005).

50. G. Lazarev, A. Hermerschmidt, S. Krüger, and S. Osten, *LCOS Spatial Light Modulators: Trends and Applications* (Wiley-VCH, 2012).

51. W. P. Bleha and L. A. Lei, "Advances in Liquid Crystal on Silicon (LCOS) spatial light modulator technology," in D. D. Desjardins and K. R. Sarma, eds. (2013), p. 87360A.

52. Z. Zhang, Z. You, and D. Chu, "Fundamentals of phase-only liquid crystal on silicon (LCOS) devices," Light Sci. Appl. **3**, e213 (2014).

53. A. Jesacher, C. Maurer, A. Schwaighofer, S. Bernet, and M. Ritsch-Marte, "Near-perfect hologram reconstruction with a spatial light modulator," Opt. Express **16**, 2597 (2008).

54. H. Yoshikawa, "Image Quality Evaluation of a Computer-Generated Hologram," in (OSA, 2015), p. DT2A.8.

55. Y. Deng and D. Chu, "Filling factor characteristics of masking phase-only hologram on the quality of reconstructed images," in H. I. Bjelkhagen and V. M. Bove, eds. (2016), p. 97710M.

56. D. Palima and V. R. Daria, "Holographic projection of arbitrary light patterns with a suppressed zero-order beam," Appl. Opt. **46**, 4197–4201 (2007).

57. H. Zhang, J. Xie, J. Liu, and Y. Wang, "Elimination of a zero-order beam induced by a pixelated spatial light modulator for holographic projection," Appl. Opt. **48**, 5834–5841 (2009).

58. E. Ronzitti, M. Guillon, V. de Sars, and V. Emiliani, "LCoS nematic SLM characterization and modeling for diffraction efficiency optimization, zero and ghost orders suppression," Opt. Express **20**, 17843–17855 (2012).

59. J. Liang, S.-Y. Wu, F. K. Fatemi, and M. F. Becker, "Suppression of the zero-order diffracted beam from a pixelated spatial light modulator by phase compression," Appl. Opt. **51**, 3294–3304 (2012).

60. D. Briers, D. D. Duncan, E. Hirst, S. J. Kirkpatrick, M. Larsson, W. Steenbergen, T. Stromberg, and O. B. Thompson, "Laser speckle contrast imaging: theoretical and practical limitations," J. Biomed. Opt. **18**, 066018 (2013).

61. J. Bingi and V. M. Murukeshan, "Speckle lithography for fabricating Gaussian, quasi-random 2D structures and black silicon structures," Sci. Rep. **5**, (2016).

62. Y. Mizuyama, N. Harrison, and R. Leto, "Despeckling fly's eye homogenizer for single mode laser diodes," Opt. Express **21**, 9081 (2013).

63. K. Curtis, "Apparatus for despeckling laser systems and methods thereof," U.S. patent US9158063 B2 (October 13, 2015).

64. F. Wyrowski and O. Bryngdahl, "Speckle-free reconstruction in digital holography," J. Opt. Soc. Am. A **6**, 1171 (1989).

65. S. Zwick, T. Haist, M. Warber, and W. Osten, "Dynamic holography using pixelated light modulators," Appl. Opt. **49**, F47 (2010).

66. A. Georgiou, J. Christmas, J. Moore, A. Jeziorska-Chapman, A. Davey, N. Collings, and W. A. Crossland, "Liquid crystal over silicon device characteristics for holographic projection of high-definition television images," Appl. Opt. **47**, 4793–4803 (2008).

67. T. Haist and W. Osten, "Holography using pixelated spatial light modulators—part 1: theory and basic considerations," J. MicroNanolithography MEMS MOEMS **14**, 041310 (2015).

68. D. Engström, M. Persson, J. Bengtsson, and M. Goksör, "Calibration of spatial light modulators suffering from spatially varying phase response," Opt. Express **21**, 16086 (2013).

69. J. Min, B. Yao, P. Gao, R. Guo, J. Zheng, and T. Ye, "Parallel phase-shifting interferometry based on Michelson-like architecture," Appl. Opt. **49**, 6612 (2010).

70. R. Leach, ed., *Optical Measurement of Surface Topography* (Springer Berlin Heidelberg, 2011).

71. J. Fischer and M. Wegener, "Three-dimensional optical laser lithography beyond the diffraction limit: 3D optical lithography off limits," Laser Photonics Rev. **7**, 22–44 (2013).

72. J. Xia, "Three-dimensional light modulation using phase-only spatial light modulator," Opt. Eng. **48**, 020502 (2009).

73. P. Wang and R. Menon, "Optical microlithography on oblique and multiplane surfaces using diffractive phase masks," J. MicroNanolithography MEMS MOEMS **14**, 023507–023507 (2015).

74. G. Shabtay, "Three-dimensional beam forming and Ewald's surfaces," Opt. Commun. **226**, 33–37 (2003).

75. F. J. Martínez, A. Márquez, S. Gallego, J. Franc?s, and I. Pascual, "Extended linear polarimeter to measure retardance and flicker: application to liquid crystal on silicon devices in two working geometries," Opt. Eng. **53**, 014105 (2014).

76. F. J. Martínez, A. Márquez, S. Gallego, M. Ortuño, J. Francés, A. Beléndez, and Inmaculada Pascual, "Electrical dependencies of optical modulation capabilities in digitally addressed parallel aligned liquid crystal on silicon devices," Opt. Eng. **53**, 067104 (2014).

77. J. Rosen, G. Brooker, G. Indebetouw, and N. T. Shaked, "A Review of Incoherent Digital Fresnel Holography," J. Hologr. Speckle **5**, 124–140 (2009).

78. J. Rosen, R. Kelner, and Y. Kashter, "Incoherent digital holography with phase-only spatial light modulators," J. MicroNanolithography MEMS MOEMS **14**, 041307–041307 (2015).

79. M. Shusteff, J. K. Dudoff, A. E. M. Browar, L. A. Shaw, R. M. Panas, J. B. Hopkins, N. X. Fang, and C. M. Spadaccini, "Optimal Source Beam Shaping for Digital Holographic Lithography," in *Proceedings of the 2016 Imaging and Applied Optics Congress* (The Optical Society, 2016), p. DW1D.2.

80. N. J. Jenness, R. T. Hill, A. Hucknall, A. Chilkoti, and R. L. Clark, "A versatile diffractive maskless lithography for single-shot and serial microfabrication," Opt. Express **18**, 11754–11762 (2010).

81. M. Mahamdeh, C. Pérez Campos, and E. Schäffer, "Under-filling trapping objectives optimizes the use of the available laser power in optical tweezers," Opt. Express **19**, 11759 (2011).

82. A. Laskin, "Solutions for Beam Shaping: Control of laser intensity profile and spot shape with refractive beam shaping," Laser Tech. J. **10**, 37–40 (2013).

83. A. Laskin, V. Laskin, and A. Ostrun, "Beam shaping for holographic techniques," in *Proceedings of SPIE*, S. Yin and R. Guo, eds. (SPIE, 2014), Vol. 9200, p. 92000E.

84. M. Degirmenci, A. Onen, Y. Yagci, and S. P. Pappas, "Photoinitiation of cationic polymerization by visible light activated titanocene in the presence of onium salts," Polym. Bull. **46**, 443–449 (2001).

85. D. Sabol, M. R. Gleeson, S. Liu, and J. T. Sheridan, "Photoinitiation study of Irgacure 784 in an epoxy resin photopolymer," J. Appl. Phys. **107**, 053113 (2010).

86. K. Matyjaszewski, ed., *Handbook of Radical Polymerization* (Wiley-Interscience, 2002).

87. B. M. Mandal, *Fundamentals of Polymerization* (World Scientific, 2013).

88. K. S. Anseth, C. M. Wang, and C. N. Bowman, "Reaction behaviour and kinetic constants for photopolymerizations of multi(meth)acrylate monomers," Polymer **35**, 3243–3250 (1994).

89. K. Taki, Y. Watanabe, H. Ito, and M. Ohshima, "Effect of Oxygen Inhibition on the Kinetic Constants of the UV-Radical Photopolymerization of Diurethane Dimethacrylate/Photoinitiator Systems," Macromolecules **47**, 1906–1913 (2014).

90. C. Decker and A. D. Jenkins, "Kinetic approach of oxygen inhibition in ultraviolet- and laser-induced polymerizations," Macromolecules **18**, 1241–1244 (1985).

91. S. C. Ligon, B. Hus?r, H. Wutzel, R. Holman, and R. Liska, "Strategies to Reduce Oxygen Inhibition in Photoinduced Polymerization," Chem. Rev. **114**, 557–589 (2014).

92. Q. Ge, A. H. Sakhaei, H. Lee, C. K. Dunn, N. X. Fang, and M. L. Dunn, "Multimaterial 4D Printing with Tailorable Shape Memory Polymers," Sci. Rep. **6**, (2016).

93. A. K. O'Brien and C. N. Bowman, "Impact of Oxygen on Photopolymerization Kinetics and Polymer Structure," Macromolecules **39**, 2501–2506 (2006).

94. J. S. Oakdale, J. Ye, W. L. Smith, and J. Biener, "Post-print UV curing method for improving the mechanical properties of prototypes derived from two-photon lithography," Opt. Express **24**, 27077 (2016).

95. P. J. Flory, "Molecular Size Distribution in Three Dimensional Polymers. I. Gelation," J. Am. Chem. Soc. **63**, 3083–3090 (1941).

96. P. J. Flory, "Constitution of Three-dimensional Polymers and the Theory of Gelation.," J. Phys. Chem. **46**, 132–140 (1942).

97. W. H. Stockmayer, "Theory of Molecular Size Distribution and Gel Formation in Branched-Chain Polymers," J. Chem. Phys. **11**, 45–55 (1943).

98. W. H. Stockmayer, "Theory of Molecular Size Distribution and Gel Formation in Branched Polymers II. General Cross Linking," J. Chem. Phys. **12**, 125–131 (1944).

99. A. Thakur, A. K. Banthia, and B. R. Maiti, "Studies on the kinetics of free-radical bulk polymerization of multifunctional acrylates by dynamic differential scanning calorimetry," J. Appl. Polym. Sci. **58**, 959–966 (1995).

100. M. D. Goodner and C. N. Bowman, "Development of a comprehensive free radical photopolymerization model incorporating heat and mass transfer effects in thick films," Chem. Eng. Sci. **57**, 887–900 (2002).

101. J. B. Mueller, J. Fischer, F. Mayer, M. Kadic, and M. Wegener, "Polymerization Kinetics in Three-Dimensional Direct Laser Writing," Adv. Mater. **26**, 6566–6571 (2014).

102. S. Wu, J. Serbin, and M. Gu, "Two-photon polymerisation for three-dimensional micro-fabrication," J. Photochem. Photobiol. Chem. **181**, 1–11 (2006).

103. D. Dendukuri, P. Panda, R. Haghgooie, J. M. Kim, T. A. Hatton, and P. S. Doyle, "Modeling of Oxygen-Inhibited Free Radical Photopolymerization in a PDMS Microfluidic Device," Macromolecules **41**, 8547–8556 (2008).

104. S. Moylan, J. Slotwinski, A. Cooke, K. Jurrens, and M. A. Donmez, "An Additive Manufacturing Test Artifact," J. Res. Natl. Inst. Stand. Technol. **119**, 429 (2014).

105. A. M. Forster, *Materials Testing Standards for Additive Manufacturing of Polymer Materials: State of the Art and Standards Applicability* (National Institute of Standards and Technology, 2015).

106. C. Sun, N. Fang, D. M. Wu, and X. Zhang, "Projection micro-stereolithography using digital micro-mirror dynamic mask," Sens. Actuators Phys. **121**, 113–120 (2005).

107. G. M. Gratson, F. García-Santamaría, V. Lousse, M. Xu, S. Fan, J. A. Lewis, and P. V. Braun, "Direct-Write Assembly of Three-Dimensional Photonic Crystals: Conversion of Polymer Scaffolds to Silicon Hollow-Woodpile Structures," Adv. Mater. **18**, 461–465 (2006).

108. E. B. Duoss, M. Twardowski, and J. A. Lewis, "Sol-Gel Inks for Direct-Write Assembly of Functional Oxides," Adv. Mater. **19**, 3485–3489 (2007).

109. E. B. Duoss, T. H. Weisgraber, K. Hearon, C. Zhu, W. Small, T. R. Metz, J. J. Vericella, H. D. Barth, J. D. Kuntz, R. S. Maxwell, C. M. Spadaccini, and T. S. Wilson, "Three-Dimensional Printing of Elastomeric, Cellular Architectures with Negative Stiffness," Adv. Funct. Mater. **24**, 4905–4913 (2014).